Warning and Mitigation Technologies for Travelling Ionospheric Disturbances Effects

TechTIDE

D2.2

Report on TID algorithms

Version 1.1

Grant agreement no: 776011

The TechTIDE has received funding from the European Commission Horizon 2020 research and innovation programme (2017 – 2020)

DOI: 10.5281/zenodo.2510350

INDEX

Index of Tables

Index of Figures

generated by multiple waves. As the waves propagate southward, all detectors in the Southern Europe observe them unambiguously.

Figure 5. Multi-window analysis of signal properties for accurate evaluation of TID wave period. The computed TID amplitude reaches maximum when DFT frequency is in agreement with the underlying wave. (a) Single-wave case with 62% amplitude and 110 min period. (b) Multi-wave case with two solutions (60 and 140 min periods).

Figure 6. DPS4D instruments in Europe and South Africa. Configuration of the contributing Digisonde DPS4D instruments in Europe and South Africa. (green) existing locations and links tested in 2014-2017; (red) upcoming new locations and links; (orange) potential future partners that would significantly increase TechTIDE coverage area; (gray) other instruments of the same Digisonde model, compatible with the nominal bistatic configuration.

Figure 7. HF Interferometry Method. (a) Geographical distribution of the HF sensors in Europe. (b) Coherent disturbance of a given ionospheric characteristic in the European region. (c) Estimation of dominant period of oscillation and amplitude by spectral analysis. (d) Detection of coherent oscillation activity at different measuring sites.

Figure 8. Ionosonde sensors used for HF interferometry. (a) Position of the European ionosonde sensors used for HF interferometry method; red labels indicate the current stations, and blue labels indicates future stations adopted for the method. (b) Position of the South African Digisonde DPS4D instruments to be used for HF interferometry method.

Figure 9. HF Interferometry Background model and residuals. (a) Fourier model of an ionospheric characteristic for a given 24-h. (b) Background specification of the daily variation considering the main diurnal harmonics (periods larger than 3 hour). (c) De-trended ionospheric characteristic after removing the background specification.

Figure 10. Example of TID detection for 2017-04-21 at EB040 station. From the bottom to the top: a) Velocity (red) and azimuth (blue). b) Dominant period (black) and espectral contribution (green). c) “Traffic lights” on the basis of correlations and coherency of periods between stations. Green means correlations lower than 0.6 or incoherent periods. Yellow means 3 or more stations have coherent periods, correlation larger than 0.6, and the espectral contribution is less than 50%. Red means 3 or more stations have coherent periods, correlation larger than 0.6, and the espectral contribution is more than 50%.

Figure 11. Scheme of HF interferometry methodology.

Document Information

Deliverable number:	D2.2
Deliverable title:	Report on TID algorithms
Date of Delivery:	31st August 2018
Author(s):	OE, BGD, NOA, DLR, FU, UPC, IAP
Work Package no.:	2
Work Package title:	TID identification methodologies
Work Package leader:	OE
Dissemination level:	Public
Nature:	Report

Abstract

This deliverable presents the TID detection algorithms as improved in response to design principles stated in T2.1 and their testing in the lab environment, verification against measurements taken during quiet and disturbed periods of time, benchmarking for their transition to operations, and final validation to the user requirements of accuracy, timeliness, and coverage.

Document history

Version	Date	Edited by	Reason for modification / Remarks
0.0	30 August 2018	Ivan Galkin	Original version in Google drive with inputs from all T2.2 participants
1.1	31 August 2018	Anna Belehaki	Final check

Disclaimer

This document contains description of the TechTIDE project findings, work and products. Certain parts of it might be under partner Intellectual Property Right (IPR) rules so, prior to using its content please contact the Project Coordinator (Dr Anna Belehaki, belehaki@noa.gr) for approval.

In case you believe that this document harms in any way IPR held by you as a person or as a representative of an entity, please do notify us immediately.

The authors of this document have taken all reasonable measures in order for its content to be accurate, consistent and lawful. However, neither the project consortium as a whole nor the individual partners that implicitly or explicitly participated in the creation and publication of this document hold any sort of responsibility that might occur as a result of using its content.

This publication has been produced with the assistance of the European Union. The content of this publication is the sole responsibility of the TechTIDE consortium and can in no way be taken to reflect the views of the European Union.

Executive Summary

TechTIDE project, funded by the European Commission Horizon 2020 research and innovation program [AD-1], will establish a pre-operational system to demonstrate reliability of a set of TID (Travelling Ionospheric Disturbances) detection methodologies to issue warnings of the occurrence of TIDs over the region extending from Europe to South Africa. TechTIDE warning system will estimate the parameters that specify the TID characteristics and the inferred perturbation, with all additional geophysical information to the users to help them assess the risks and to develop mitigation techniques, tailored to their application. This document is TechTIDE D2.2 "*Report on the TID algorithms*" and it is an output of TechTIDE Task 2.2 (Development of the TID identification algorithms and products) of the WP2 (TID identification methodologies) which has the final goal to release the basic algorithms for the TID identification and to test a first version of the value-added products for implementation in the TechTIDE warning system. The document highlights four aspects of the TID algorithm release process, (1) *Development* based on the concept, techniques, and algorithms as stated in TechTIDE D2.1, (2) *Verification*, an internal testing process that ensures algorithm correctness, (3) *Benchmarking* needed to prepare algorithms to transition to operations, and (4) *Validation*, an external process of ensuring that developed algorithms are compliant with the stated end user expectations.

1. Introduction

1.1 Purpose and Scope of the Document

This document presents the TIDs detection algorithms. The document is divided into four sections:

Section 1 (the current section) includes the purpose of this document and its organization.

Section 2 lists the applicable and reference documents and also contains the list of acronyms used in this document.

Section 3 describes each of the TID detection methodologies as developed.

Section 4 present the results of internal testing of individual algorithms against synthetic and reference datasets.

Section 5 reports results of benchmarking the implemented algorithms and identifies requirements to the data and processing infrastructure for implementation as a real-time TID warning system.

Section 6 discusses results of validation of the algorithms against their expected performance metrics.

Section 7 is the conclusion section providing the time plan of the WP2 activities also in relation with the WP3 work plan where the results of all TID detection methodologies will be further cross-validated and evaluated based on the assessment of current geospatial and lower atmosphere conditions.

2 Associated documents

2.1 Applicable Documents

The following table contains the list of applicable documents.

Table 11. List of applicable documents

AD	Document title
[AD-1]	Grant Agreement number: 776011 — TechTIDE — H2020-COMPET-2017

2.2 Reference Documents

The following table contains the list of references used in this document.

Table 12. List of reference documents

RD	Document title
[RD-1]	TechTIDE D2.1 Report on the design and specifications of the TID algorithms and products. May 2018
[RD-2]	TechTIDE D1.1 Initial Users´ Requirements report. February 2018
[RD-3]	ESA SSA Team, "Space Situational Awareness – Space Weather Customer Requirements Document", Rev.5a, SSA-SWE-RS-CRD-1001, 2011-07-28
[RD-4]	Reinisch, B., Galkin, I., Belehaki, A., et al. (2018). Pilot ionosonde network for identification of traveling ionospheric disturbances. Radio Science, 53; doi; 10.1002/2017RS006263
[RD-5]	Huang, X., Reinisch, B. W., Sales, G. S., Paznukhov, V. V., & Galkin, I. A. (2016). Comparing TID simulations using 3-D ray tracing and mirror reflection. Radio Science, 51, 337–343; doi 10.1002/2015RS005872
[RD-6]	Paznukhov, V. V., Galushko, V. G., & Reinisch, B. W. (2012). Digisonde observations of AGWs/TIDs with Frequency and Angular Sounding Technique. Advances in Space Research, 49(4), 700–710; doi 10.1016/j.asr.2011.11.012

[RD-7]	Altadill, D., E. Blanch, V. Paznukhov, et al, Identification of travelling ionospheric disturbances applying interferometry analysis to classical ionogram data from an ionosonde network, IEEE-TGARS, 2017 (submitted)
[RD-8]	Hernandez-Pajares, M., Juan, J. M., & Sanz, J. (2006). Medium-scale traveling ionospheric disturbances affecting GPS measurements: Spatial and temporal analysis. Journal of Geophysical Research, 111, A07S11; doi 10.1029/2005JA011474
[RD-9]	Borries C., N. Jakowski, K. Kauristie, et al. (2017), On the dynamics of Large-Scale Travelling Ionospheric Disturbances over Europe on 20th November 2003, J. Geophys. Res., 122, doi:10.1002/2016JA023050.
[RD-10]	Kutiev, I., P. Marinov, and A. Belehaki (2016), Real time 3-D electron density reconstruction over Europe by using TaD profiler, Radio Sci., 51, doi:10.1002/2015RS005932.
[RD-11]	Belehaki, A., I. Kutiev, P. Marinov, et al. (2016) Ionospheric electron density perturbations during the 7–10 March 2012 geomagnetic storm period, Advances in Space Research, ISSN 0273-1177, doi 10.1016/j.asr.2016.11.031
[RD-12]	Haldoupis, C., Meek, C., Christakis, N., Pancheva, D., Bourdillon, A. (2006). Ionogram height–time–intensity observations of descending sporadic E layers at mid- latitude. Journal of Atmospheric and Solar Terrestrial Physics 68, 539–557.
[RD-13]	Lastovicka, J., Chum, J., 2017, A review of results of the international ionospheric Doppler sounder network, Adv. Space Res. (in press).
[RD-14]	Sanz, J., J.M. Juan and G. González-Casado, et al. (2014) Novel Ionospheric Activity Indicator Specifically Tailored for GNSS Users. Proc. 27th International Technical Meeting of The ION GNSS+ 2014, Florida, September 8-12, 2014.
[RD-15]	Farmer J. D., Sidorowich J.J., Predicting chaotic time series, Physics Review Letters 59, 845-848, 1987.
[RD-16]	Farmer J. D., Sidorowich J.J, Exploiting chaos to predict the future and reduce noise, Evolution, Learning and Cognition, ed Y.C. Lee, World Scientific Press, New York, 1988.
[RD-17]	Juan J.M., Sanz J., Rovira-Garcia A., González-Casado G., D. Ibáñez-Segura, Orus R. (2018) “AATR an Ionospheric Activity Indicator Specifically based on

	GNSS Measurements", Journal of Space Weather Space Climate 8:A14, pp 1-11, DOI 10.1051/swsc/2017044
[RD-18]	Mayer, C.; Jakowski, N.; Borries, C.; Pannowitsch, T. & Belabbas, B. (2008), Extreme ionospheric conditions over Europe observed during the last solar cycle, *Proceedings of the 4th ESA Workshop on Satellite Navigation User Equipment Technologies*
[RD-19]	Belehaki A., Lj. Cander, B. Zolesi, J. Bremer, C. Juren, I. Stanislawska, D. Dialetis and M. Hatzopoulos (2006), Monitoring and forecasting the ionosphere over Europe: The DIAS project, *Space Weather*, 4, S12002, doi:10.1029/2006SW000270.
[RD-20]	Belehaki, A., I. Tsagouri, I. Kutiev, P. Marinov and S. Fidanova (2012), Upgrades to the topside sounders model assisted by Digisonde (TaD) and its validation at the topside ionosphere J. Space Weather Space Clim. 2 A20.
[RD-21]	Bergeot, N., J.-M. Chevalier, C. Bruyninx, E. Pottiaux, W. Aerts, Q. Baire, J. Legrand and P. Defraigne (2014) Near real-time ionospheric monitoring over Europe at ROB using GNSS data, J. Space Weather Space Clim. **4** A31, DOI: http://dx.doi.org/10.1051/swsc/2014028
[RD-22]	Davis, John C. (1986), Statistics and Data Analysis in Geology, John Wiley and Sons, New York.
[RD-23]	Chum, J., F.A.M. Bonomi, F.A.M., Fišer, J., Cabrera, M.A., Ezquer, R.G., Burešová, D., Laštovička, J., Baše, J., Hruška, F., Molina, M.G., Ise, J.E., Cangemi, J.I., Šindelářová, T., 2014. Propagation of gravity waves and spread F in the low-latitude ionosphere over Tucumán, Argentina, by continuous Doppler sounding: First results. J. Geophys. Res. Space Physics, 119, 6954–6965, doi:10.1002/2014JA020184.
[RD-24]	Kutiev, I., and P. Marinov (2007), Topside sounder model of scale height and transition height characteristics of the ionosphere, *Adv. Space Res.*, **39**, 759–766, DOI: 10.1016/j.asr.2006.06.013.
[RD-25]	Kutiev I, Marinov P, Belehaki A, Reinisch B, Jakowski N (2009b), Reconstruction of topside density profile by using the topside sounder model profiler and digisonde data, Advances in Space Research, 43 (11): 1683-1687.
[RD-26]	Kutiev I, Marinov P, Fidanova S, Belehaki A & Tsagouri I (2012), Adjustments of the TaD electron density reconstruction model with GNSS-TEC parameters for operational application purposes. *J. Space Weather Space Clim.*, **2**, A21.

[RD-27]	Kutiev I., P. Marinov, A. Belehaki, N. Jakowski, B. Reinisch, C. Mayer, and I. Tsagouri (2009a), Plasmaspheric electron density reconstruction based on the Topside Sounder Model Profiler. *Acta Geophysica*, **58**, 3, 420-431.
[RD-28]	Tsurutani, B.T., E. Echer, K. Shibata, O. P. Verkhoglyadova, A. J. Mannucci, W. D. Gonzalez, J. U. Kozyra, and M. Pätzold (2014), The interplanetary causes of geomagnetic activity during the 7-17 March 2012 interval: a CAWSES II overview, J. Space Weather Space Clim. 4 A02 (2014) DOI: 10.1051/swsc/2013056

2.3 Acronyms

The following table contains the list of all acronyms used in this document.

Table 13. List of acronyms

Acronym	Definition
2D	2-Dimension
3D	3-Dimension
AATR	Along-arc TEC rate
BGD	Borealis Global Designs Ltd.
CDSS	Continuous Doppler Sounding System
DLR	German Aerospace Center
DPS4D	Digisonde-Portable-Sounder-4D
EDD	electron density distribution
EGNOS	European Geostationary Navigation Overlay Service
FU	Frederick University
GBAS	Ground Based Augmentation System
GNSS	Global Navigation Satellite System
HF	High Frequency
HTI	Height-time-reflection intensity
IAP	Institute of Atmospheric Physics (Academy of Sciences of Czech Republic)

IdN	Identification Number
LSTID	Large Scale TID
MSTID	Medium Scale TID
MUF	Maximum Usable Frequency
NOA	National Observatory of Athens
OE	Fundació Observatori de l'Ebre
OI	Oblique Incidence
OTHR	Over The Horizon Radar
PFA	Probability of false alarm
POD	Probability of detection
ROT	Rate of TEC
Rx	Receiver
SNR	Signal-to-Noise Ratio
SSA SWE	Space Situational Awareness Space Weather
SSN	Sunspot Number
TEC	Total Electron Content
TID	Travelling Ionospheric Disturbance
Tx	Transmitter
UPC	Universitat Politècnica de Catalunya
VI	Vertical Incidence
WP	Work-package

3. The TID algorithms in TechTIDE

This section presents description of the TIDs algorithms in TechTIDE as updated by the design and development team. Eight methodologies for TID identification were selected for TechTIDE implementation, as summarized in Table 4. Detailed description of the original concept, design, and update plan for each of the methodologies is provided in TechTIDE Deliverable D2.1 [RD-1]. Resulting TID algorithms are discussed below in sections 3.1-3.8.

Table 4. ***Summary of TechTIDE TID identification methodologies.*** *Green background: real-time capability, gray: offline analysis only, yellow: transition to real-time in progress.*

IdN. Method	Main Characteristics	Intermediate Product	Final Product	Value added Product
1. HF-TID Detects perturbations in space from all possible sources (solar and lower atmosphere origin) and it is suitable for the identification of both MS and LS TIDs	Input: signal properties from Digisonde synchronized operation. Output: TID velocity, amplitude, propagation direction at the signal reflection point between the stations	Doppler frequency, angle of arrival, and time-of-flight from Tx to Rx, both OI and VI sounding	Separately for MS and LS TID: 1+ detections of {TID Period, Phase Velocity, Direction of propagation, Wavelength, and Amplitude}	Maps of the current TID activity Maps of TID occurrence probability
2. HF Interferometry Finds oscillation activity in ionospheric characteristics and it can detect LSTIDs only.	Input: ionospheric characteristics from VI and OI soundings. Output: 2D TID vector velocity, amplitude and period.	De-trended ionospheric characteristics and contribution of LSTID to the data variability.	Dominant period, Amplitude and 2D Vector velocity of detected LSTID.	Estimation of LSTID propagation
3. Spatial & Temporal GNSS Analysis Can detect perturbations in space from all possible sources (solar and lower atmosphere origin) and it is suitable for the identification of both MS and LS TIDs	Input: GNSS TEC from single receivers over a region. Output: Fluctuations associated to the TIDs and estimation of the propagation parameters (direction, velocity and amplitude).	De-trended GNSS data measurements.	TID Velocity, Direction of propagation and Amplitude	Climatology and physical origin of MSTID

4. GNSS TEC Gradient Analyze TEC maps and it is mostly sensitive to perturbations from LSTIDs.	Input: Grids of TEC maps over a region. Output: Latitude-time maps of TEC gradients and indication of significant gradients.	Maps of TEC and TEC rate	TEC Gradients	Graphical presentation in an image
5. 3D EDD Maps Analyze maps of TEC and ionospheric characteristics and it is sensitive to perturbation from LSTIDs only.	Input: ionospheric characteristics at the hmF2 altitude and TEC maps. Output: Analytical function of the electron density distribution with altitude from 90 km to 22000 km	1D electron density distribution (EDD) over the Digisonde locations	3D EDD results over a user-specified area. Maps of ED for vertical, horizontal and slant surfaces, specified by the user.	Maps of gradients of the integrated electron density for altitudinal ranges defined by the user.
6. HTI Reconstructs daily plot of the vertical movement of the ionospheric layers and it can capture oscillations detected in space from all possible sources.	Input: raw vertical ionogram binary data from single station Output: Reconstructed daily variability of F region virtual height.	F region virtual height variation above a given Digisonde station	Period of dominant wave activity.	Relative contribution of detected LSTID to the total variance
7. CDSS-MSTID Analyze Doppler shift of radio signals to detect quasi-periodic perturbations and associate them with overpassing MSTIDs.	Input: CDSS reflected signals, ionospheric characteristics and irregularities. Output: Doppler shift, SNR and confidence level.	Continuous Doppler shifts of fixed sounding radio frequency.	Period, Amplitude and Phase of Doppler measurements.	MSTIDs Characteristics Seismic response
8. AATR Indicator Analyze TEC data oven specific region and it is mostly sensitive to perturbations from LSTIDs	Input: slant TEC parameters. Output: the Along Arc STEC Rate, metric to characterize the ionosphere operational conditions of EGNOS.	TEC rate	Warning of ionospheric activity.	Warning about the availability in SBAS systems

Developments reported here are based on [RD-2] and [RD-3].

3.1 HF-TID

HF-TID is a direct remote sensing method for TIDs identification based on detection of quasi-periodic oscillations that the high-frequency (HF) sensor signal exhibits as it propagates the trans-ionospheric channel modulated by the traveling density perturbations. [RD-4].

3.1.1 Founding Principles of HF-TID Method

The original method [RD-6] assumes a simple case of one wave-like traveling disturbance of amplitude A and wavelength Λ (Figure 1a), propagating horizontally with a phase velocity V_p and travel azimuth Θ. In this case the HF radio signal that traverses the ionospheric channel exhibits distinct oscillating patterns of the temporal variation of its properties (Figure 1b): Doppler frequency δ(*t*), angles of elevation ε(t) and azimuth β(*t*), and time-of-flight τ(*t*) (or the equivalent group path ρ(*t*) = *c* · τ(*t*), where *c* is the free-space speed of light) [RD-4].

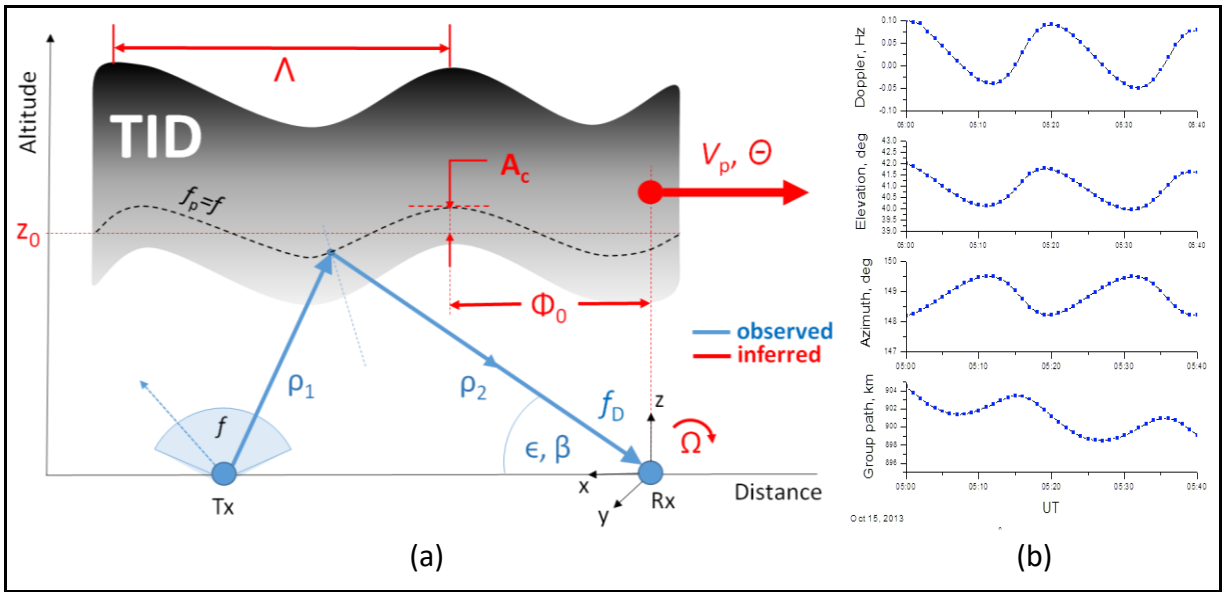

Figure 1. HF-TID method.

(a) TID model as a perfectly reflecting corrugated mirror (dashed line) moving across the area (red arrow) and causing variations of the OI signal (blue line) characteristics {δ(t), ε(t), β(t), ρ(t)}. (b) Simulation of variations of a 5 MHz signal on a 200 km radiolink from CHU transmitter to Millstone Hill observatory for a 10% 20-minute southward TID.

HF-TID associates the *observed* signal variations of ε(t), β(*t*), δ(*t*), and ρ(*t*) at the dominant TID wave angular frequency Ω with the *underlying* TID phenomenon defined by A_c, Λ, V_p, and Θ.

3.1.2. Description of HF-TID Algorithm as Implemented

Work to improve HF-TID algorithm resulted in several enhancement to the original concept as described below.

3.1.2.1 New formalism of TID inverse problem

In the presence of signal measurement noise and mistakes of signal tracking in the multi-modal environment of D2D operations, the original formalism of the HF-TID inverse problem that evaluates TID parameters from the signal properties was found prone to low accuracy of the estimates. Stronger performance of the TID computation algorithm was accomplished by relaxing one of the original simplification in the derivation of Eq. (3.1.1-3.1.3) to a more general treatment based on the complex algebra. Full derivation details are out of scope of these report; new formalism of HF-TID computations is given in Eq. (3.1.4-3.1.7), where Fraktur notation is used for complex variables:

$$\mathfrak{D}(\Omega_k) = \frac{2\pi}{N}\sum_{n=0}^{N-1}\delta_n \exp(-\mathrm{i}\,\Omega_k n) \qquad \text{Signal's Doppler spectrum (3.1.1)}$$

$$\mathfrak{B}(\Omega_k) = \frac{2\pi}{N}\sum_{n=0}^{N-1}\beta_n \exp(i\Omega_k n) \qquad \text{Signal's azimuth spectrum (3.1.2)}$$

$$\mathfrak{E}(\Omega_k) = \frac{2\pi}{N}\sum_{n=0}^{N-1}\epsilon_n \exp(-i\Omega_k n) \qquad \text{Signal's elevation spectrum (3.1.3)}$$

Then TID parameters (A_N, K, Vp, and Θ) are:

$$A_N = Abs\left[\frac{i\lambda\,\mathfrak{D}(\Omega)}{2z_0\Omega sin\epsilon_0}\right] \qquad (3.1.4)$$

$$\Theta = Re[\mathfrak{H}]$$
$$\mathfrak{H} = arctan(\mathfrak{C}_1, \mathfrak{C}_2)$$
$$\mathfrak{C}_1 = \frac{-i\lambda\,\mathfrak{D}(\Omega) + 2z_0\Omega\,\mathfrak{E}(\Omega)tan\epsilon_0}{\mathfrak{S}} \qquad (3.1.5)$$
$$\mathfrak{C}_2 = \frac{-2z_0\Omega\,\mathfrak{B}(\Omega)}{\mathfrak{S}}$$

$$\mathfrak{R} = \frac{\mathfrak{S}}{\mathfrak{D}(\Omega)} \frac{cos\epsilon_0}{z_0\lambda}$$

$$\mathfrak{S} = \sqrt{\mathfrak{T}_1 + \mathfrak{T}_2 + \mathfrak{T}_3} \qquad (3.1.6)$$

$$\mathfrak{T}_1 = -\mathfrak{D}^2(\Omega)\lambda^2 sin^2\varepsilon_0$$
$$\mathfrak{T}_2 = -i4z_0\lambda\Omega sin\epsilon_0 tan\epsilon_0\, \mathfrak{D}(\Omega)\mathfrak{E}(\Omega)$$
$$\mathfrak{T}_3 = 4z_0^2\Omega^2\left[\mathfrak{E}^2(\Omega)tan^2\epsilon_0 + \mathfrak{B}^2(\Omega)\right]$$

$$V_p = Abs\left[\frac{\Omega}{\mathfrak{R}}\right] \qquad (3.1.7)$$

3.1.2.2 Improved detection of MS-TID

One of the important user requirements identified during the initial feasibility study [RD-1] is the emphasis on detection of the medium-scale TID (MS-TID) events that are most detrimental to the operational systems for precise navigation and geolocation. While, in principle, data acquisition for HF-TID can be arranged with high signal sampling rates, high enough for reliable MS-TID identification, in practice these measurements have to be incorporated in already busy schedules of the Digisonde observatories. The stock mode of HF TID as originally tested was 40 sec transmissions every 5 minutes. Raising the sampling rate to 2.5 minutes proved to be logistically impossible without significant additional effort.

3.1.2.2.1 Signal-to-noise ratio considerations

The reason for selecting 40 sec transmission duration for HF-TID operations is the technical requirement of 40 dB signal-to-noise ratio (SNR) required for reliable data analysis. The threshold SNR requirement is driven by the need to measure the angles of arrival β_k and ϵ_k with adequate precision. The original HF-TID technique was tested on a unique radar instrument with a 2 by 1 km antenna array and subsequently migrated to the stock version of Digisonde with a 4-element receiver array and transmitter antennas, optimized for vertical rather than oblique sounding. Shortening the transmitter durations to accommodate higher cadences of measurements in support of MS-TID detections was deemed impossible without additional measures to increase SNR.

3.1.2.2.2 New 64- and 128-chip coded pulses for D2D operation

In the conventional vertical-incidence sounding mode, Digisonde DPS4D uses 533 µs pulses with phase-coded modulation. For oblique-incidence D2D operations, a longer pulse can be transmitted without blanking reception of the signals of interest by the transmitted signal.

Two new coded waveforms were developed and tested for the Digisonde DPS4D instrument, 64- and 128- complementary phase-modulated sequences that are x4 and x8 longer than the original 16-chip code.

Lowell DIgisonde International (LDI) has prepared a hardware upgrade kit for the fielded DPS4D instruments in Europe in order to perform a performance study campaign using 16- versus 128-chip pulses. Figure 2 presents SNR improvement histogram for the campaign. As expected, ~12 dB improvement in SNR is accomplished using new waveform, which enables new measurement scheduling to support 2.5 minute cadences for MSTID detection.

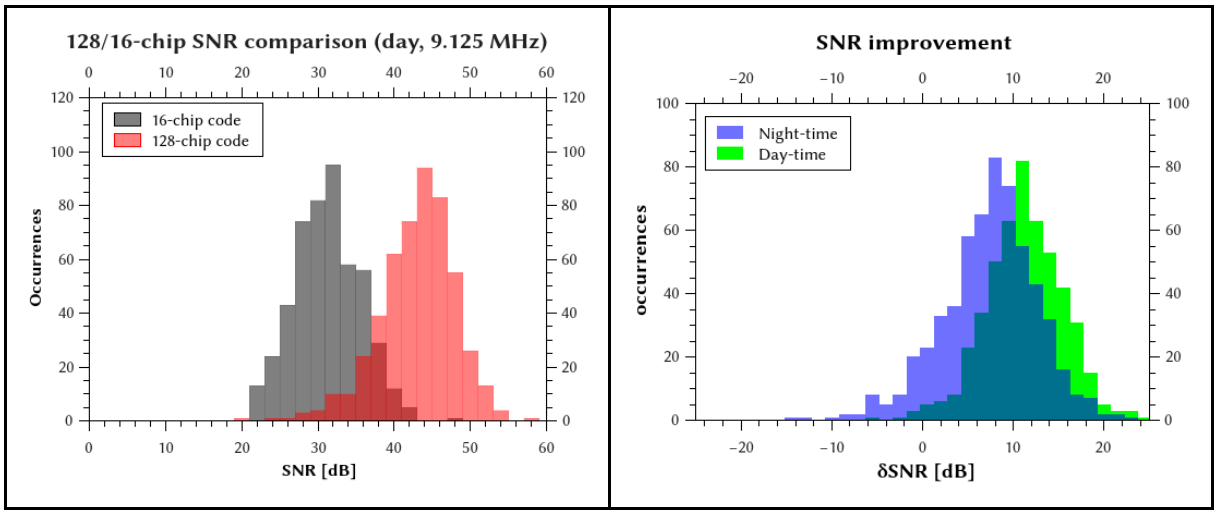

Figure 2. New 128-chip coded signal for Digisonde DPS4D model.
New waveform provides 12 dB improvement of signal-to-noise ratio during day-time, 8 dB during night-time. This allows shorter 20-sec D2D transmission programs to be scheduled at 2.5 minute cadence for efficient detection of MSTID events.

3.1.2.3 Early detection of TID events

While all TechTIDE sensors provide data in near-real-time, reliable detection of a TID event requires a good fraction of the full wave cycle to be available for analysis. For example, a TID with 30-minute wave period is reliably detected in a 30-minute window of past measurements. This latency makes an early detection of the TID (i.e., by a sensor located as close as possible to its place of origin) an important requirement. Early detection ensures timeliness of the TID warning and mitigation measures for the areas along the track of the anticipated TID travel direction.

Closer to the areas of TID generation, however, the wave may not be a well-formed sinusoidal, especially if the underlying phenomenon responsible for the TID generation is continuous (e.g., auroral oval precipitation) rather than instantaneous (e.g., explosion). The ability of HF-TID detector to efficiently operate in the mixed-wave environments is therefore beneficial to the prompt warning objective.

3.1.2.4 Event detection in mixed-TID environments

A special analysis strategy is required to detect and characterize TID events when multiple active sources generate wave mixtures. In Figure 3, an example TEC "deltagram" (timeline of TEC residuals after slow background TEC variation is removed by detrending) illustrates the existence of an active region at high latitudes between 50 and 70°N. In this region, TEC residuals do not display single TID propagating equatorward; rather, a mixture of generated waves causes a complicated interference pattern. Away from the region, only the primary LSTID wave is supported while other modes are fading out. In practice, the ability of the HF TID technique to resolve multiple TIDs was proven instrumental for detection of the weaker MSTID events in the presence of other stronger/larger waves.

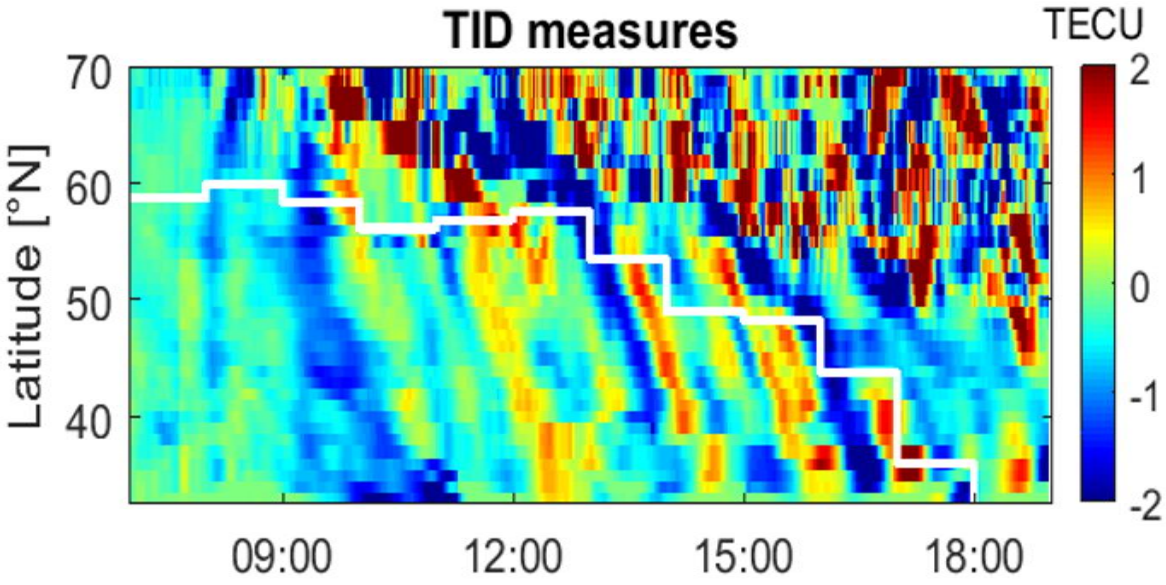

Figure 3. Timeline of ΔTEC residuals on 20 Nov 2003, obtained using a GNSS receiver chain along 15°E longitude. An active source region exists at high latitudes where a mixture of plasma density waves create a complicated interference pattern. Only the primary TID wave persists as it travels southward away from the active region, while others fade out.

The HF-TID method has an important capability to distinguish various TID waves in the multi-TID environments. In Figure 4, a minor geomagnetic storm on April 21, 2017 causes two LSTID events triggered by the brightening of auroral oval, first over the North American sector, and then over Northern European sector.

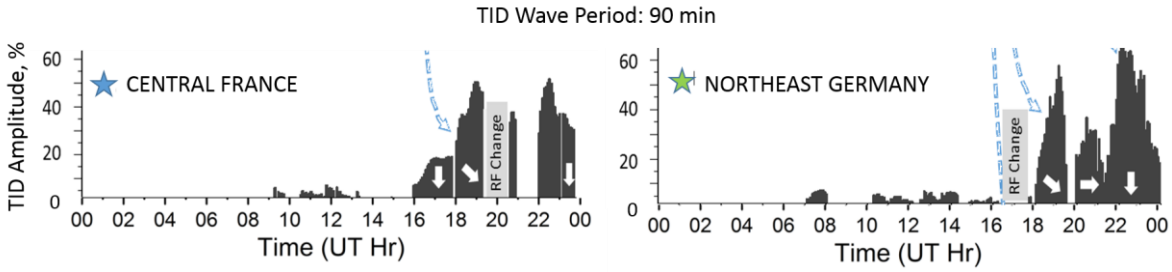

(a) TID Detection Amplitude, %

(b) Isodensity contours showing signatures of TID overpass

Figure 4. Detection of two strong 90-min LSTID events in the mixture of traveling waves during 21 April 2018 geostorm. The HF-TID site in Northeast Germany (green star) reports distinct 60% amplitude waves while the isodensity contours at Pruhonice and Dourbes sites show only ripples of the interference pattern generated by multiple waves. As the waves propagate southward, all detectors in the Southern Europe observe them unambiguously.

At the time of the events, two HF-TID Detectors were operating with coverage areas in Central France and Northern Germany, while additional five Digisonde observatories monitored TID activity located as shown in the map. Figure 4(a) demonstrates sensitivity of HF-TID method to individual components in the multi-TID mix. Both LSTID events are detected by HF-TID

sensors at 90-minute period. The right panel of Figure 4(a) shows these events as they overpass Northern Germany, detecting them at 60% amplitude. The isodensity contour plots in the same area (Pruhonice and Dourbes) do not distinguish the individual waves and do not reveal the event. Similarly to what ΔTEC residuals show at higher latitudes closer to the active region, they display only minor wave ripples.

The capability of HF-TID technique to detect and characterize individual TID events in the mixture of waves helps early detection of the TID activity onset before its reaches and affects systems operating in Central and Southern Europe.

3.1.2.5 Multi-window Wave Analysis

Additional algorithms are implemented to support reliable identification of TID waves present in the signal data. For the standard D2D measurement cadence of 5 minutes and a 32-point FFT, the analysis window is W_a = 160 min. Such low cadence of the measurements limits the selection of detectable wave periods to eight specific values ranging from 20 to 160 min (Table 5). Clearly, naturally occurring TID wave periods do not necessarily match this selection, which means that Fourier analysis of the signal variation will generate sidelobes in the spectrum. If a strong TID event is present in the signal data, the sidelobes from its spectral analysis overlap weaker waves, making their detection nearly impossible.

Table 5. **Detectable wave periods for an analysis window of 160 min (32 pt FFT at 5 min cadence)**

Detectable TID Wave Period, min	20.0	22.9	26.7	32.0	40.0	53.3	80.0	160.0

To overcome the sidelobe problem and support detection of more than one TID event in the data, multiple analysis windows are used with their lengths varying nominally from 30 to 180 minutes in 5 minute increments. Such multi-window wave analysis extends set of detectable wave periods. Figure 5 is an example of this technique applied to the measurements collected by D2D sounding between Dourbes, Belgium and Roquetes, Spain. In Figure 5(a), TID nowcast on April 21, 2017 23:28 UT suggests a single 62% LSTID with a 110-minute period. In Figure 5(b), however, there are two distinct groups that correspond to two separate TID solutions.

In order to avoid misinterpretation of DFT sidelobes for a valid TID solution, analysis of the charts is done *iteratively*; on each iteration step, the strongest wave solution is identified and then its corresponding contributions are synthesized and subtracted from time series of signal properties in the time domain. On the next iteration of the algorithm, the previously identified wave is removed and the spectra are free from its sidelobes.

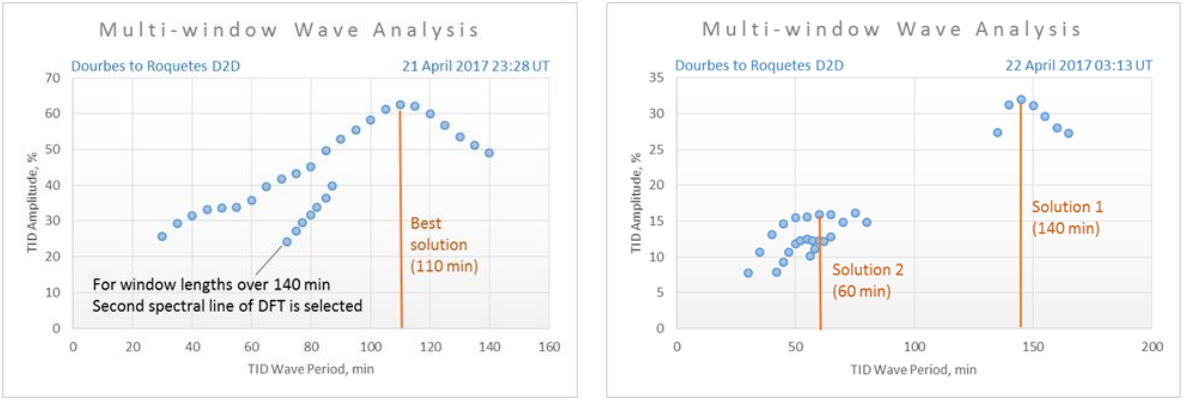

(a) (b)

Figure 5. Multi-window analysis of signal properties for accurate evaluation of TID wave period. The computed TID amplitude reaches maximum when DFT frequency is in agreement with the underlying wave. (a) Single-wave case with 62% amplitude and 110 min period. (b) Multi-wave case with two solutions (60 and 140 min periods).

3.1.2.6 Access to TID detection data

Records of all automatically detected TIDs are stored in TID database hosted by Lowell GIRO Data Center at jdbc:firebirdsql://tidbase.giro.uml.edu/tid; this is a Firebird 2.5 database with online JDBC interface via TCP port 3050. Open data access to the TID database contents is provided via servlets that support RESTful API with populated parameters of the calls:

Access to TID Detections:

https://lgdc.uml.edu/rix/tid-detector?time=yyyy.mm.ddThh:mm&window-sec=NNNN&rx=uuuuu

where

yyyy.mm.dd.Thh.mm is time of interest in ISO-standard format

NNNN is search window around the time of interest in secords

uuuuu is [optional] 5-symbol URSI code of the receiver observatory

3.1.2.7 Activate all links in the sensor network

Currently available configuration of DPS4D instruments in Europe is expanded by addition of new contributors and activating all existing links (Figure 6).

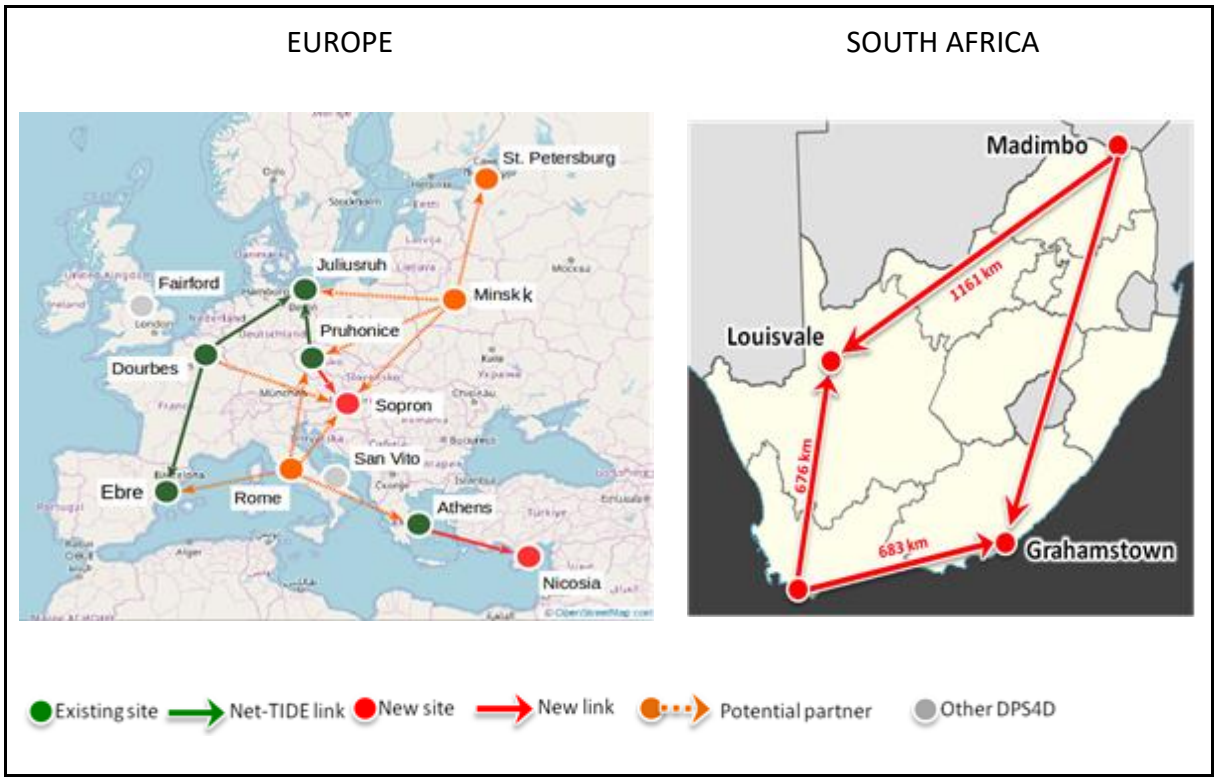

Figure 6. DPS4D instruments in Europe and South Africa.
Configuration of the contributing Digisonde DPS4D instruments in Europe and South Africa. (green) existing locations and links tested in 2014-2017; (red) upcoming new locations and links; (orange) potential future partners that would significantly increase TechTIDE coverage area; (gray) other instruments of the same Digisonde model, compatible with the nominal bistatic configuration.

3.2 HF Interferometry

HF Interferometry is a method to identify LSTIDs for the monostatic measurements of a given network of HF sensors (Ionosondes).

3.2.1 Founding Principles of HF interferometry

The method detects quasi-periodic oscillations of ionospheric characteristics, identifies coherent oscillation activity at different measuring sites of the network and sets bounds to time intervals for which such activity occurs into a given region. The TID candidate effects on ionospheric variations are isolated by applying a disturbance model. The dominant period of oscillation and amplitude of the LSTID are obtained by spectral analysis. This allows for identification of TID activity from Digisonde Networks (Figure 7) [RD-7]. Note that shaded areas in figures 7(b) and 7(d) show incoherent disturbances and oscillation activity respectively.

The propagation parameters are reconstructed from the measured time delays of the disturbance of a given ionospheric characteristic at different sensor sites. The time delay Δt_i of the disturbance with respect to a reference sensor is expressed as $\Delta t_i - \underline{s} \cdot \Delta \underline{r_i}$, where $\underline{\boldsymbol{s}} = \frac{\underline{v}}{v^2}$ is the slowness vector of the disturbance propagating with the velocity $\underline{v}$, and $\Delta \underline{r_i}$ is the relative position vector of the i[th] sensor with respect to the reference. Δt_i are obtained by correlation analysis to multi-site measurements and $\underline{s}$ is estimated solving Equation (3.2.1). Finally, the 2D vector velocity of the LSTID is obtained according to Equation (3.2.2).

$$\Delta t_i - \underline{s} \cdot \Delta \underline{r_i} = 0 \tag{3.2.1}$$

$$\underline{v} = \frac{\underline{s}}{s^2} \tag{3.2.2}$$

Due to the geographical distribution of Digisonde sites within Europe network (distant by about 1000 km from to each other), only identification of LSTID is feasible in principle, which are associated with auroral and geomagnetic activity, directly related to Space Weather [RD-7].

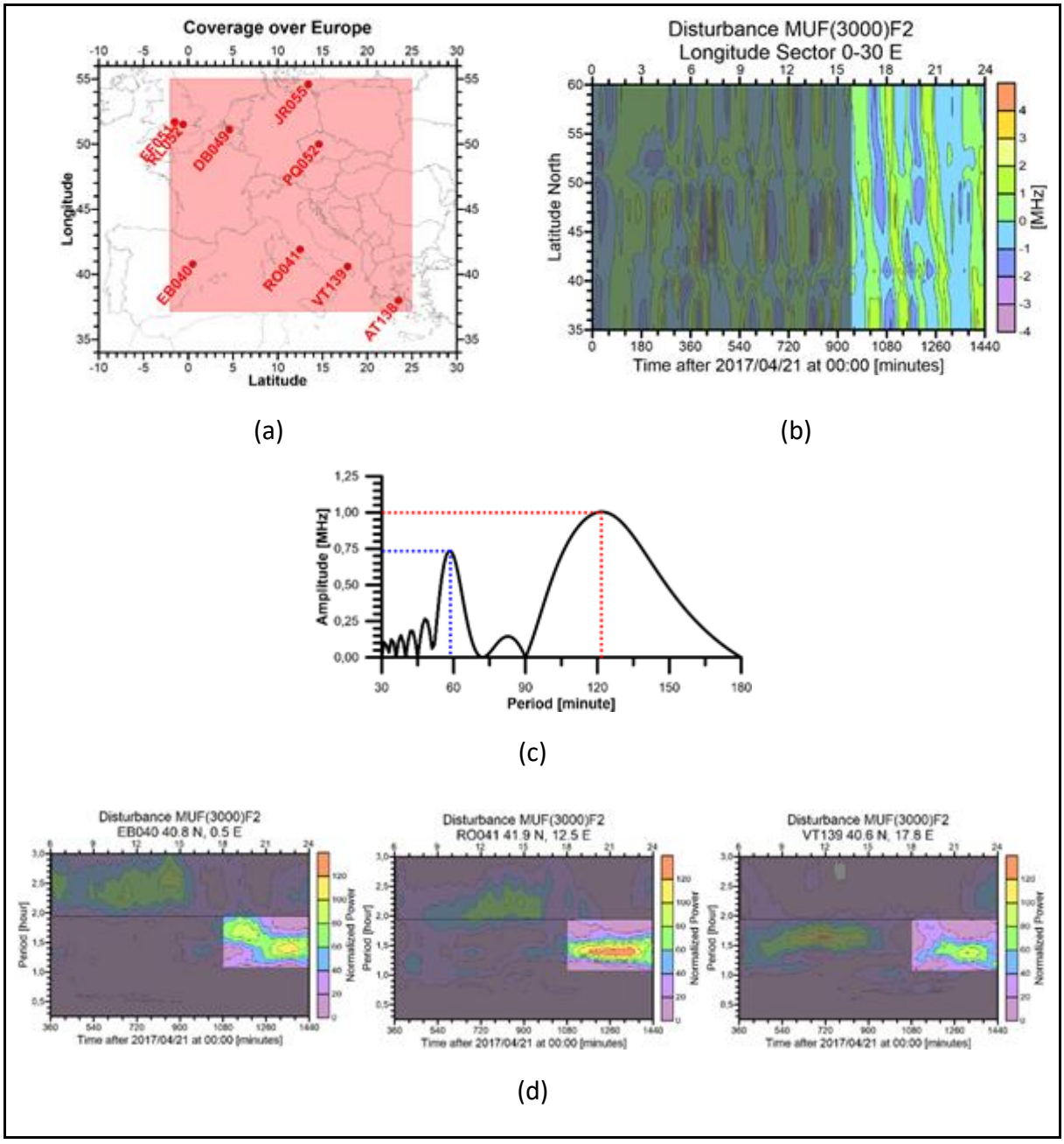

Figure 7. HF Interferometry Method.
(a) Geographical distribution of the HF sensors in Europe. (b) Coherent disturbance of a given ionospheric characteristic in the European region. (c) Estimation of dominant period of oscillation and amplitude by spectral analysis. (d) Detection of coherent oscillation activity at different measuring sites.

3.2.2 Description of HF interferometry algorithm as implemented

3.2.2.1 Extending spatial coverage

The HF interferometry method uses the Maximum Usable Frequency (MUF) obtained from 9 European Digisondes (Figure 8a) and 4 Digisondes from South Africa (Figure 8b). It uses near real time data from the GIRO DIDBase Fast Chars (http://giro.uml.edu/didbase/scaled.php).

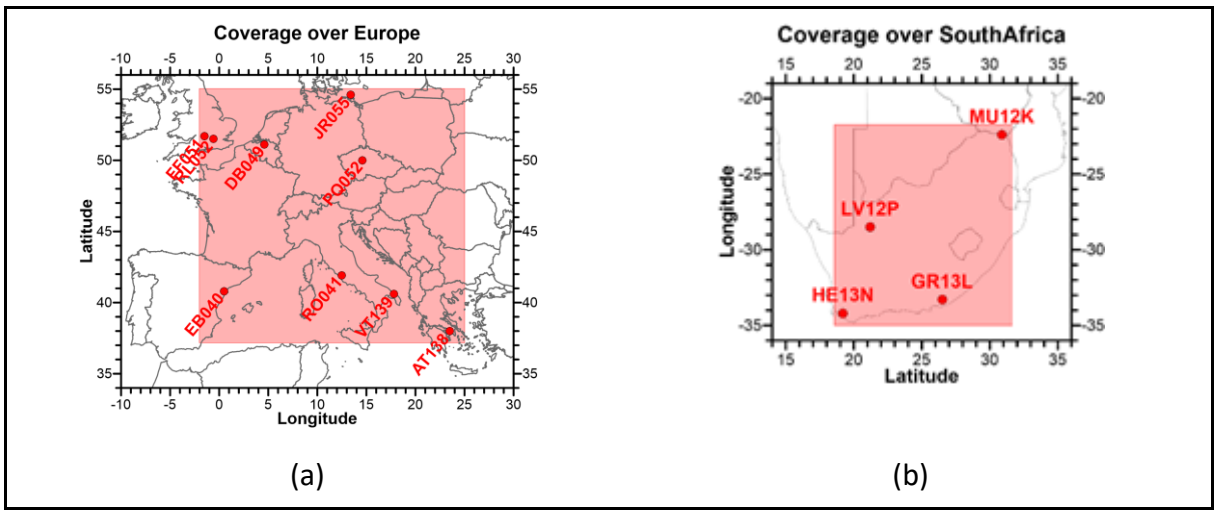

Figure 8. Ionosonde sensors used for HF interferometry.
(a) Position of the European ionosonde sensors used for HF interferometry method; red labels indicate the current stations, and blue labels indicates future stations adopted for the method. (b) Position of the South African Digisonde DPS4D instruments to be used for HF interferometry method.

3.2.2.2 Upgrading for near-real-time operation

Original HF interferometry method concept applies off-line for test cases characterized by TID activity. The test cases and the required data are obtained from the TechTIDE open access repository and on time intervals when persistent TID activity of significant amplitude is observed by the Net-TIDE experiment (http://tid.space.noa.gr). The final code provides near-real-time information of detected LSTID activity above given measuring sites within European and South African regions. The current codes for European region are running off-line in near real time at 5 min cadence which can track LSTIDs only. Current codes for South African region are running off-line at 15 min cadence which can track LSTIDs only.

3.2.2.3 Upgrading for obtaining Spectral Energy Contribution of LTIDs

Original HF interferometry lacks of information about the LSTID contribution to the variability of the ionospheric characteristics under analysis. Applying the Parseval's relation we will estimate the *Spectral Energy Contribution* (SEC) of the periodic range of the LTIDs to the total energy which is equivalent to the contribution of the LTIDs to the total variability of the given time series (Equations 3.2.3-3.2.4),

$$\sum_{n=-\infty}^{\infty} |x[n]|^2 = \frac{1}{2\pi} \int_{-\pi}^{\pi} |X(\omega)|^2 d\omega \sim \sum_{T=T_S}^{T=T_E} A(\omega)^2 \qquad (3.2.3)$$

$$SEC(\%) = \frac{\sum_{T=T_{TID_S}}^{T=T_{TID_E}} A(T)^2}{\sum_{T=T_S}^{T=T_E} A(T)^2} \qquad (3.2.4)$$

where ω is the angular frequency of the period T, T_{TIDS} and T_{TIDE} are the starting and ending periods of the periodic range of the LSTID respectively, and T_S and T_E are the starting and ending periods of the total periodic range under analysis.

3.2.2.4 Background specification

For the development of the HF interferometry method we use as background specification of the daily variation the contribution of the main diurnal harmonics based on a Fourier model for a 24-h time interval. The disturbance potentially associated to TID in the last 6-h interval will be related to the de-trended ionospheric characteristics after removing the main daily harmonics (Figure 9).

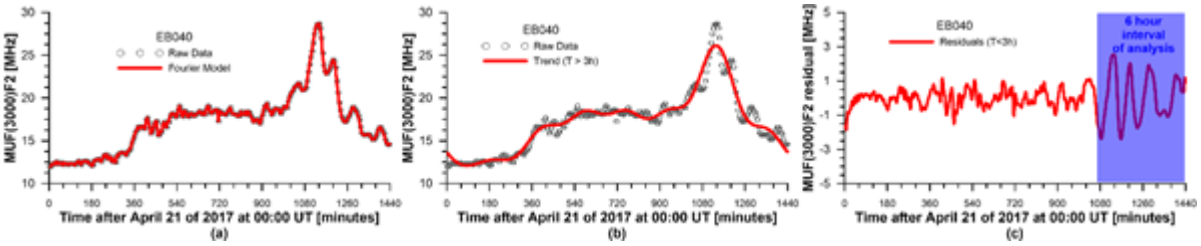

Figure 9. HF Interferometry Background model and residuals.
(a) Fourier model of an ionospheric characteristic for a given 24-h. (b) Background specification of the daily variation considering the main diurnal harmonics (periods larger than 3 hour). (c) De-trended ionospheric characteristic after removing the background specification.

3.2.2.5 Multi-step data analysis

As a first step, the method verifies that there is enough data to run. This means that a given network (Europe and South Africa) has at least 3 stations available and that individual sensors provides data for more than 80% of the time interval of interest.

Second step removes the daily trend and extract the disturbance of the time series. For that, we calculate the background specification as the contribution of the main diurnal harmonics (T > 3h) based on a Fourier model for a 24-h time interval and remove it of the time series. Finally, we work with the residual values of the data for the last six-h time window (figure 9).

Third step apply spectral analysis to detect possible TID-like variations in the time series. Amplitude spectra are calculated for individual measuring sites and find the period with largest amplitude and with a confidence level larger than 0.95. If periods with largest amplitude are coherent among different sites, we estimate the amplitude, the dominant period and the espectral energy contribution of the possible TID.

Finally, we estimate the vector velocity of the disturbance (velocity modulus and azimuth) by eqs. (3.2.1) and (3.2.2). The time delays of disturbance are obtained by calculating the time-lag for maximum cross-correlation. To estimate the propagation velocity vector of this TID-like variation requires a minimum of 3 stations and a cross-correlation larger than 0.6.

Figure 10 shows an example of TID detected by the method. From top to bottom: (c) “traffic lights” as a system of alert, (b) period and espectral contribution, and (a) velocity and azimuth. Figure 10 indicates that above Ebro station (EB040) there was some wave activity at around sun-rise (4-6 UT), and that at the end of the day clearly developed a TID with a velocity around 600 m/s, an azimuth of 180º and a dominant period at about 85 minutes.

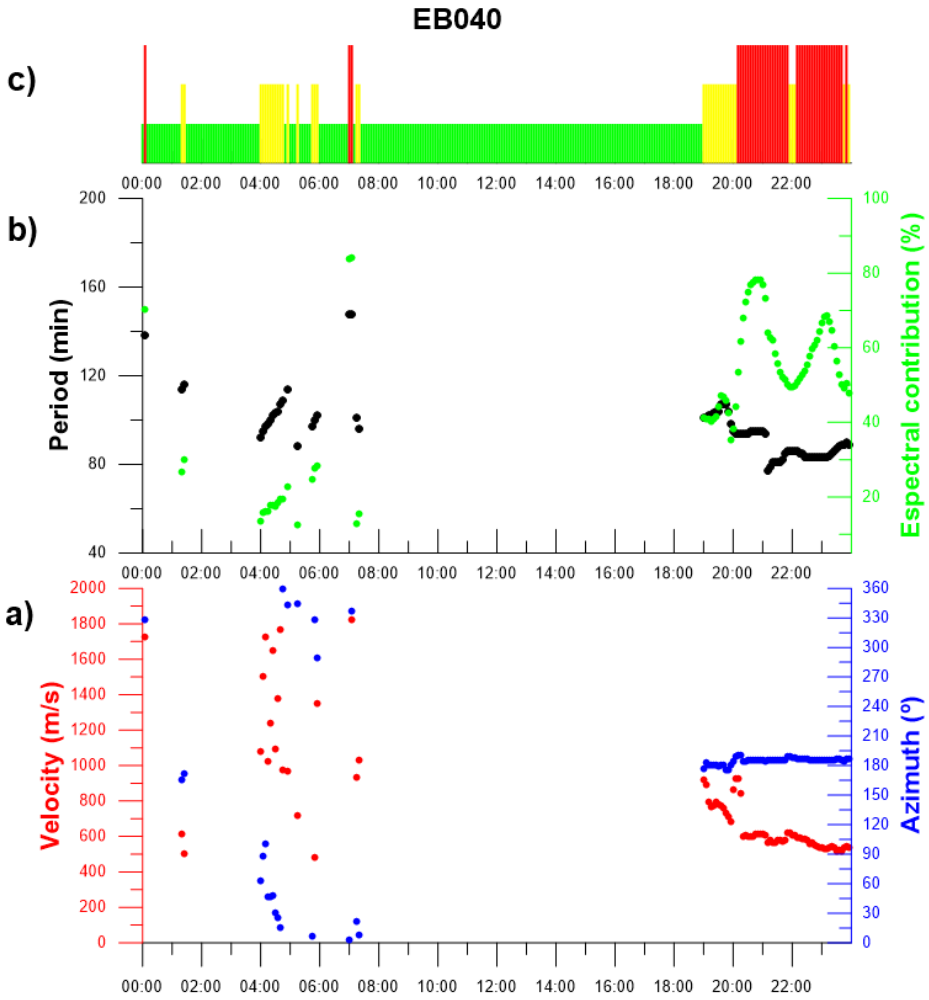

Figure 10. Example of TID detection for 2017-04-21 at EB040 station.
From the bottom to the top: a) Velocity (red) and azimuth (blue). b) Dominant period (black) and espectral contribution (green). c) "Traffic lights" on the basis of correlations and coherency of periods between stations. Green means correlations lower than 0.6 or incoherent periods. Yellow means 3 or more stations have coherent periods, correlation larger than 0.6, and the espectral contribution is less than 50%. Red means 3 or more stations have coherent periods, correlation larger than 0.6, and the espectral contribution is more than 50%.

The current flow scheme of the HF interferometry methodology is shown in figure 11, and the intermediate product (ASCII file to be sent every 5 min) in figure 12.

A bash script downloads the data from the DIDBase and calls the different programs to obtain, as a result, one file which contains the values of the period, spectral power, amplitude, % contribution, velocity, azimuth, "traffic light" and 2 index, IQ (index of data quality) and IA

(index of the range of the TID) for each station for the detected TID. IQ is the ratio of the number of stations used to observe a TID event in relation to the number of stations that are providing data. IA is the ratio of the number of stations used to observe a TID event in relation to the total number of stations of the network. The bash script is running in a dedicated machine with a crontab that executes the method every 5 minutes, then, we obtain a file with the corresponding values every 5 minutes. We are running the HF interferometry method in near real-time but off-line since 2018-04-25 for the European region. For the South African region we are running the HF interferometry method for test cases but it is ready to work in near real time.

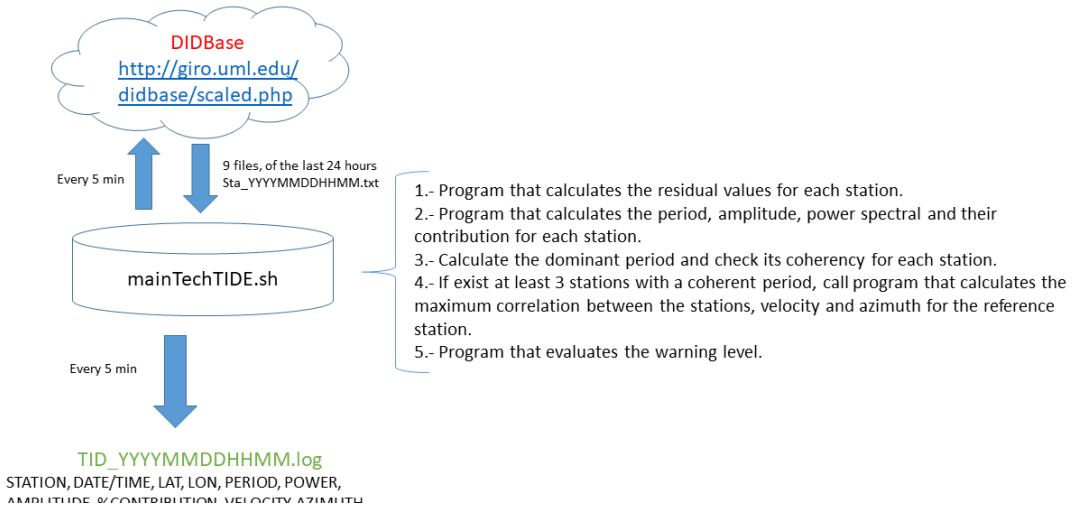

Figure 11. Scheme of HF interferometry methodology.
Every 5 minutes the bash file asks for data on the net and calls programs to calculate different variables.

HE	ST	FL	ESTA	DATE	TIME	ALATI	ALONG	NW	IW	PERIO	POTENCIA	AMPLI	CONTP	VEL	AZI	SEM	IQ	IA
1	1	1	AT138	201704212220		38.00	23.50	1	1	0	0.000	0.0000	0.0000	-999	-999	1	0	0
1	2	1	DB049	201704212220		50.10	4.60	1	1	80	59.913	0.9684	23.6257	626	186	2	87	100
1	3	1	EB040	201704212220		40.80	0.50	1	1	85	102.435	1.4543	52.7492	589	187	3	87	100
1	4	1	FF051	201704212220		51.70	-1.50	1	1	79	113.672	0.8941	41.5444	558	185	2	87	100
1	5	1	JR055	201704212220		54.60	13.40	1	1	80	64.522	1.0648	31.1211	629	181	2	75	100
1	6	1	PQ052	201704212220		50.00	14.60	1	1	79	75.669	0.9359	22.8885	555	183	2	87	100
1	7	1	RL052	201704212220		51.50	-0.60	1	1	79	92.278	0.3253	39.3728	564	177	2	87	100
1	8	1	RO041	201704212220		41.90	12.50	1	1	88	80.439	0.8961	47.1290	615	186	2	87	100
1	9	1	VT139	201704212220		40.60	17.80	1	1	82	62.049	0.3808	43.1835	636	204	2	87	100

Figure 12. Intermediate product: ASCII file that contents the HF interferometry method results. First 9 columns contain information about the station and time interval. After that, the results of the calculations are: period, spectral power, amplitude, % contribution, velocity, azimuth,"traffic light", index of quality IQ and index of range IA.

We have two versions of the bash file: one is working in near-real time, and the other works under defined time intervals. We have run the method for the whole year 2017 for the European region with the aim to check the performance of the method and test potential bugs. As a result of this process we have detected many TIDs events of auroral origin and due to sunrise effect. Figure 13 shows the amplitude of the TID for those cases with high warning level. We can see lack of data during summer time, due to the presence of Es layer. We detected the sunrise effect during the whole year, and some cases of auroral origin especially during equinox seasons at night.

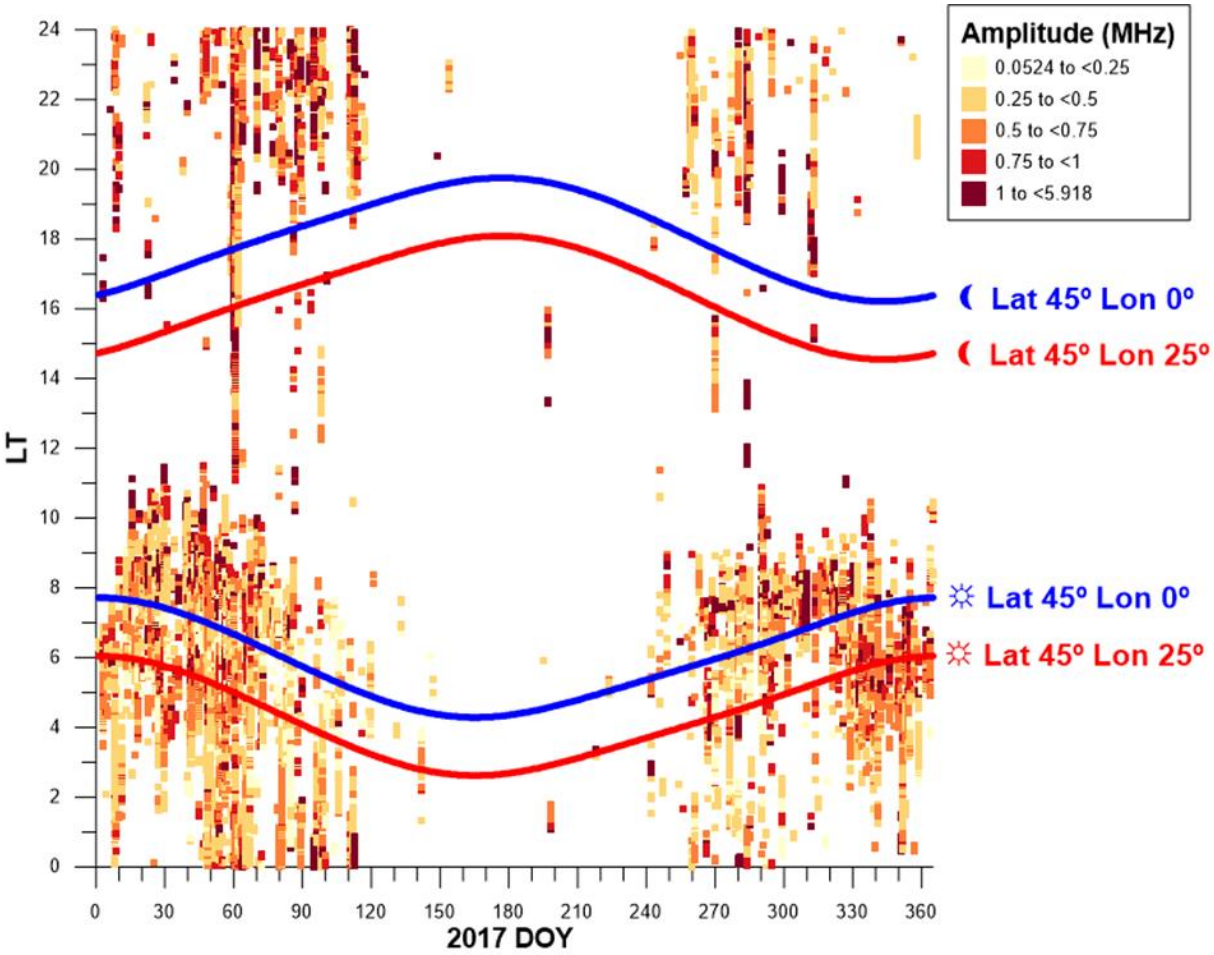

Figure 13. TID Amplitudes detected by the HF interferometry method during 2017. The climatological analysis shows dominant activity near Sun rise and at night.

3.2.2.6 Some identified problems

- Lack of data due to the presence of sporadic layer, especially during summer months (see figure 13). Figure 14 shows an example for 24 June 2017 over DB049 station. We can observe that the presence of Es layer screens the F2 layer. For this time period, the corresponding station will no contribute to the TID detection.

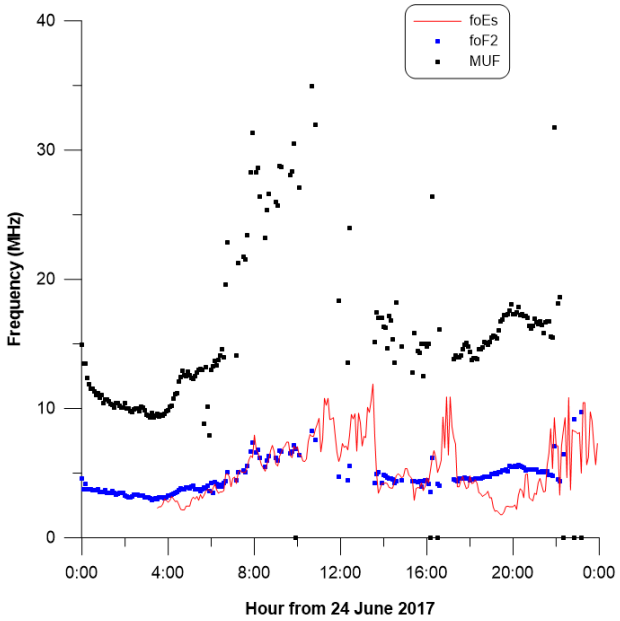

Figure 14. Red line corresponds to foEs, blue dots corresponds to foF2 and black dots correspond to MUF values for 24 June 2017 at DB049 station.

- Identification of spikes in time series. Spikes are a potential problem for HF interferometry method because introduce noise in the time series that make difficult to identify TIDs and produce artificial disturbances. These spikes are result of the auto-scaling algorithms that makes possible near-real time data. We have been working to detect and remove spikes automatically from the time series. Figure 15 shows an example of spike detection and removal: the left panel shows the raw data in red with some spikes and also some gaps, the right panel shows the same case after removing the detected spikes. Results show how artificial disturbance generated by the spikes near time 960-1080 have been removed and the residual values look smoother.

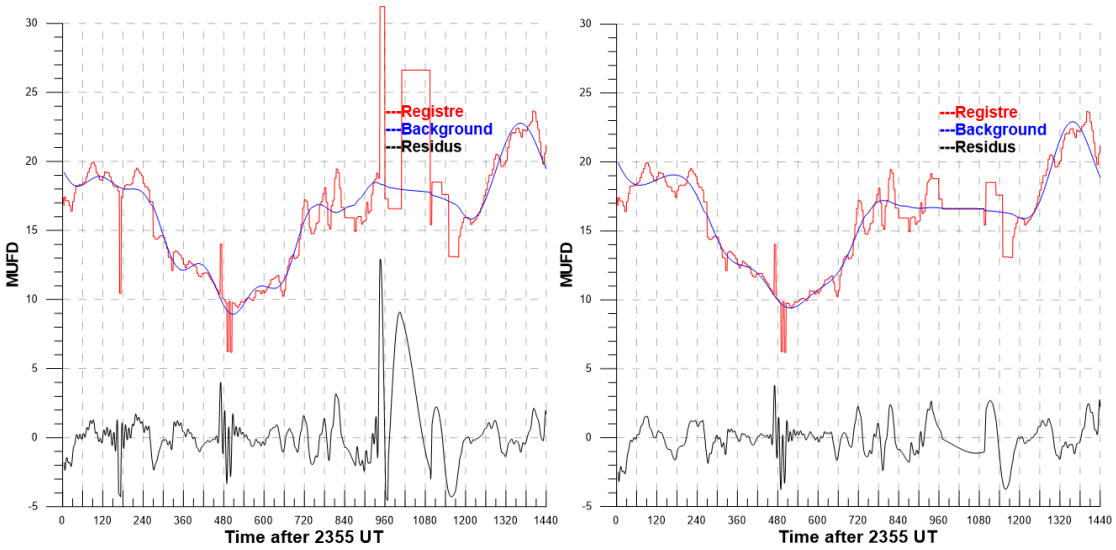

Figure 15. Example of spikes and their elimination for 2018-05-17 at EB040 station. On the left panel raw data (in red), the calculated background (in blue) and the residual values (in black). On the right the same after running the software to eliminate spikes.

- Select the appropriate thresholds (for the maximum correlation, to eliminate spikes, to search for coherent periods from different stations, etc...) to achieve a correct identification of a TID.

3.3. Spatial and Temporal GNSS Analysis

3.3.1. Founding Principles of Spatial and Temporal GNSS Analysis Technique

The procedure to detect and to characterize TIDs, including velocity and period will be based on the Spatial and Temporal analysis of GNSS measurements [RD-7]. This procedure allows the study of any ionospheric perturbation (including MSTID or LSTID) and can be used for detecting the TID (with a single receiver) or estimating the propagation parameters (from a network of receivers). The basic GNSS measurement used is the geometry-free combination of carrier phases, with measurement noise at the level of few millimetres. The first step for the TID detection is to detrend the data in order to remove the well-known dependencies, such as diurnal and elevation angle variations, having larger time scales than the TID. This detrending can be applied in real-time and for a single receiver. Therefore, information about the TID occurrence can be obtained for the monitored region (around the receiver). Figure 17 shows for three different receivers the original measurements in the left, and the de-trended data in the right. The baselines are less than 40 km, clearly under the MSTID wavelength.

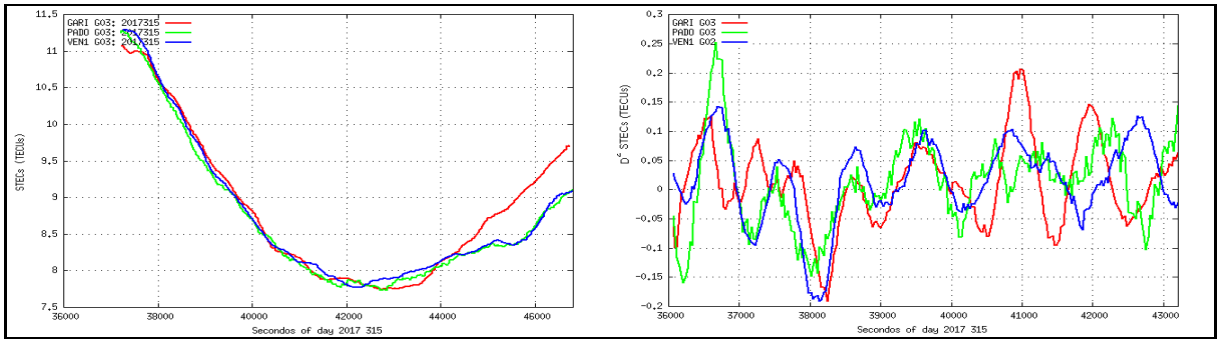

Figure 16. Spatial and Temporal GNSS Analysis
Example of de-trending and temporal variation procedure for three GNSS receivers.

After de-trending the measurements, it is possible to detect, in any of the receivers, the fluctuations associated with the TIDs. Similarly to above method, it is possible to estimate the propagation parameters (propagation direction, velocity and amplitude) by correlating these fluctuations on the different receivers in the network. Here $\Delta t_i = \vec{s} \cdot (\Delta \vec{r}_i + \mathrm{v}_{IPP} \cdot \Delta t_i)$, where $\vec{s} = \frac{v}{v^2}$ is the slowness vector of the disturbance propagating with the velocity $\vec{v}$, $\Delta \vec{r}_i$ is the relative position vector of the i[th] sensor with respect to the reference, and $\vec{v}_{IPP}$ is the velocity of the ionospheric pierce point. Δt_i are obtained by correlation analysis to multi-site measurements and $\vec{s}$ is estimated solving Equation (3.3.1). Finally, the 2D vector velocity of the LSTID is obtained according to Equation (3.2.2).

$$\Delta t_i - \vec{s} \cdot (\Delta \vec{r}_i + \vec{v}_{IPP} \cdot \Delta t_i) = 0. \qquad (3.3.1)$$

The same procedure can be applied for LSTIDs and MSTIDs, but, for the detrending, one has to take into account the characteristic periods of these two TIDs.

3.3.2. Temporal and spatial GNSS analysis as implemented

The analysis of GNSS data for detecting MSTIDs consists on two parts/tools: one for detecting the MSTIDs itself and another for estimating the propagation parameters of the MSTID (velocity, direction, amplitude and period)

3.3.2.1 MSTID detection

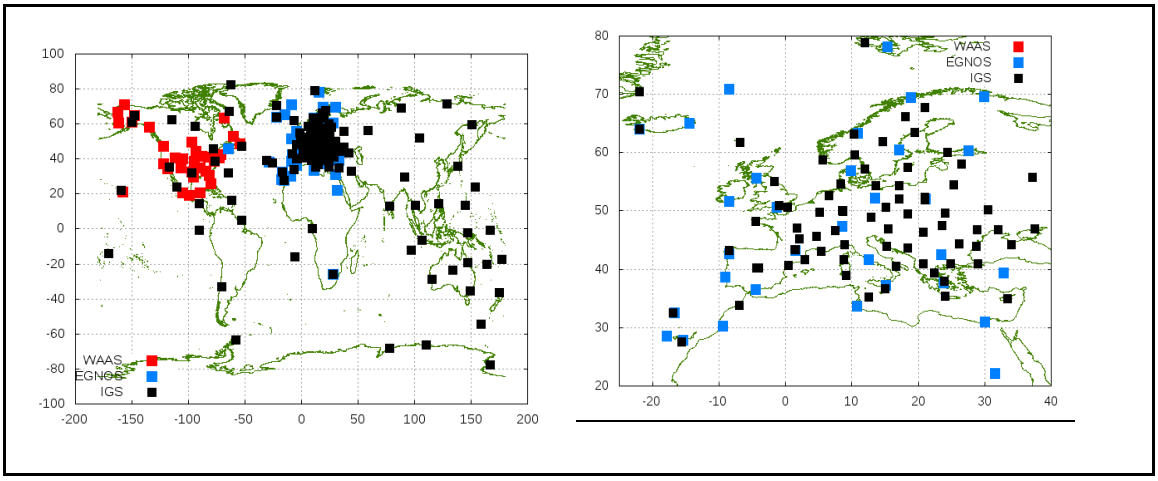

Figure 17. Receiver distribution for detecting MSTID activity
(a) World wide distribution of GNSS receivers: WAAS receivers (red), EGNOS receivers (blue) and IGS receivers (black); (b) Zoom for Europe.

For each of those receivers the tool computes the lack of linearity of the geometry-free combination of carrier phases (L_{GF}):

$$D^2 L_{GF}(t-\tau) = 0.5(L_{GF}(t-2\tau) + L_{GF}(t)) - L_{GF}(t-\tau)$$

where τ is selected as a trade off between the efficiency on detecting MSTIDs and the required latency. In the current implementation we are using a value of 300s.

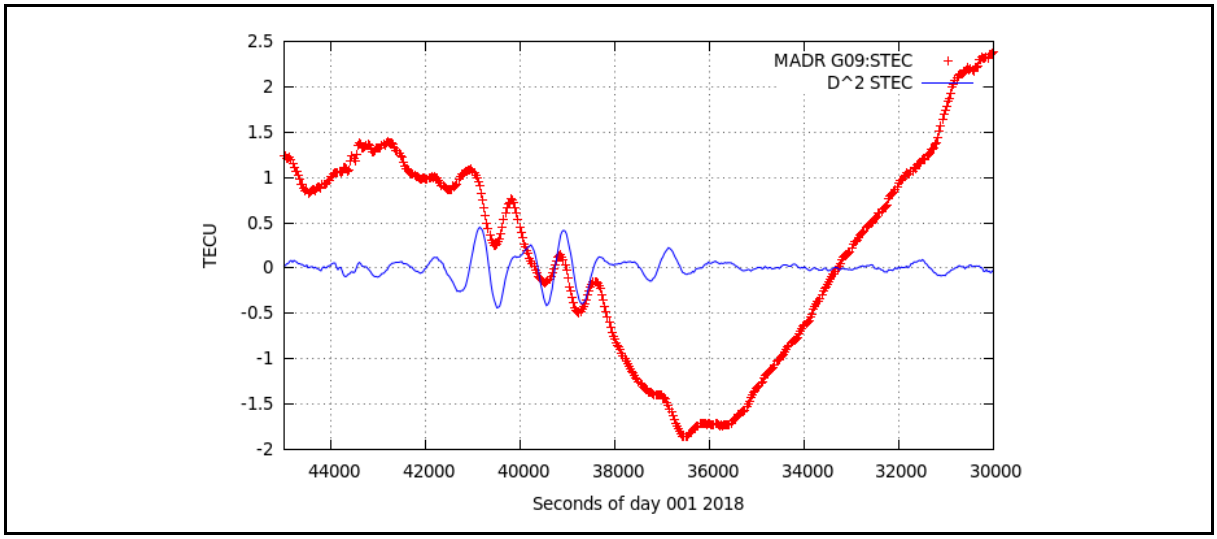

Figure 18. **Example of the detrending method for detecting MSTIDs**

The previous example shows how one can extract the effect of the TID on the geometry-free combination of carrier phases and, consequently the part of the ionospheric error that any single frequency user cannot mitigate by interpolating the perturbations in the reference receivers. But the final effect on the navigation into a NRTK network depends also on the geometry, that means that the effect do not depend only on the amplitude but on how the perturbation is translate to the position error through the navigation filter.

In this sense, the output of the tool is the TID indicator as the error in the navigation solution that can be associated to the TID. Moreover, beside this TID indicator the tool also provide the geometrical Dilution of Precision (DoP) in order to identify whether a high value of the indicator can be due to a bad geometry. Table 6 is an example of the output.

Table 6. **Example output of TID Indicator**

Time (s)	Receiver	TID (m)	DoP (m)
600	madr	0.0021	1.71e+00
900	madr	0.0033	1.86e+00
1200	madr	0.0039	1.87e+00

1500	madr	0.0021	1.87e+00
1800	madr	0.0033	1.86e+00
2100	madr	0.0068	2.15e+00
2400	madr	0.0051	2.44e+00
2700	madr	0.0034	2.24e+00
3000	madr	0.0031	2.07e+00

Figure 19 illustrates an example of the 2nd differences of STEC and the TID index

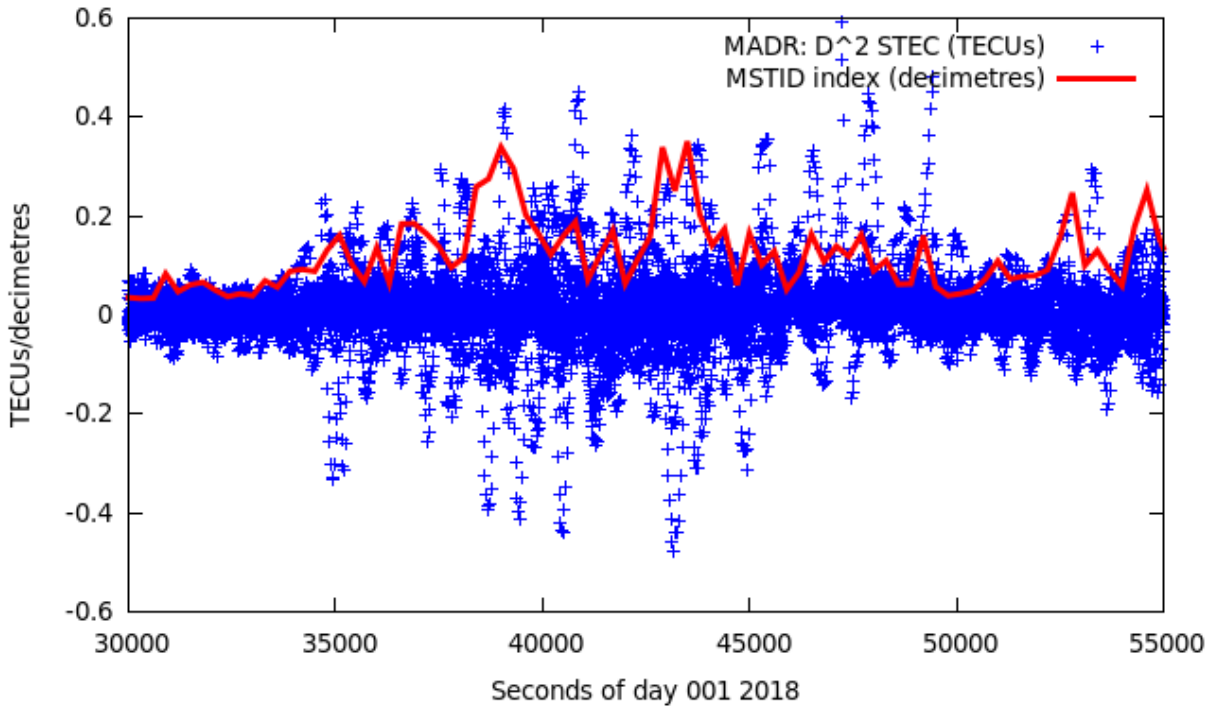

Figure 19. Example of the MSTID indicator.
Second differences of D^2L_{GF} (blue). Impact on navigation (red).

3.3.2.2 Estimation of propagation parameters

The estimation of the TID parameters are based on the coherency between TID effects on close receivers. The next plot depicts the TID effects on two nearby receivers (MADR and VILL).

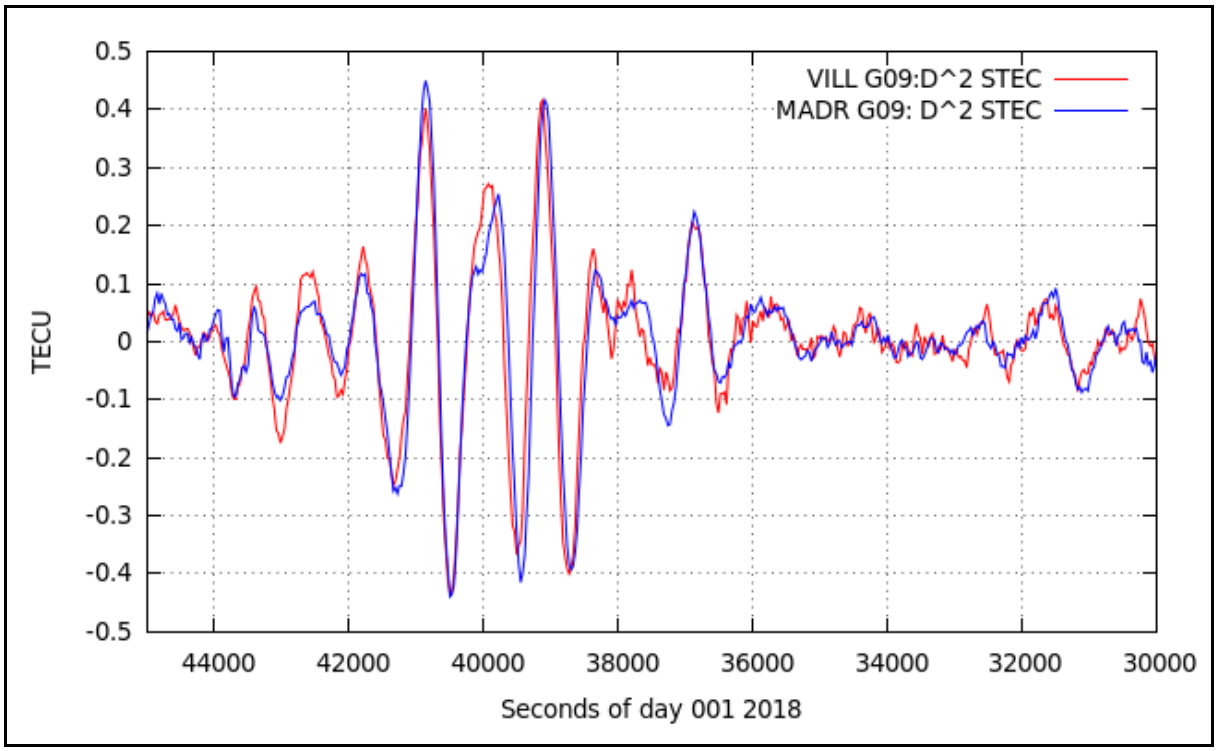

Figure 20. Example of the impact of a MSTID in the measurements gathered by 2 close receivers (MADR and VILL) from the transmitter G09

In the previous plot one can see that the TID affect in a similar way to both receivers. If this is the case, one can estimate the delay between the two detrended signals (Δt), and, from this delay, the propagation parameters assuming the following relationship:

$$\bar{s}\,(\Delta\bar{r} + \bar{v}_{ipp}\,\Delta t) = \Delta t$$

where

$$\bar{s} = \frac{\bar{v}}{v^2}$$

is the slowness vector, $\Delta\bar{r}$ is the relative vector between receivers and $\bar{v}_{ipp}$ the velocity of the ionospheric pierce point.

Obviously, for estimating the velocity parameters one needs at least 2 independent baselines, i.e. 3 receivers with distances of few tens of kilometres. This is a hard constraint and we have only identified 6 of these networks in Europe (see the map).

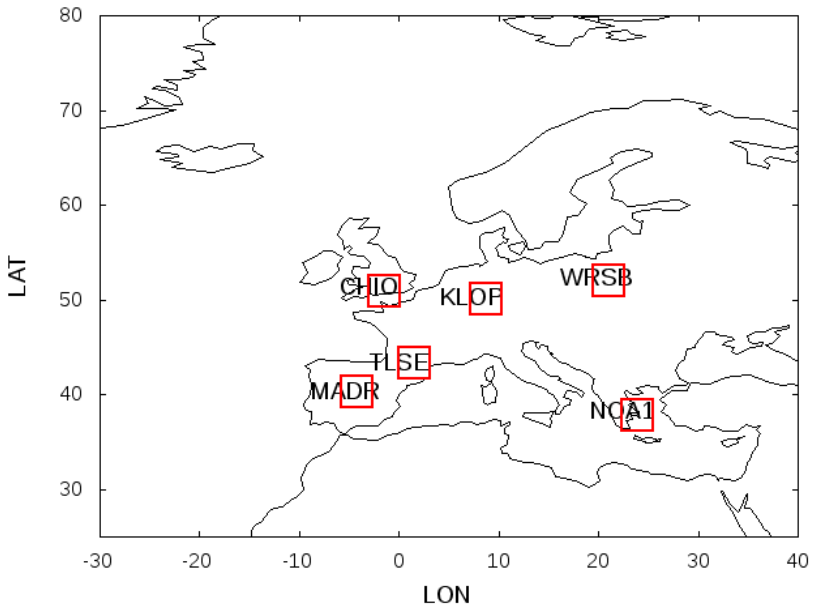

Figure 21. The six small networks used for estimating MSTID propagation parameters.

For each of these networks the tool detects the TID and write a sheet with some of his characteristics. This is an example of this sheet with a brief explanation of the parameters.

Identifier
MSTID: 21300 22 tlse
time: 21300
sat: 22

sta_ref: tlse

amplitude: 0.022 (0.21 TECUs)

elevation: 60.9

Results from the correlation

name ipp_lon ipp_lat d_x d_y corr d_t T_mx-T_mn

ADD_STA: tlmf -.29 42.30 -8.29 1.39 .98 26.00 361.00

ADD_STA: tlsb -.17 42.16 1.71 -14.17 .96 72.00 347.00

STA_REF : tlse -.194 42.285

SCAN_velocity(km/s,deg): .062 29.037

where:

- **STA_REF** refers to the reference receiver (tlse) and its ipp longitude and latitude.
- **SCAN_velocity** is the velocity of the ionospheric pierce point $\underline{v}_{ipp}$
- **ADD_STA** refers to the two basesines (tlsb and tlmf) with the ipp longitude and latitude.
- **d_x** and **d_y** are the projection of the relative vectors $\Delta\underline{r}$ into the East and North direction, in km
- **corr** refers to the correlation coefficient with respect to the perturbation in the reference receiver
- **d_t** is the delay of the signal with respect to perturbation in the reference receiver (Δt)
- **T_mx-T_mn** is the time difference for maximum and minimum correlation (semi-period)

LMS fit

SLOWNESS: -7.069561 -9.673873 .16E+01 .13E+01

RMS_residuals: .33E-15

PROP_velocity(km/s,deg): .083 -143.841

SOL: 21300 22 tlse 83. -144.

where :

- **SOL** refers to the propagation velocity in m/s and the azimuth in degrees.

3.4. GNSS TEC gradient algorithms

3.4.1 Founding Principles of GNSS TEC Gradient Method

Large scale Travelling Ionospheric Disturbances (TIDs) occurring during geomagnetic storms produce strong temporal and spatial TEC gradients which are observed closest to the source region of LSTIDs. These gradients are attributed to heating and convection processes which are related to the excitation of LSTIDs [RD-8]. Temporal and spatial gradients are calculated based on maps of TEC. Figure 22 presents the results of this method applied on the 20 November 2003 storm.

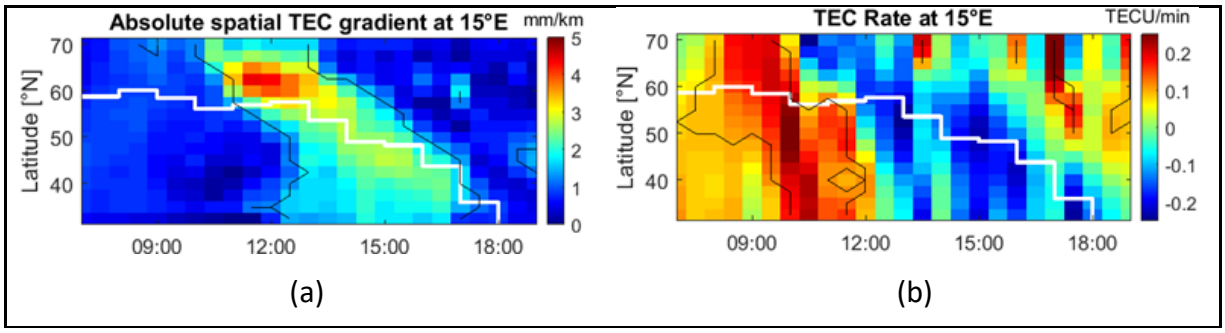

Figure 22. GNSS TEC gradient method
Results for 20 November 2003, (a) shows the spatial TEC gradients and (b) the TEC rate derived from DLR TEC maps at 15°E.

In Figure 22, both the spatial TEC gradients (a) and the TEC rate (b) are derived from DLR TEC maps at 15°E. The white line approximates the trough location. Large-scale TEC gradients are routinely produced by the DLR and the results will be used on TechTIDE for the real-time identification of LSTIDs and the identification of the source region.

3.4.2 Description of GNSS TEC gradient as implemented

Input for this algorithm are NRT TEC maps for Europe, which are generated at DLR. TEC is given in a regular grid with fixed grid size with 1°x1° grid size in latitude and longitude. The TEC gradient is computed as difference between neighbouring grid points dTEC/dd measured in TECU/°. This value is converted to L1 range error per distance measured in mm/km, using the estimation 1TECU~160mm and the distance in degree is converted to kilometers. This is the typical measure of TEC gradients used in aviation applications.

3.5. 3D-EDD Maps

3.5.1 Founding Principles of 3D-EDD Mapping Method

The 3-dimensional Electron Density Distributions (3D-EDD) [RD-10] are built using the Topside sounder model - assisted Digisonde profiler [RD-24, RD-27] driven by two sources of real-time measurements: (a) sub-peak (bottomside) electron density profiles (EDP) provided by the Pan-European network of Digisondes and (b) GNSS TEC parameters calculated at the Digisonde locations. Seamless connection of the bottomside EDP with TEC-driven profiles above hmF2 results in a 3D specification of electron density from the bottom of the ionosphere up to the GNSS orbit altitude of about 20,000 km. Not only such 3D EDD specification reproduces signatures of propagating TIDs, but also it can be used to detect the altitude of the maximum plasma density perturbation.

3.5.2 Description of the algorithm as implemented

The main users' requirements connected with this methodology are:

1. Provision of 3D EDD maps over Europe and Africa regions, for the bottomside and the topside ionosphere.
2. Detection of LSTIDs in real-time.
3. Indication of the altitude of the maximum disturbance

In the following sections we present the TaD model algorithms and their implementation. Computations begin with 1D EDP over Digisonde observatory locations and then extended by means of 2D mapping to the 3D case over a region.

3.5.2.1 The 1D version of the EDD TaD model

The TaD model has three components:

a) the Topside Sounders Model (TSM) subroutine [RD-24] that provides the empirical functions for the O^+- H^+ transition height (h_T), the topside electron density scale height (H_T) and their ratio $Rt=H_T/h_T$, derived solely from the Alouette/ISIS data;

b) the Topside Sounders Model Profiler (TSMP) subroutine [RD-25, RD-27] that offers analytical formulas for obtaining the shape of the vertical plasma distribution in the topside ionosphere and plasmasphere based on TSM parameters and on the F layer maximum density (NmF2), its height (hmF2) and its scale height (Hm) at its lower boundary, derived from Digisondes. This profiler models separately the O+, H+, and He+ density distributions in transition region between the topside F region and plasmasphere, extracted from the analysis of the electron density profiles from ISIS-1;

c) the final TaD subroutine that performs the necessary transformations to the Digisonde autoscaled scale height so that the integrated TSMP electron density from the F layer peak to GNSS orbits can be finally adjusted to the measured GNSS TEC at the Digisonde location [RD-20, RD-26]. In section 3.5.2.6 we describe the basic TaD model's components with their input and output parameters.

An example of the application of the TaD model in the Ebro Digisonde location, is presented in Figure 23.

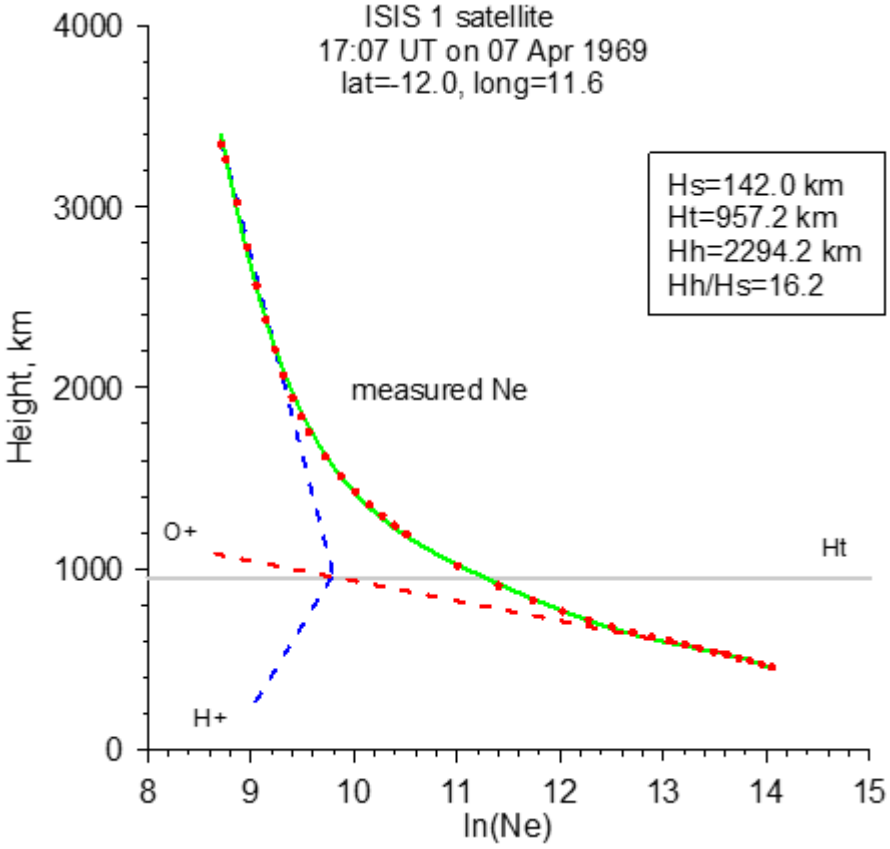

Figure 23. A sample Ne profile obtained by 3D EDD method
Red dots represent ISIS 1 data points, the green line is a smoothed approximation of the Ne profile, pink and dashed blue lines represents O^+ and H^+ distributions. The gray line marks the transition height h_T.

The sample Ne profile in Figure 23 was obtained on 05 February 1969, a time period when ISIS 1 topside sounding profiles were available. Red dots represent ISIS 1 data points, the green line is a smoothed approximation of the Ne profile, pink and dashed blue lines represents O^+ and H^+ distributions. The gray line marks the transition height h_T. It was assumed that the H^+ scale height (H_P) at least 500 km above the transition height h_T can be represented as the

maximum of dh/d(lnNe), in order to avoid influence of O^+ distribution. In average, the plasmaspheric part of the measured Ne profiles extends 2500 km above the transition height. The procedure of calculating the scale height H_P requires at least three measured points for taking a regression line, but in average, the regression involves the 5 uppermost data points.

3.5.1.2 Description of the 3D EDD procedure

The 3D EDD maps are created using ionospheric characteristics extracted from the Digisonde ionograms that are obtained from the DIAS database [RD-19], in order to ensure real-time availability of critical ionospheric data. To develop 3D EDD maps, a grid is drawn over the area extended between -10˚ and 25˚E in longitude and between 35˚and 60˚N in latitude, with resolution of one degree on both coordinates which defines 900 grid nodes. TaD profile parameters: topside scale height H_T, transition height h_T, and plasmasphere scale height Hp, and Digisonde provided foF2, hmF2 are calculated at each grid node using the Polyweight interpolation procedure, implemented in TaD software. For the calculation of the grid values, data from eight European Digisondes are used, and their coordinates are given in Table 7.

Table 7. **European Digisonde coordinates used for 3D EDD computation**

Code	Stations	Latitude	Longitude
EA	Arenosillo	37.1	-6.7
EB	Ebre	40.8	0.5
CH	Chilton	51.6	-1.3
JR	JuliusRuh	54.6	13/4
AT	Athens	38.0	23.5
RO	Rome	41.9	12.5
PQ	Pruhonice	50.0	14.6
DB	Dourbes	50.1	4.6

For the tests presented here, TEC values are extracted from ROB (Royal Observatory of Belgium) GNSS-TEC maps [RD-21] and are assigned to the grid node locations. Maps of TaD produced at 13:45 UT on 08 March 2012 are shown in Figure 24. The magnitude is color coded

with scales on the right of the maps. The black crosses show locations of Digisonde stations used in the analysis. Once profile parameters and TEC values are assigned to each grid node, TaD calculates the vertical ED profiles and adjusts their integrals to the corresponding TEC values. The ED profiles at the grid nodes constitute the 3D EDD over Europe. Electron density value at locations with arbitrary coordinates and height are calculated in two steps: 1) the 5 TaD parameters NmF2, hmF2, H_T, h_T, and Hp are obtained at the specific location by the linear interpolation from the neighbor grid nodes, and 2) ED for the respective height is calculated by the profile expression presented in section 3.5.2.6.

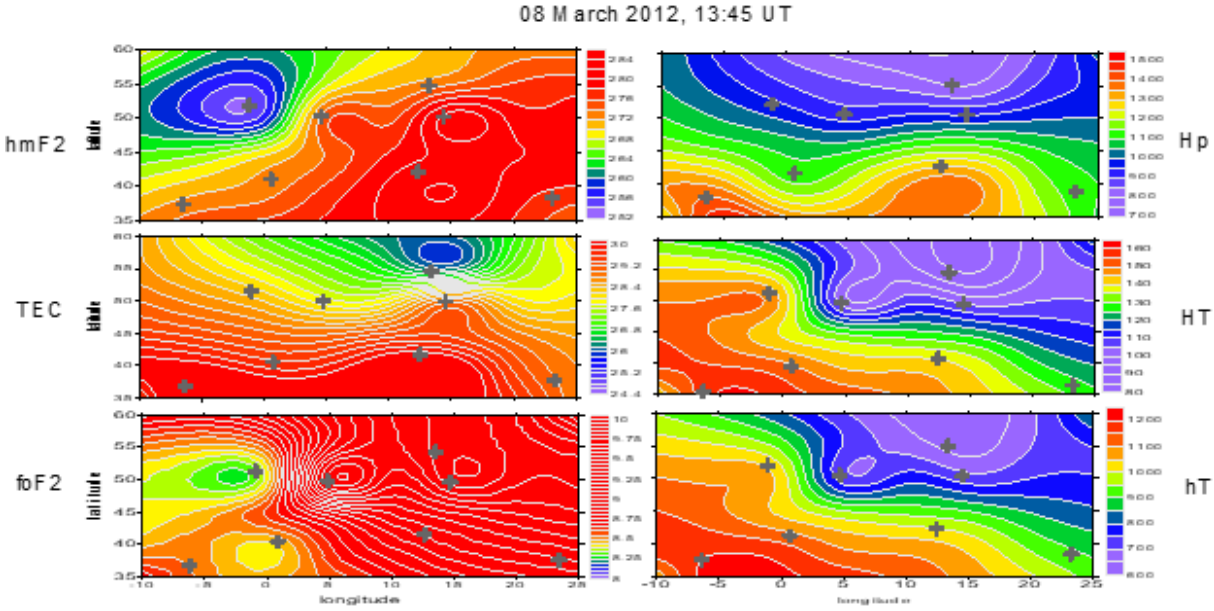

Figure 24. Maps of TaD profile parameters taken at 13:45 UT on 08 March 2012. Magnitudes are color coded with scales on the right of each map. Location of Digisonde stations are shown on each map by the black crosses.

3.5.2.3 Visualization of 3D EDD maps

The maps are the result of the visualization of EDD in the region of space with the mapping area as the base and height range between 200 km and 1150 km. In this height range ED changes more than 3 orders of magnitude, much more than in horizontal plane at any fixed height. This fact makes difficult the color visualization of EDD variations in the whole 3D space. If we use a dynamic range of 4 orders of magnitude to cover the ED height variations, the horizontal variations will be strongly depressed and not visible in color coded maps. If we choose to represent the horizontal variations better, because they are physically more

significant, then we have to produce the fixed-height latitude/longitude maps in different magnitude ranges. Here we chose the second option but for comparison, we present in Figure 25(a) the fixed-height maps on a single range of 4 orders of magnitude, showing slices of log(ED) at 200, 400, 600, 800, and 1000 km for the same chosen moment 13:45 UT on 08 March 2012. The magnitude scale ranges from 9.5 to 13.5 log(ED) units. Horizontal variations in each map can be followed by the contour lines, which are drawn every 0.1 of log unit, as at every 0.5 step the contour lines are made thicker with the value labels marked on them. The color scale is shown on the right.

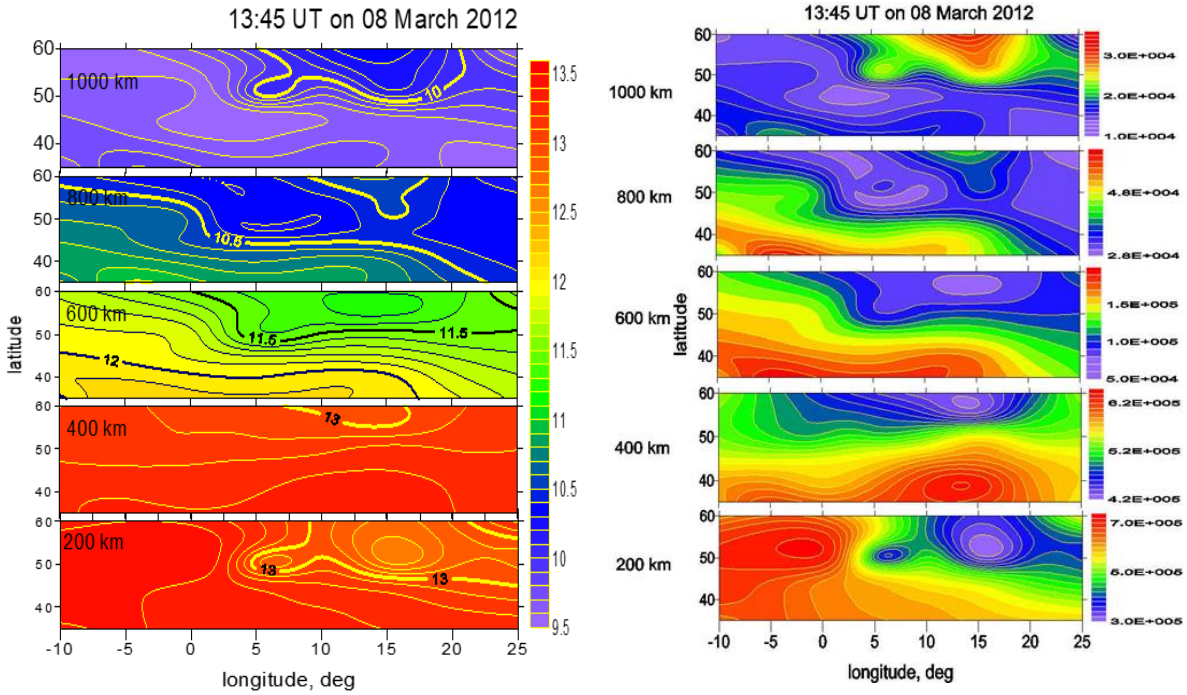

(a) (b)

Figure 25. Electron density distribution on horizontal slices between 200 km and 1000 km.

Figure 25(b) shows the same maps in linear scale, as each fixed-height map has its own magnitude range shown on the right. Now the horizontal variations of ED are better expressed. An interesting feature worth to mention is the relative increase of ED in the northern-east part of the map. It is seen from Figure 24 that foF2 also increases in this part of the map which is supported by the data from the nearest Digisonde stations Juliusruh (JR) and

Pruhonice (PQ). Indeed, foF2 and hmF2 maps differ significantly from ionosonde measurements. As will be shown below, this disturbed structure significantly changes the density along specific raypaths. Another spatial view of the same slices is presented in Figure 26, where the different altitude changes of ED in the different parts of the map are better followed.

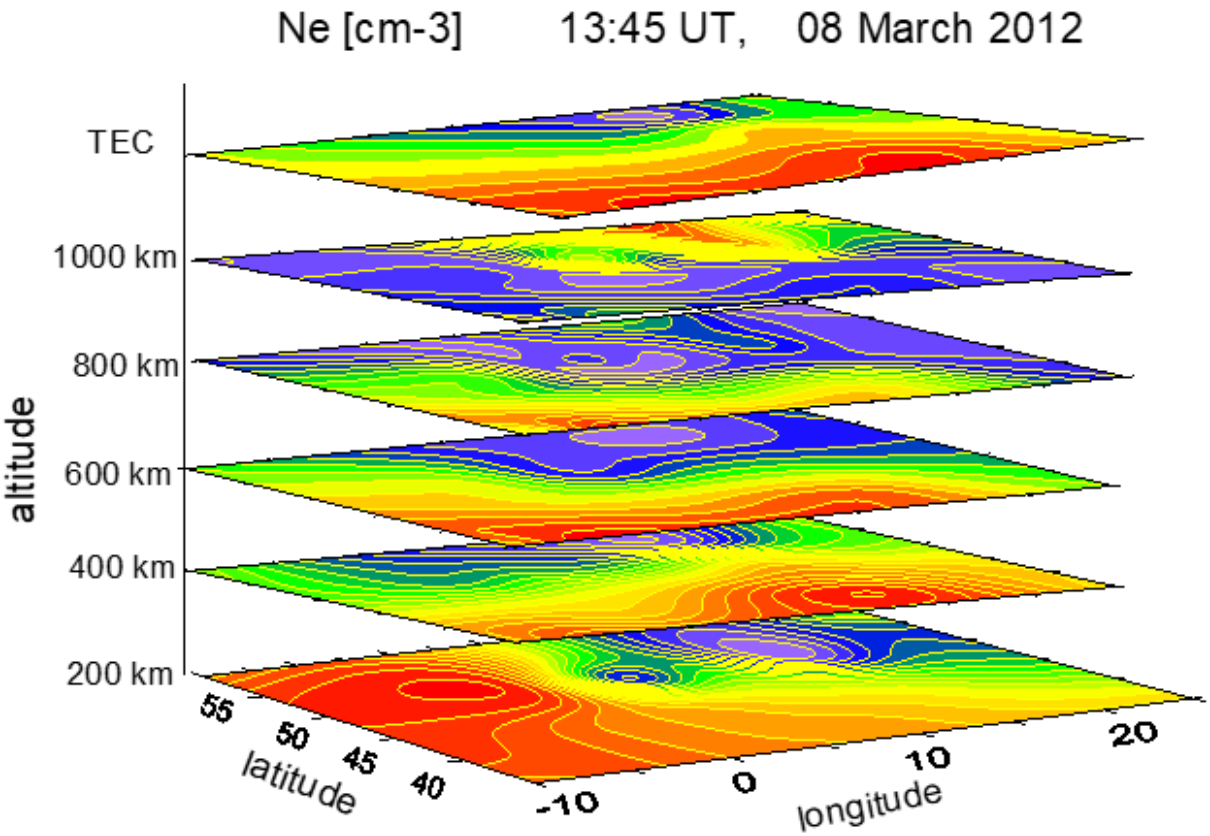

Figure 26. 3D view of electron density distribution as altitude slices. The map of TEC from Figure 24 is added at the top of the figure.

Figure 26 is composed by taking the altitude maps of Figure 25 and the TEC map which are tilted in a way to produce a 3D representation. For simplicity, the color scales are omitted. The aim of this figure is to show the EDD changes with altitude. Although the color scales at each height slice are different, the ED topology changes significantly from map to map. As expected, the increase of TEC at lower latitudes is determined by the ED increase in the F region (200-600 km maps).

In order to reveal the internal structure of the 3D EDD in a selected parallelepiped, we produced vertical slices shown in Figure 27. The base *abcd* is at 150 km, while the top *efgh* is at 1150 km. The place of each map in the parallelepiped is indicated in its upper left corner.

Depending on its place, the abscissa is longitude or latitude, while the ordinate is always altitude. The value range of all maps is the same, but the color scales are omitted for simplicity.

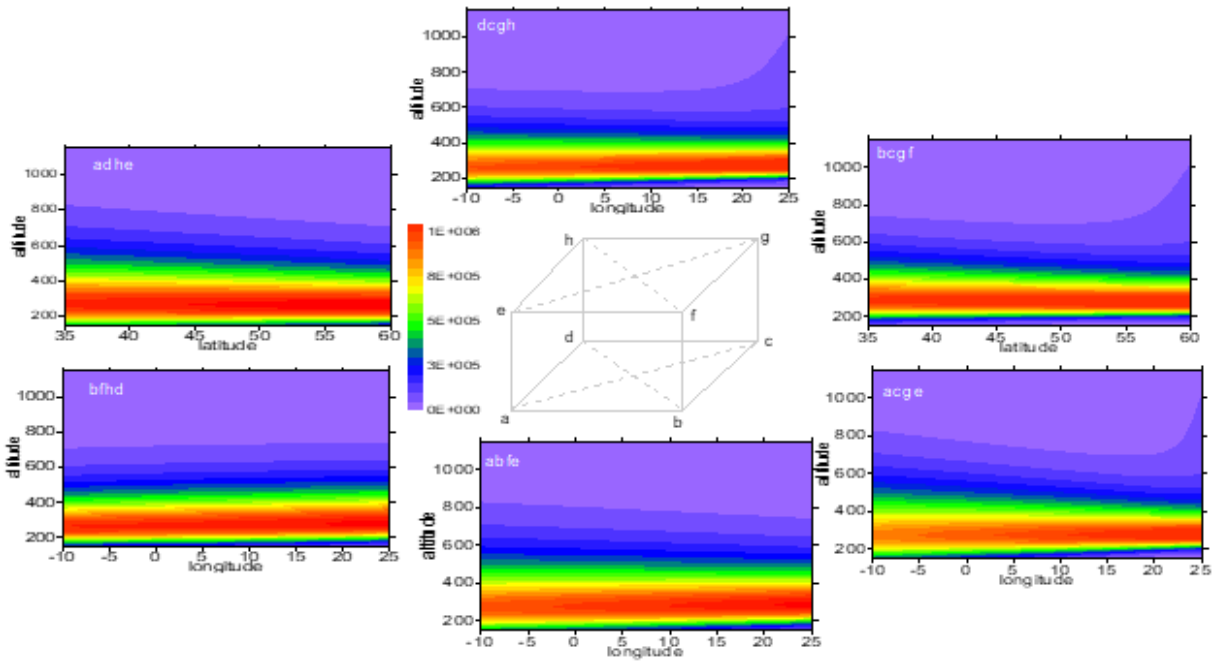

Figure 27. Vertical slices of selected parallelepiped for TID detection.
The letters in upper left corner of each map indicate the place of the slice. The maps represent the front, rear, left and right sides and both diagonals of the parallelepiped. The color scale is the same to all maps.

Having obtained the 3D EDD in the chosen parallelepiped, TaD procedure can reconstruct the EDD along arbitrary raypaths within the volume. Figure 28 shows two vertical profiles *ae* and *cg*, and two slant profiles: *ag* and *ce*, all lying in the diagonal slice *acge*. The upper map represents this diagonal slice with the raypaths marked in different colors. The projections of these raypaths are also marked in the top side. Corresponding ED profiles are shown on the right plot.

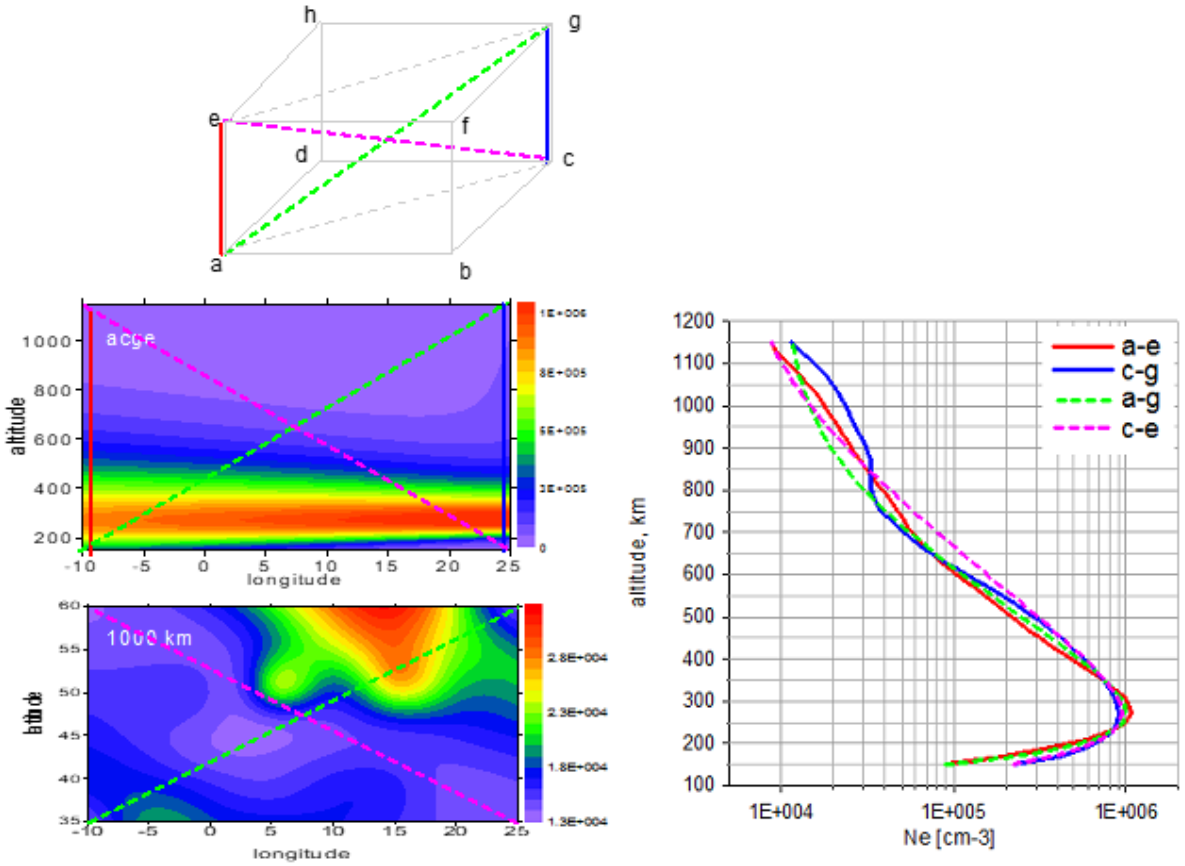

Figure 28. Electron density profiles along raypaths.
Two vertical (red and blue curves) and two slant (green and pink dashed curves) raypaths are shown, all lying on diagonal slice *acge* (the upper map). The lower electron density map at 1000 km shows the enhanced density at its north-east part, which supports the interpretation of the density increase in the green profile.

The vertical profiles are represented by the red and blue thick curves, while the slant profiles are shown by pink and green dashed curves. The slant profile *ag* starts from the red vertical profile at 150 km and merges the blue one at 1150 km. The other slant profile *ce* starts from the blue vertical profile and ends at 1150 km in the red one. It is interesting to note the large difference in the density of the two vertical profiles, which reflects the density increase above 800 km in north-east part of the lower map. The green slant profile *ag* also shows this feature when entering the enhanced density zone.

The TaD profiles include the bottomside Digisonde profile and the profiles above hmF2 extended up to 20,000 km. Therefore, the 3D EDD procedure can reconstruct EDD in the

parallelepiped with the mapping area as a base and altitude range between the E region (around 100 km) and GNSS orbit heights (20,000 km). This means that TaD procedure can obtain the EDD between two arbitrary points of the space within defined volume, as well as along the raypath between a GNSS satellite and ground-based or LEO satellite receiver. Selected raypaths are marked in the maps and in the parallelepiped at the top.

Several 3D EDD possible graphical representations are shown here. In TechTIDE User Interface we will consider what is the best graphical format to be adopted, based on users' requirements.

3.5.2.4 Detection of the LS TID activity

The TaD model has the advantage to provide the electron density at various heights. In Figure 29 we present the results from the 1D version of the TaD model over the Digisondes in Dourbes and Roquetes for two disturbed days 7 and 8 March 2012 [RD-11].

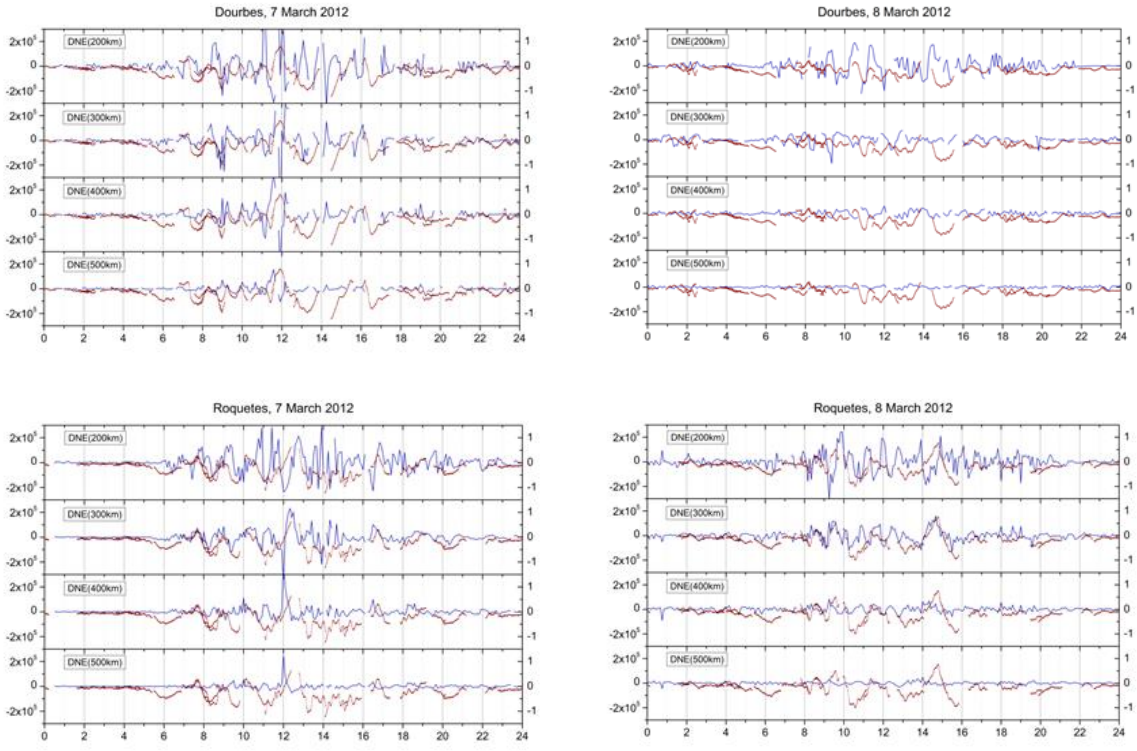

Figure 29. Coincident variations of detrended Digisonde electron density dNe and dSTEC from GNSS. dNe and dSTEC are obtained for two locations (Dourbes and Ebre) during 7 and 8 March 2012. dNe are calculated with the TaD model at altitudes ranging from 200 to 500 km (blue color). The slant TEC variations (dSTEC) from GPS receivers at the same locations are overplotted in red.

These Digisondes operate at 5 minutes cadence which allows detection of LSTIDs. Together we present for comparison the slant TEC (sTEC) from GPS receivers co-located with these two Digisondes. The sTEC plotted in Figure 29 are calculated with datafiles of 30 sec resolution, received from GPS satellites with elevation larger than 70 degrees, applying the single station solution. Both TaD ED and GPS TEC perturbations are de-trended with 60 min running average background.

From the inspection of Figure 29, the main remark is that perturbations in the Ne calculated with the TaD model are concurrent with the sTEC perturbations. Another remark is that the best visual correlation between Ne and sTEC is noticed at 300 km altitude. This might be the assumption made by the single station solution method that the ionosphere is a thin layer at 300 km altitude. The correlation between Ne and sTEC perturbation at 300 km is more prominent in Roquetes. It should be considered that Roquetes Digisonde sampling is 25 kHz in frequency and 2.5 km in height. The corresponding sampling rate in Dourbes Digisonde is 45kHz and 2.5 km. The fine resolution in frequency leads to more accurate results and therefore we consider that Roquetes records provide a very realistic representation of the ionospheric structure. Data from Digisondes used for this study are extracted from ionograms with the ARTIST 5.0 software that performs with superior performance compared to previous versions. Nevertheless, we cannot neglect the case of artificial results due to scaling errors, therefore the samples of the ionospheric parameters used in this paper have been checked for their integrity. If TaD is going to be used operationally with Digisonde data to routinely calculate Ne perturbations at different heights, additional filters need to be applied in the data to ensure that TaD can reach its best performance and support efficiently satellite systems that require Ne information of high precision.

The general conclusion from Figure 29 is that the perturbations obtained with the two methods, start and end simultaneously. Their pattern cannot be directly compared, because GPS receivers provide the integral of the electron content from the ionosphere up to the plasmasphere, whereas TaD model provides the electron density at each selected height. GPS TEC shows most of the time a sinusoidal variation, implying a propagation of a wave front over the specific location. TaD Ne perturbations reveal a more complex pattern.

3.5.2.5 Indication of the altitude of max disturbance

Considering the requirements of the users and based on the primary output of the 3D EDD code, the specification of the height of the maximum disturbance due to TIDs is the value-added product that can be provided. Below we provide the product design concept:

The 3D EDD code has the capability to provide the integral of the electron density over any part of the path between the lower altitude of the ionosphere (i.e. ~ 90 km) up to the GNSS

heights (i.e. 22,000 km). The TIDs mainly perturb the ionization at the F2 layer however there are cases where the TID travel upwards or downward depending on their source. Using the EDD results from the 3D EDD code, we can calculate the time and spatial gradients of the partial electron density integrals over the E layer, the F layer, the whole bottomside and parts of the topside ionosphere for a specific geographic region. The comparison of the gradients of the maps can give us an indication regarding the ionospheric layer where the maximum perturbation is detected. Some basic TID characteristics such as the velocity and the direction of propagation can also be extracted, especially for large scale TIDs.

3.5.2.6 Implementation of 1D version

The basic routines of the 1D version of the TaD EDD code are given in Table 8.

Table 8. **The TaD subroutines for the topside reconstruction at a single point**

Input Parameters	Subroutine	Output
Month, LT, glat, f10.7, Kp	**TSM**: Topside Sounders Model Analytical functions based on Alouette, ISIS-1,-2 topside profiles (Bilitza, 2001)	Empirical functions of parameters H_T: topside scale height (i.e., H_{O+}) h_T : transition height R_T: ratio H_T/h_T
H_m, k, R_T, h_mF2, N_mF2 and *glat*	**TSMP**: Topside Sounders Model Profiler Analytical functions based on ISIS-1 topside profiles to model plasmaspheric scale height	Empirical functions of parameters H_P: plasmaspheric scale height (≡H_{H+}), $H_P=H_T(9cos^2 glat+4)$ *Ne*: electron density profile in the topside ionosphere and plasmasphere $N_e = N_{O^+}(h) + gN_{O^+}(h_T)exp\left(-\frac{\lvert h-h_T\rvert}{H_p}\right) + (1-g)N_{O^+}(h_T)exp\left(-\frac{\lvert h-h_T\rvert}{4H_T}\right)$ $N_{O^+}(h) = Nm\ exp\left\{-\frac{1}{2}\left[\frac{h-hm}{k\ Hm} + 1 - exp\left(\frac{h-hm}{k\ Hm}\right)\right]\right\}$ g is the ratio N_H+ / N_O+ at h_T k is the correction parameter that converts H_m (the neutral scale height) to make it compliant with H_T

Digisonde parameters at the height of maximum density (*hmF2*, *foF2*, H_m), R_T, and vTEC (GNSS) at the Digisonde location	**TSM-assisted Digisonde Profiler** Calculation of the actual profile over each Digisonde location to update TSMP with current Digisonde and TEC (GNSS) parameters	$$N_{\square} = N_{O^+}(h) + gN_{O^+}(h_T)exp\left(-\frac{\lvert h-h_T\rvert}{H_p}\right) + (1 - g)N_{O^+}(h_T)exp\left(-\frac{\lvert h-h_T\rvert}{skH_m}\right)$$ where $s=H_{He+}/kH_m$ The integral of the Ne profile can be adjusted to the measured vTEC by varying solely the correction parameter *k*

The empirical TSM functions are updated in real time with Digisonde data at the height of the maximum electron density (hmF2) and with TEC data from GPS receivers co-located with the Digisondes.

The 1D version is already available in TechTIDE repository for offline execution.

3.5.2.7 Implementation of 3D version

The 3D mapping routines are based on the Polyweight method, a modification of the 'Inverse Distance to a Power' gridding method (Davis, 1986, Franke, 1982). The Polyweight interpolation method calculates parameter values at the grid nodes. At each node (x_0,y_0) it approximates the mapping parameter with a linear function of latitude and longitude, taking all data points with weights.

The linear function is $p(x,y) = C_{00} + C_{10}(x-x_0) + C_{01}(y-y_0)$ (1)

The fit minimizes $\Sigma w_i(z_i - p(x_i,y_i))^2 \rightarrow min$ (2)

where the weight w_i is: $w_i = \frac{1}{[\sigma+(x_i-x_o)^2+(y_i-y_o)^2]^q}$ (3)

The data points (at Digisonde locations) have coordinates x_i and y_i and the parameter value z_i (i=1…N), N is the number of all data points, is a constant which prevents the weight w_i for getting too large when a data point (x_i, y_i) is very close to the grid node (x_0,y_0). The weighting power q is taken 0.75 and the smoothing parameter =10 [deg^2]. A linear function $p(x,y)$ is calculated for each grid node (x_0,y_0) by taking all data points (x_i, y_i, z_i), as its value is assigned

only to the given grid node (x_0,y_0) and nowhere else. Interpolation procedure is repeated by calculating the plane $p(x,y)$ for each grid node (x_0,y_0) in the mapping area. In this way, all data points participate in calculation of each of the grid nodes but each time with different weight w_i. In this study, we have used data from eight European Digisondes, but frequently only 5-7 of them provide data available for the mapping. To increase the number of data points, we take the four corner grid nodes and calculate their parameter values in advance by using the Inverse distance method with the same weighting power 0.75. We then include these values as additional data points complementing those of DIAS ionosondes. Inclusion of corner grid points avoids the appearance of unrealistically high or low parameter values around the corners of the map where ionosonde data are not available.

It is important to know to what extent the Polyweight model represents the underlying Digisonde data. By design, this model does not accurately match Digisonde foF2 and hmF2 parameters because it employs the least-squares-based interpolation method (eq. 2). We have made numerous experiments to find a proper compromise between the exact match, which produces a 'bull eyes' topology around the stations and a more reliable smoothing of mapped parameters. The parameter values of and q are the result of that optimization. For the particular geomagnetically disturbed period subject to this analysis, we give in Table 9 the deviations of the mapped and measured foF2 and hmF2 over the stations.

Table 9. **Deviations in % between measured (sta) and mapped (PW) values of foF2 and hmF2 calculated for the epoch 13:34 UT on 8 March 2012**

code	Lat	Long	foF2, MHz			hmF2, km		
			sta	PW	diff %	sta	PW	diff%
EA	37.1	-6.7	8.65	8.55	1.14	276.0	272.9	1.14
EB	40.8	0.5	8.45	8.47	-0.26	278.1	272.9	1.91
CH	51.6	-1.3	8.62	8.33	3.59	219.1	253.8	13.68
JR	54.6	13.4	9.46	9.26	2.20	273.9	273.6	0.11

AT	38.0	23.5	-	8.95	-	-	277.0	-
RO	41.9	12.5	8.92	8.92	0.078	287.1	281.0	2.17
PQ	50.0	14.6	9.32	9.27	0.57	285.5	282.8	0.96
DB	50.1	4.6	9.39	9.22	1.84	273.8	274.4	0.22

The three columns in Table 9 for both foF2 and hmF2 give the measured (sta), mapped (PW) and the difference in percent (diff %) for each station in a row. Athens ionosonde does not provide data at that time and hmF2 value of Chilton is exceptionally low compared with those of the other stations. On average, the deviation between the measured and mapped values is 2-3 %, which is clear evidence that the Polyweight method assures a satisfactory representation of ionosphere over the Digisonde stations.

The 3D version will be made available to run online. The user will have the possibility to select the area (either a single point or a region, and then given the region the user can select a vertical, horizontal or slant surface), the type of output (graphical or ASCII).

The TaD code is ready for implementation in Europe and in Africa.

3.6. HTI Method

The height-time-reflection intensity (HTI) methodology [RD-12] is similar to the technique producing range-time intensity (RTI) radar displays within a given time interval. The application of this method in TechTIDE enables the identification and tracking of the TID activity over each Digisonde station by using the actual ionograms produced over each station. This technique considers an ionogram as a ''snapshot'' of reflected intensity as a function of virtual height and Digisonde signal frequency, and it uses a sequence of ionograms to compute an average HTI plot, (for a given frequency bin) that is essentially a 3-D plot of reflected signal-to-noise ratio in dB as a function of height within a given time interval. This display reveals dynamic changes in the ionosphere. Figure 30 depicts TID-like variations on typical HTI plots corresponding to a Digisonde frequency band, of 2.0-4.0 MHz for three stations over Europe. The periodicity of the dominant wave activity is estimated by applying spectral analysis to points of maximum intensity reflected at certain F-region virtual heights indicated by black dots on these HTI plots.

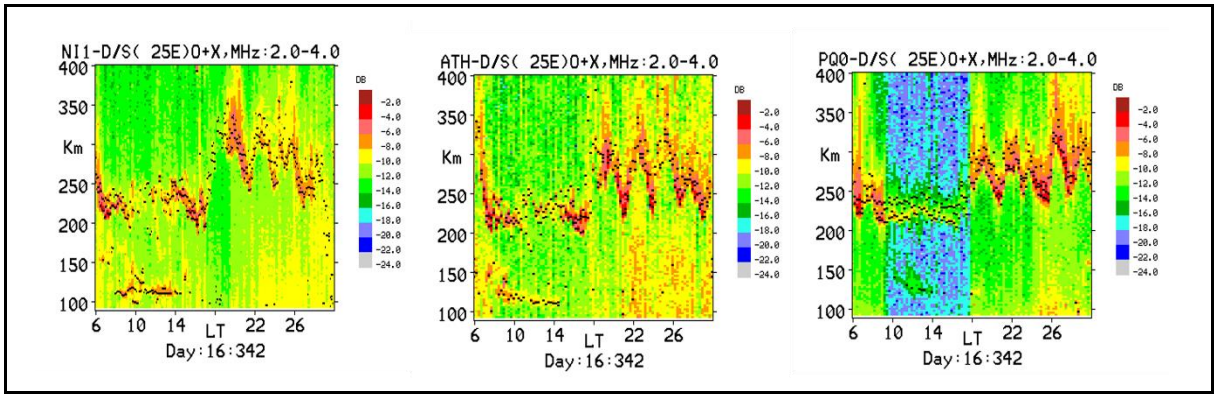

Figure 30. HTI plots over Nicosia (left), Athens (middle) and Pruhonice (right) for December 7, 2016.

3.6.1 Description of HTI Method as implemented

The HTI Method uses raw ionograms obtained from 9 european digisondes and 4 digisondes from South Africa. It also uses near real time foF2 data from the GIRO DIDBase Fast Chars (http://giro.uml.edu/didbase/scaled.php) in order to estimate the optimal frequency bin within which the F-region trace of the ionograms will be processed at each instant during a 24 hour interval. For each ionogram at the appropriate frequency bin a virtual height profile of signal strength is obtained (indicated by different colour in Figure31(a).

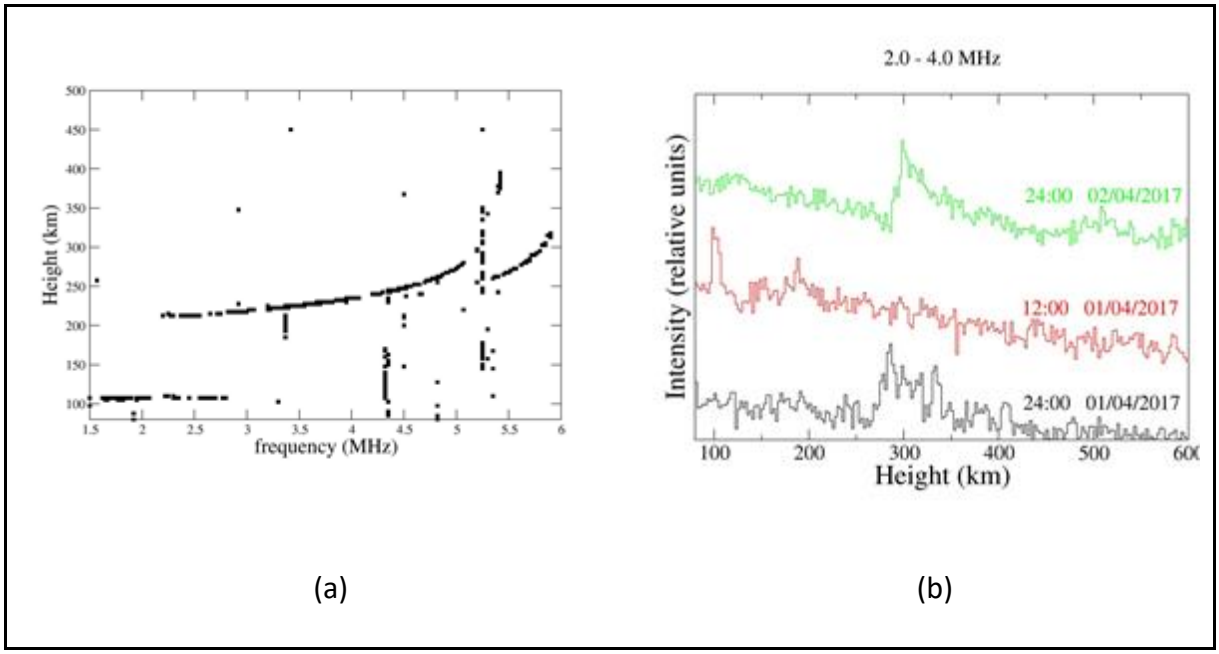

Figure 31. (a) Ionogram ready to be processed by HTI. (b) Output virtual height intensity profile for three different ionograms at a frequency bin of 2-4 MHz.

By estimating the virtual height of the points of maximum intensity within each profile and by superimposing these resulting from each ionogram an HTI plot may be determined (Figure 32). At times strong reflections from sporadic E (Es) are received (indicated by the circles in Figure 32) that are strong enough to mask F-region reflections so appropriate procedures have been applied to treat these points as outliers and not consider them in the subsequent spectral analysis.

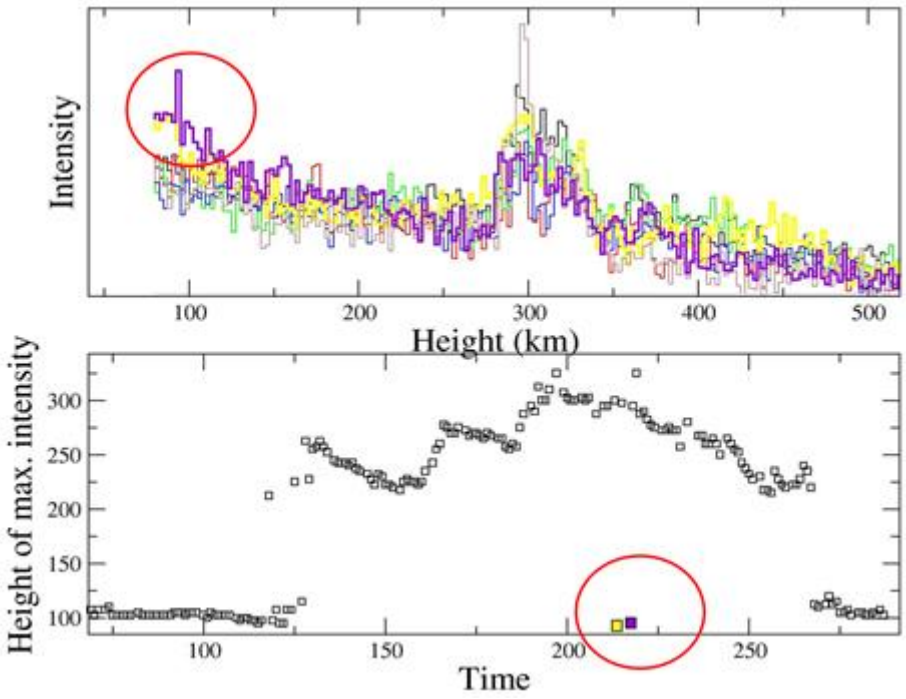

(a)

(b)

Figure 32. (a) Estimation of reflection intensities at various F region virtual heights including E region outliers. (b) Resultant HTI plot indicating strongest signal reflection points for a full day.

3.6.1.1 Spectral analysis on HTI plots to infer LSTID periodicity

The points of maximum intensity are extracted from the HTI density with an appropriate statistical error. We aim in fitting the data with a superposition of a low period signal (in the range of 1-3 hours) with an arbitrary number of higher period signals, which essentially correspond to established background ionospheric activity. The low period signal aims in capturing possible persistent TID activity during a chosen time interval.

We employ a statistical model fitting technique, Athens Model Independent Analysis Scheme (AMIAS) which is appropriate for analyzing data with large error. The starting point of AMIAS is a set of measurements with the associated statistical errors, in this case the points of maximum intensity. The model we use for this analysis is given in Equation 3.6.1 where the first period, T_1, is in the range between 1 and 3 hours. AMIAS determines a probability distribution function (PDF) Π(Ar) for each fit parameter Ar. The estimates for the values of the fit parameters and their uncertainties are the expectation values and the standard deviations

of the corresponding PDFs given in Equations 3.6.2-3.6.3. The PDF for the complete set of fit parameters is defined by Equation 3.6.4.

AMIAS is able to handle a rather large number of parameters using Monte Carlo techniques, i.e., it is suited to study several superimposed periodicities. The key property of our methodology is that model parameters that contribute to the solution have well defined distributions which are not biased when 'insensitive' parameters are inserted in the model i.e. we can selectively search in a number of ranges for the possible periodicities.

$$f(t) = a_0 + \sum_n a_n \sin\left(\frac{2\pi}{T_n} + \varphi_n\right) \tag{3.6.1}$$

$$\bar{\mathcal{A}}_r = \int d\mathcal{A}_r \mathcal{A}_r \Pi(\mathcal{A}_r) \tag{3.6.2}$$

$$\sigma(\mathcal{A}_r) = \left(\int d\mathcal{A}_r (\mathcal{A}_r - \bar{\mathcal{A}}_r)^2 \Pi(\mathcal{A}_r) \right)^{1/2} \tag{3.6.3}$$

$$P(\mathcal{A}_1, \mathcal{A}_2, \ldots) = \frac{1}{N} e^{-\chi^2/2} \tag{3.6.4}$$

3.6.1.2 Upgrading for near-real-time operation

At present the HTI method and the spectral analysis are applied off-line for test cases characterized by TID activity. The test cases and the required data are obtained from the TechTIDE open access repository and on time intervals when persistent TID activity of significant amplitude is observed by the Net-TIDE experiment (http://tid.space.noa.gr). The final code will provide near-real-time information of detected LSTID activity above given Digisonde sites within European and South African regions.

3.6.1.3 Some identified problems

During summer months the occurrence of strong sporadic E (Es) increases significantly over European stations (especially low latitude stations). As a result a lot of ionograms become unusable for processing using HTI because of the fact that the F region can not be illuminated by Digisonde signals that are completely blocked by strong (blanketing) Es layers. This can last for extended periods of time as shown by a series of ionograms over Nicosia in 30 June 2014 in Figure 33. Figure 34 shows the corresponding HTI plot which exhibits absence of F layer information within the time interval indicated by the red oval. For this time period, the HTI plot for the corresponding station will not contain any F region reflection points necessary for the spectral analysis to operate correctly as this will appear as an extended gap in the HTI plot. Therefore at times when strong Es appears, increased foEs from the auto-scaled real-time characteristics in conjunction with lack of foF2 autoscaled values indicating absence of F layer information must be utilized to detect these circumstances and issue a warning.

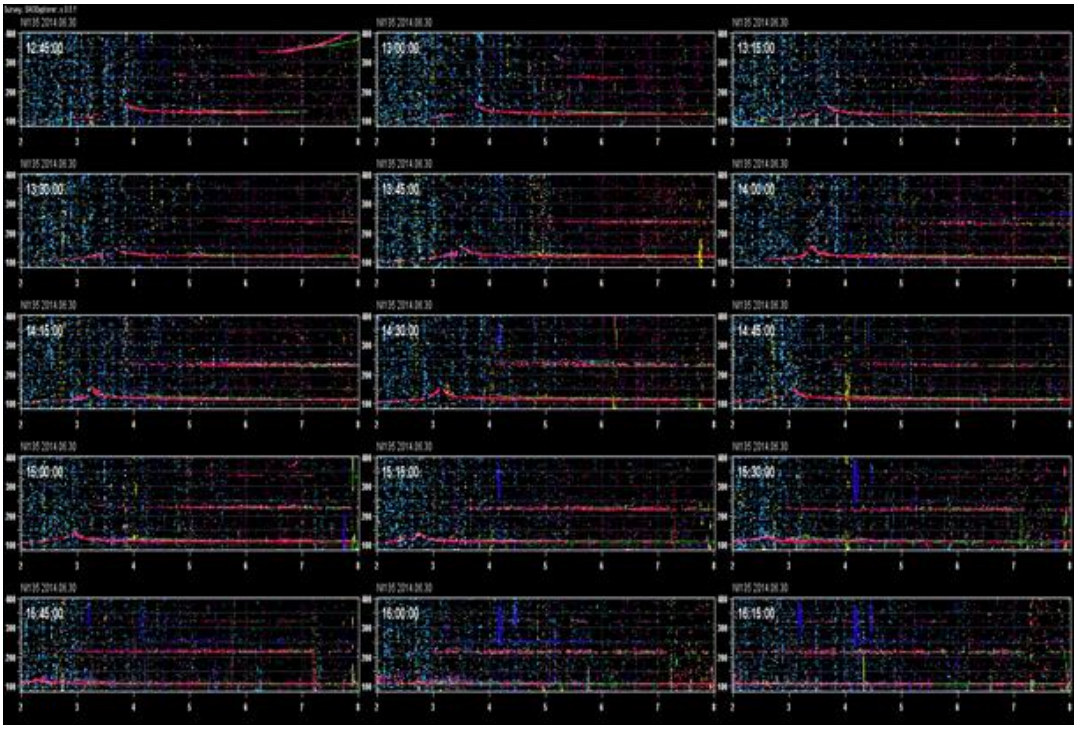

Figure 33. Series of consecutive ionograms with strong (blanketing) Es for 30 June 2014 over Nicosia station (NI135).

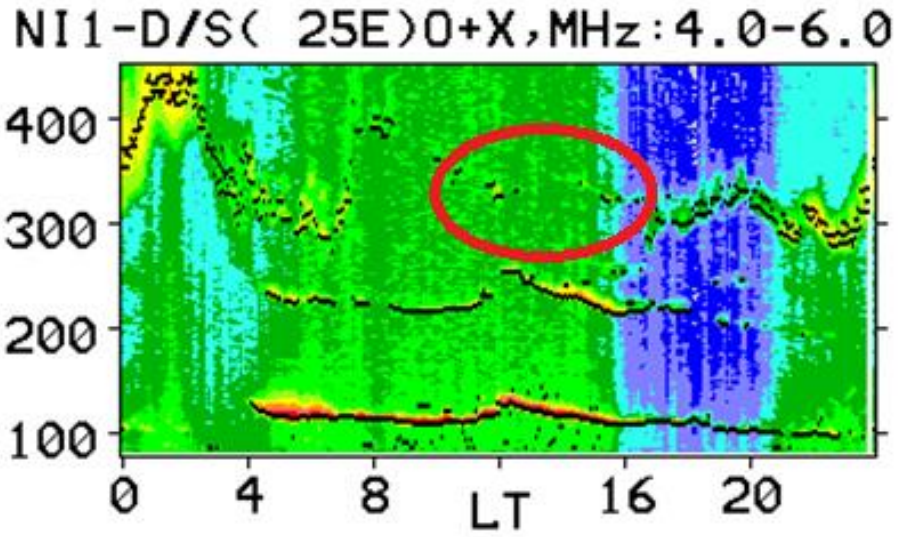

Figure 34. Example of HTI plot for 30 June 2014 at Nicosia with F layer data gap during strong Es.

3.7. CDSS Method

3.7.1 Founding Principles of CDSS-MSTID Method

In general, Doppler sounders evaluate *motion* of the reflector by inspecting the Doppler shift of the received signal frequency. High-frequency Doppler sounding of the ionosphere detects the Doppler effect in the ionospherically propagating signal; observed frequency shift can be associated with (a) bulk plasma motion (that involves mass transfer), (b) wave plasma motion (that involved propagation of the disturbances, i.e., deviations from the steady background), and (c) ionization/recombination processes (that change plasma density and therefore reflecting location). Quasi-periodic oscillations in the Doppler frequency of the sounder signal are attributed to the overpassing TID that results in slow altitude variations of the reflecting area in the ionosphere [RD-13, RD-23].

The Continuous Doppler sounding (CDS) uses continuous-wave (CW) signal that propagates between spatially separated transmitter and receiver locations via the ionospheric channel. CDS System (CCDS) is a multi-location distributed network of CDS instruments capable of detecting traveling disturbances as they propagate across the network. Similarly to the HF Interferometry method presented in Section 3.2, CCDS records can be inspected to locate the

same disturbance in all radiolinks and apply *triangulation* technique to determine its phase velocity vector.

CDSS-MSTID refers to the CDSS configuration with <100 km separation between its nodes, in which case the system targets the medium-scale TID waves of wavelengths below 100 km. TechTIDE consortium includes three CDSS-MSTID installations in Europe and South Africa; example configuration of transmitters and receivers in the central/north-western Czech Republic is shown in Figure 31. This CDSS operates at the sounding frequency f=4.65 MHz and includes 3 transmitters and one receiver as shown in Figure 35.

3.7.2 Description of CDSS-MSTID algorithms as implemented

Example CCDS recording of the Doppler spectrogram is shown in Figure 35. In order to distinguish individual channels of the systems in the plot, different radio paths are separated by adding +4 and -4 Hz offsets to the actual measurements.

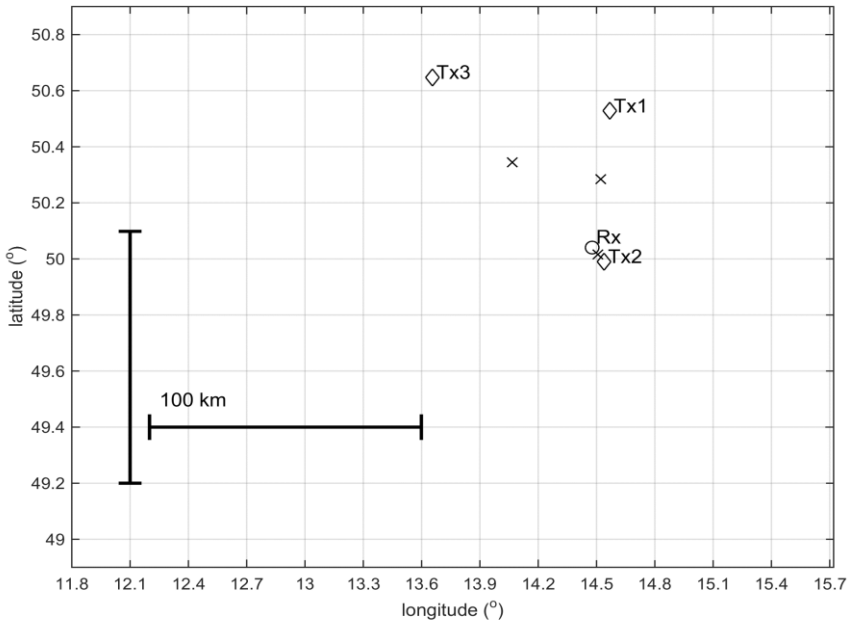

Figure 35. CCDS Installation in Czech Republic: locations of transmitters Tx1-Tx3 and receiver Rx.

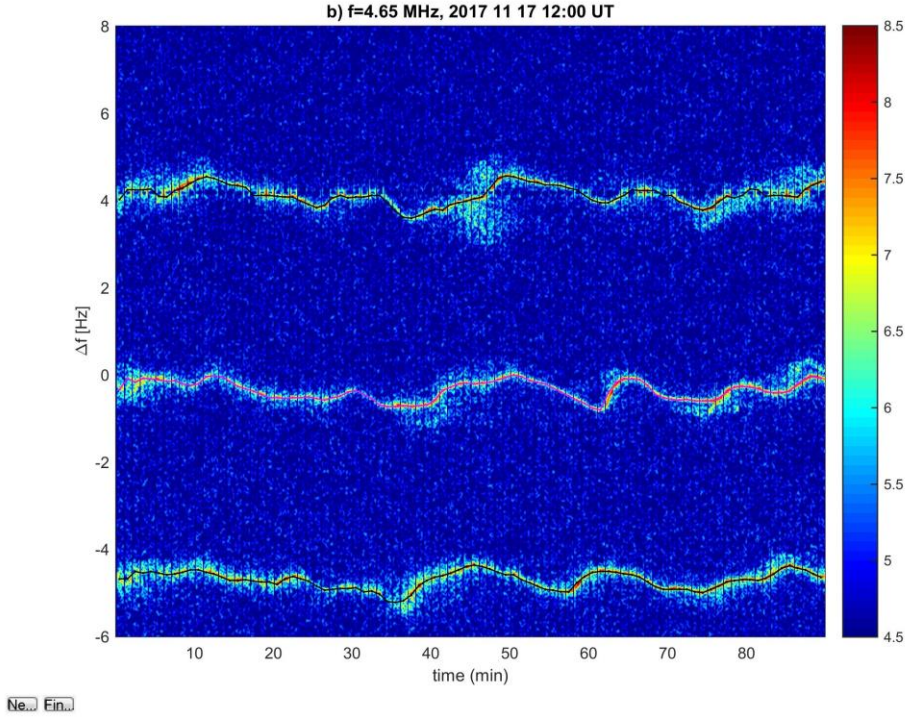

Figure 36. Example of 90-min Doppler shift spectrogram.
Maxima of spectral intensities corresponding to the Tx-Rx pairs are marked by magenta or black lines.

3.7.2.1. Input signal processing

The recorded data are processed in several steps. The whole calculation is repeated each 15-min, which corresponds to the length of recorded data files.

First, Doppler shift spectrograms are computed for the last 90-min record (example in Figure 36). The frequency corresponding to the ground wave is removed from the spectrogram. Then maxima of spectral intensities are searched in three preselected frequency bands that correspond to the frequency bands of the individual transmitter-receiver pairs. The frequencies f_{Di} corresponding to the maxima of spectral intensities for each transmitter-receiver are stored together with powers p_{pi} calculated in the narrow frequency band around these maxima (bandwidth on the order of ~0.1 Hz). In addition, powers p_{Ti} in the whole frequency bands in which the maxima are searched are evaluated (frequency band of about 4 Hz). In addition to the values of f_{Di} and p_{pi} the power ratios $r_i = p_{pi}/p_{Ti}$ are also stored to a file with 1-min step (the stored values are 1 min averages). High values of r_i approaching to 1 indicate clear signals suitable for further analysis, whereas low values of r_i indicate signals with

insignificant and featureless spectral maxima that occur e.g. during spread F conditions. Such signals are inconvenient for further analysis.

In the next step, the stored values of f_{Di}, p_{pi} and r_i are analyzed. First the offsets are removed and it is worked with values $f_{DCi} = f_{Di} - \langle f_{Di} \rangle$ further, where $\langle f_{Di} \rangle$ is the mean value over the 90-min intervals.

Next it is decided if TID or spread F likely occurred in the last 45 min and if propagation analysis of the TIDs makes sense in the last 90 min. These decisions are performed by checking if the following criteria are fulfilled.

a) TIDs are likely detected in the last 45 minutes if conditions (1) and (2) are fulfilled

$$(p_{pi} > Th1) \text{ and } (r_i >= Th2) \quad (1)$$

Condition (1) is required for at least 2/3 data points in the last 45 minutes, where *Th1*, *Th2* are experimentally found thresholds. The requirement ($p_{pi} > Th1$) ensures that sufficient signal power was received. Insufficient power is received, e.g., if the critical frequency is lower than f=4.65 MHz and the signals do not reflect from the ionosphere. As discussed before, the second requirement ($r_i > Th2$) ensures that the spectral maxima are significant.

$$\sigma_{fD} > Th3 \quad (2)$$

where σ_{fD} is the average root mean square power (in other words variance) of f_{DCi} fluctuations calculated over all three sounding paths (transmitter-receiver pairs) for data points that fulfill condition (1) and *Th3* is an experimentally found threshold. Condition (2) ensures that there are distinct fluctuations of the Doppler shifts f_{DCi}. If *Th3* is large, only large TIDs are detected.

b) Spread F is likely detected in the last 45 minutes if condition (3) is fulfilled at least for 2/3 data points in the last 45 minutes.

$$(p_{pi} > Th1) \text{ and } (r_i < Th2) \quad (3)$$

Conditions (3) means that there is relatively large power distributed in relatively large spectral bandwidths.

c) TIDs are only analyzed if condition (1) is fulfilled over the last 90 min; it is required that 7/9 of data points in the last 90 min fulfill the condition (1).

3.7.2.2. Detection and Analysis of TID events

The average variance σ_{fD} of f_{DCi} is calculated to estimate the amplitude – average oscillating velocity v_A of TIDs in the 90-min interval by equation (4)

$$v_A = -2\frac{\sigma_{fD}}{f}c \qquad (4)$$

The propagation characteristics – observed horizontal velocity and azimuth of propagation are determined as follows: first the f_{DCi} series are bandpassed filtered to keep only periods from 5 to 60 min. This aims to remove a possible high frequency noise and to remove long-period fluctuations (large-scale TIDs) that cannot be reliably analyzed with respect to 90-min intervals and with respect to the relatively small spatial scale (tens of km) of the measuring array defined by the reflection points [RD-15, RD-16].

To determine the observed horizontal velocity v_H and azimuth *AZ* of propagation three independent methods are applied i) slowness search [e.g. RD-23], ii) least squares fitting to the time delays obtained from cross-correlation of the f_{DCi} series, iii) weighted least squares fitting to the time delays obtained from cross-correlation of the f_{DCi} series; the weights are the maxima of the cross-correlation functions. The values of v_H and azimuth *AZ* that are finally reported are the mean values of v_H and *AZ* quantities obtained by the three different methods; their uncertainties are estimated as corresponding standard deviations.

The proper values of thresholds *Th1, Th2, Th3* were found experimentally by visual checking of spectrograms. Their optimum values might change if the background noise changes or if the character of signal changes, e.g., frequent splitting to ordinary and extraordinary mode or a partial spread F conditions might cause problems. Current values of *Th1, Th2, Th3* are based on initial testing on limited number of examples, and may be changed in future after getting larger experience with automatic detection.

Also, current software package uses an external value of ground wave from transmitter Tx2 that has to be removed to reliably find spectral maximum of the Tx2-Rx sky wave. This external value has to be updated if necessary (e.g. owing to long-term drift).

The information is updated each 15 minutes. So, there is an overlap as the analyzed intervals are longer. Testing site is at http://datacenter.ufa.cas.cz/TID/

3.8. AATR Indicator

3.8.1 Founding Principles of AATR Indicator Technique

Along Track TEC Rate (AATR) index was defined in the context of ESA founded ICASES project [RD-14] and it has been used to identify the conditions where a degradation in the user performance of the SBAS systems in general, and in EGNOS in particular, is expected. Figure 37 (a), shows an example of the correlation between the AATR index and the EGNOS APV1 availability over a period of two years for a station in Canary Islands (MAS1), where high values of this AATR index lead to worse performances in the EGNOS APV1 availability due to the ionospheric conditions.

The AATR index has been chosen as the metric to characterize the ionosphere operational conditions in the frame of EGNOS activities [RD-17]. This indicator has been also proposed for joint analysis in the International SBAS-Ionosphere Working Group.

3.8.2 AATR Indicator Algorithms as Implemented

In the current status of the prototype, the tool for computing the AATR works over a set of around 200 worldwide receivers, which around 100 of them are in Europe (see the maps below). These receivers collect data with a cadence of 30s.

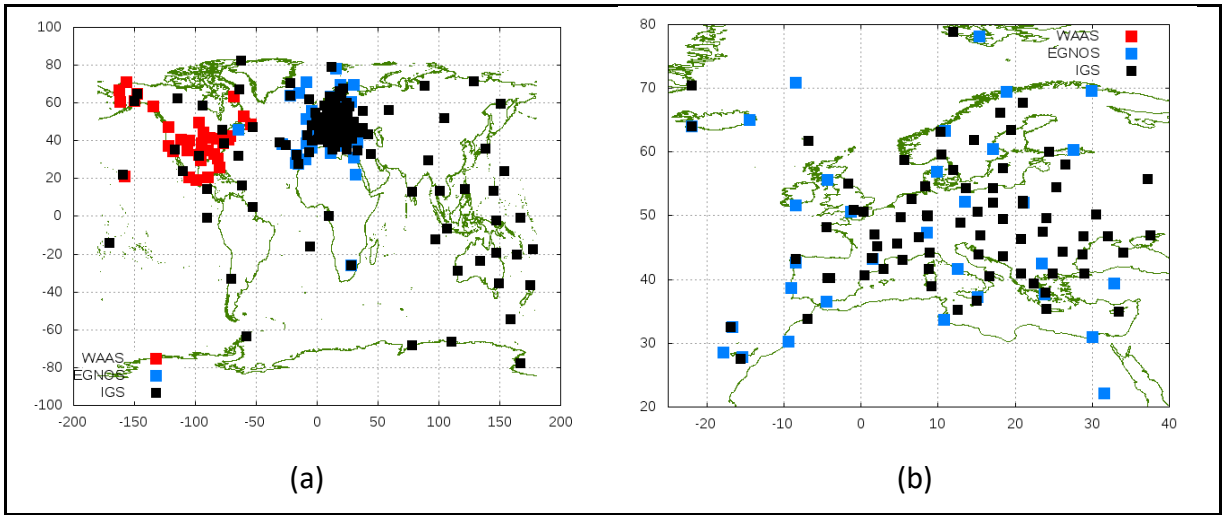

Figure 37. AATR receiver distribution

(a) World wide distribution of GNSS receivers used for computed AATR values: WAAS receivers (red), EGNOS receivers (blue) and IGS receivers (black) . (b) zoom for Europe

For each continuous receiver-satellite arc of data the tool computes the along arc rate of slant total electron content. For instance, for the satellite *j*, the receiver *i* and the time *t*:

$$AATR_i^j(t) = \frac{STEC_j^j(t) - STEC_i^j(t-30)}{30}$$

The Along Arc TEC Rate (AATR)is defined for a receiver as the RMS of the instantaneous AATR during 1 hour or 5 minutes. But, in order to diminish the effect of low elevation observations, these instantaneous rates are divided by an obliquity factor. Modeling the ionosphere as a thin layer at 350 km of altitude (h_{ion}), the obliquity factor for an elevation (ϵ) is defined as:

$$M(\epsilon) = \frac{1}{\sqrt{1-\left(\frac{R_E \cdot \cos(\epsilon)}{R_E + h_{ion}}\right)^2}}$$

where R_E is the Earth radius. In this way, AATR is defined as:

$$[AATR(t)]^2 = \sum_{j=0}^{j=\Delta T} \left[\frac{1}{M^2(\epsilon)} AATR_i^j(t+j)\right]^2$$

where (ΔT) is the time resolution of the AATR (5 minutes or 1 hour). Figure 38 depicts an AATR example for the Swedish receiver KIRU during the doy 35 in 2018.

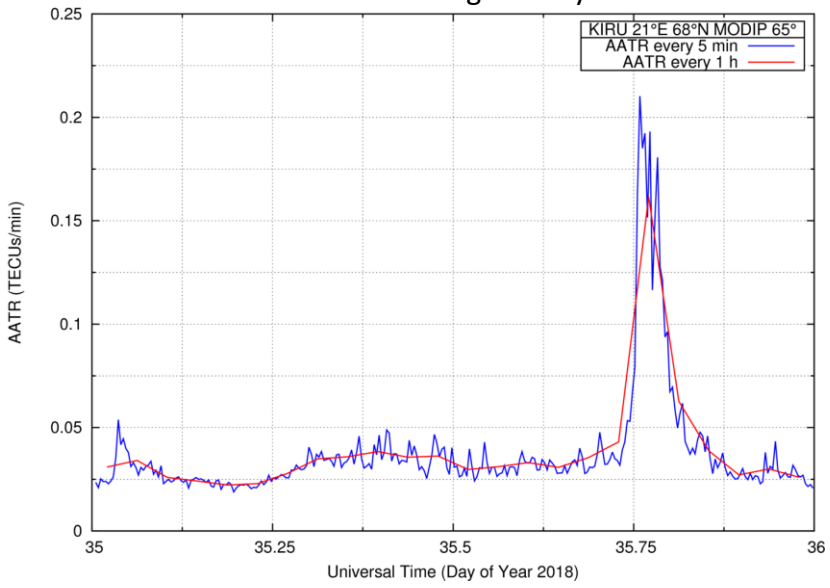

Figure 38. Example of AATR for receiver KIRU computed at 1 h and at 5m.

4. Verification of TechTIDE Algorithms: Self-verification

4.1 Verification of HF-TID method

Correctness of HF-TID method implementation was verified using synthetic data generated by means of the high-frequency radio signal ray-tracing through a realistic 3D ionosphere specification modulated by purely-sinusoidal TID waves of known properties (amplitude, wavelength, phase velocity magnitude and azimuth). Once the synthesizer produced time series of expected variation of the signal, HF-TID method was applied to detect and evaluate TID properties in the synthetic signal variation. Comparison of the derived TID with the TID used by the synthesizer was then used statistically to produce the verification report.

The signal variation synthesizer included three components:

- Background 3D model of the ionospheric density
- Model of TID modulation for superposition with background model
- Algorithm for signal raytracing through 3D ionosphere

4.1.1. Background Ne model for HF-TID Verification

Undisturbed background ionosphere can be specified as (1) horizontally stratified ionosphere defined by a single 1D Ne profile, (2) quiet-time International Reference Ionosphere (IRI) 3D model, (3) ionospheric weather 3D model given by IRTAM, and (4) ionospheric weather model corrected to represent measurements of the ionospheric tilt by neighboring Digisondes.

4.1.2. TID-modulated realistic Ne model for HF-TID Verification

The TIDs associated with atmospheric gravity waves have typical periods of tens of minutes. These TIDs modulate the background ionization $N_0(x,y,z,t)$, and the resulting bottomside electron density distribution *Ne* can be represented as:

$$Ne(x,y,z,t) = N_0(x,y,z,t)\,(\,1 + \delta N\,)$$

where δN term represents the relative amplitude of perturbation of the background ionospheric profile due to the presence of TIDs. Conventionally, the perturbation term is represented as a sum of plane horizontal sinusoidal waves of various wave number K_i and amplitude a_i. However, a more realistic TID specification is done using the spherical geometry approach so as to support computations for radio paths above 1000 km more accurately. Full details of the spherical geometry definitions are beyond the scope of this document. Two alternative definitions of TID models are illustrated in Figure 39; both models are proven to produce nearly identical 3D density specifications and TID detection performance metrics.

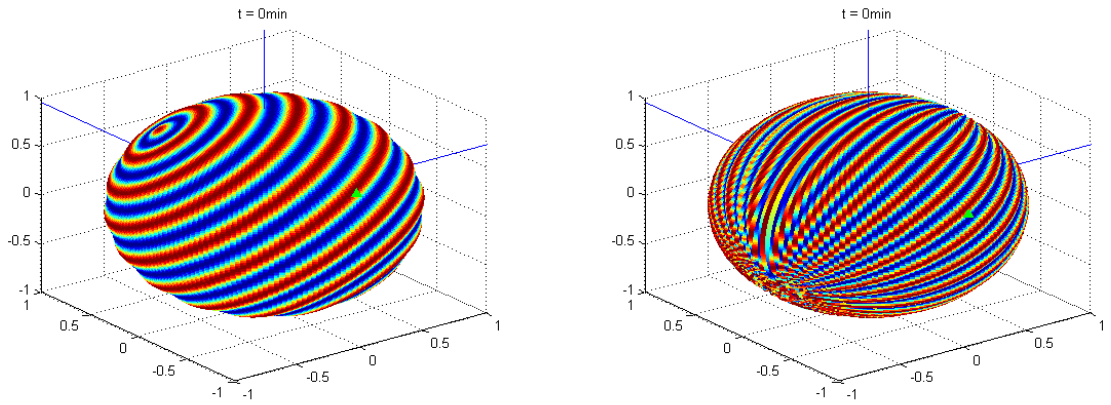

(a) (b)

Figure 39. Use of spherical geometry to define models of TID.
Same TID propagating at azimuth angle of 150° CW. (a) Model 1: Phase path is the great circle path between TID origin and observation point (green triangle). (b) Model 2: TID wavefront is perpendicular to the travel direction.

4.1.3. Ray tracing system for HF-TID Verification

Existing Huang-Reinisch raytracing algorithm based on the solution of the Haselegrove ray equation system that gives the relation of the ray path and the wave normal in spherical coordinates. Detailed description of the raytracing algorithm and underlying Haselgrove formalism can be found in [RD-5]. Huang-Reinisch algorithm has been amended with capability to identify the propagation mode as a function of the HF arrival angles and to limit the simulation study to the selected mode. Once the accurate ray trajectory in the ionosphere is computed, its parameters are obtained (arrival angles, time of flight, and Doppler shift as a time derivative of the phase path).

4.1.4. Verification Results

Example results of reconstructing TID parameters with FAS algorithm are shown in Figure 36. Overall the accuracy of TID parameter reconstruction is acceptable, being with 10% margin. The major source of errors in TID reconstruction is limitation of the TID model used in FAS algorithm and finite length and time sampling of the measurements (simulation). Given high computational demand of the signal synthesizer numerical code, verification of the HF-TID algorithms will continue over remaining time of the project.

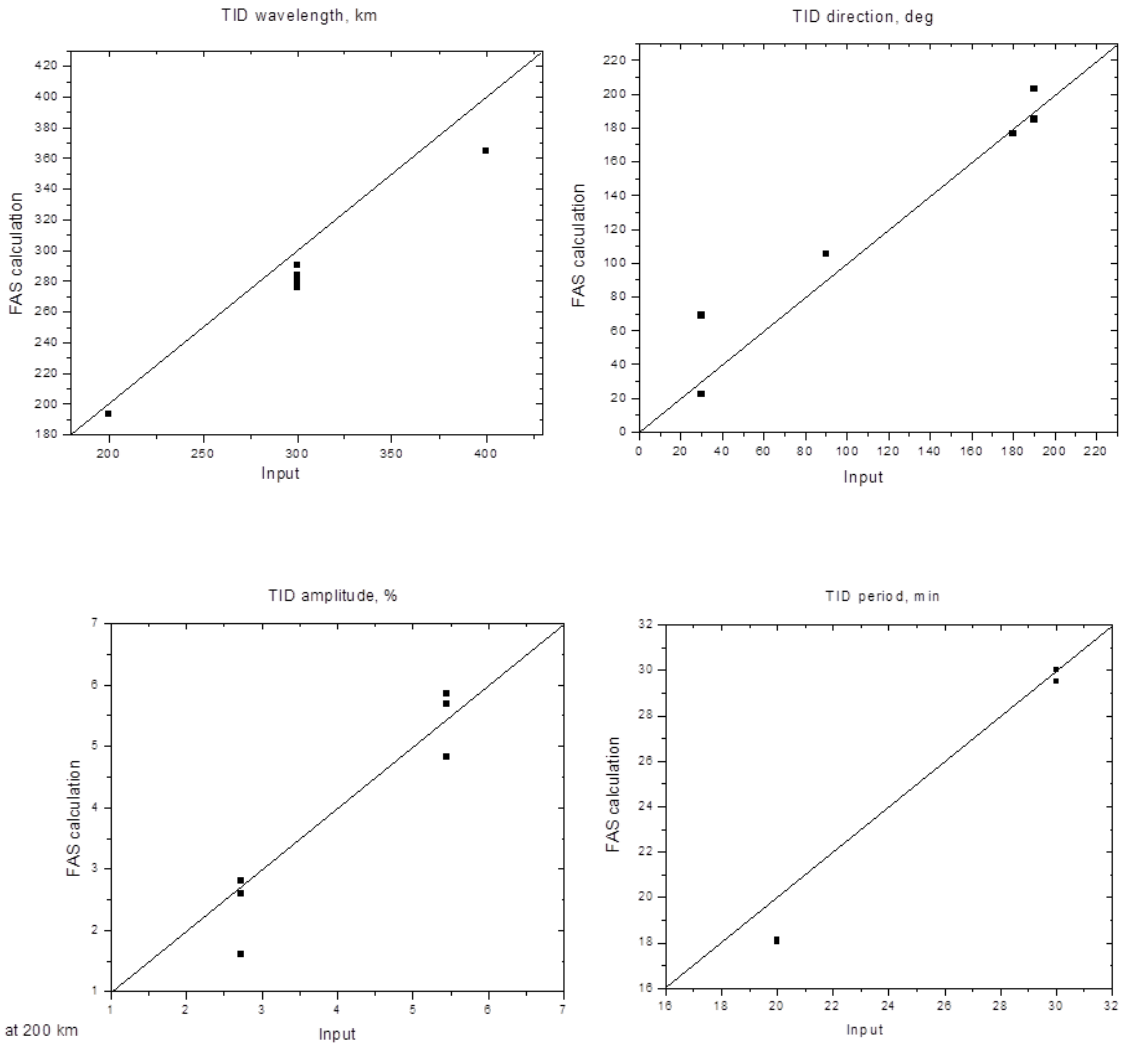

Figure 40. Verification of the HF TID algorithms using synthetic TID data (scatter plot). Accuracy of restoring the original TID parameters of the signal synthesizer is within 10%.

4.2 Verification of HF interferometry method

To verify the capability of HF interferometry method to detect TID events, we created a set of synthetic data using the following analytic function, that represents the propagation of a plane wave:

$$F = F_0\left(1 + Ae^{-(t-t_0)^2/b}cos\left(\underline{k}x - \omega t\right)\right) \qquad (4.2.1)$$

where F_0 is the background obtained from IRI model for MUF at different epochs of the year, the $cos(kx - \omega t)$ gives us the oscillation of the wave and its spatial propagation, vector $\underline{k} = \frac{\omega}{\underline{v}}$ gives us the propagation of the wave according a specific velocity and direction. Constants of the exponential term (A and b) allows us to control the amplitude and the duration of the perturbation respectively. The value of time t_0 is used to center the exponential around the desired time. Figure 41 shows the background calculated from IRI and the perturbation added according the different parameters of T, A, b and t_0 for EB040 in winter, but with the same velocity and azimuth (V=500m/s and Azi=180º).

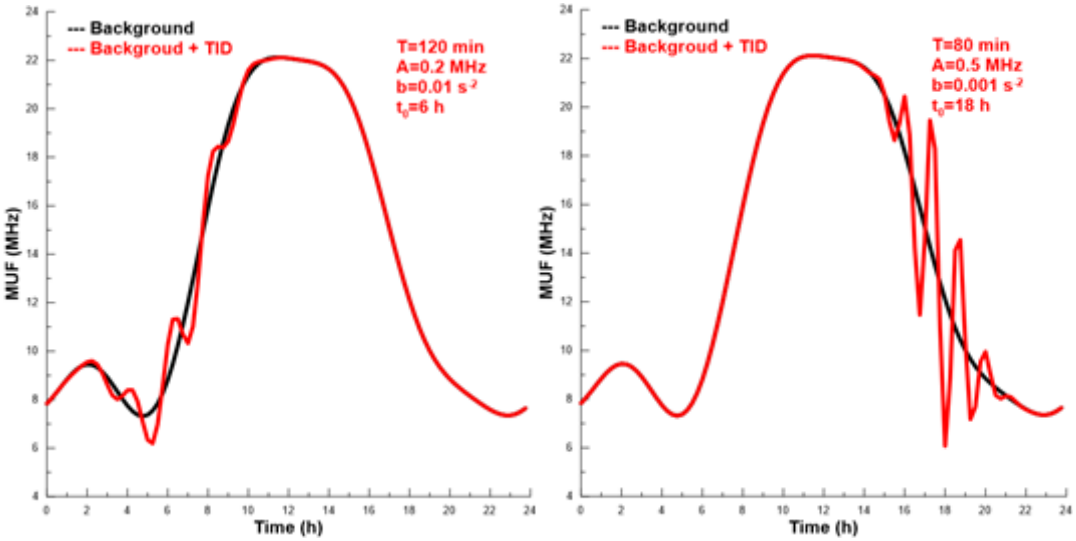

Figure 41. Examples of two TID generated analytically for the same station, EB040, and at same epoch, winter. Black lines correspond to the IRI predictions for the MUF above EB040 for 15 January 2017. Red lines correspond to the plane wave analytical function added to the IRI predictions for the same day. Different values of period (T), amplitud (A), duration of the disturbance (b) and centered time (t_0) are depicted in each plot.

Figure 41 shows the residual values for both cases depicted in figure 40 (see section 3.2.2.4 for information about the residual calculation). As we expected, the period is larger in the

left case and the amplitude is larger in the right case, according the parameters of the perturbation introduced.

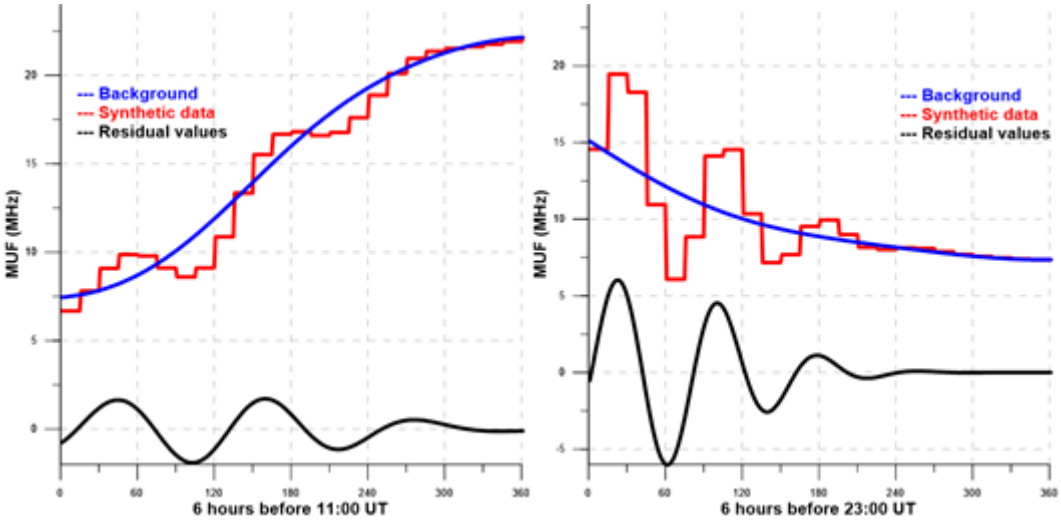

Figure 42. Results of the residual calculation from the examples shown in figure 17. Left plot corresponds to the residual calculation for a perturbation with T=120 min, A=0.2 MHz centered at 6h UT and right plot corresponds to the residual calculation for a perturbation with T=80 min, A= 0.5 MHz centered at 18h UT.

To simulate a "realistic" disturbance of auroral origin propagating southward we have taken an azimuth of 180º, a velocity of 500 m/s with T=120, A=0.2 MHz, b=0.01 s^{-2} and to=6h (left plots of figure 41 and 42). Figure 43 shows the residual values for each station for this particular case. The stations are sorted according the arrival of the simulated TID (on the top JR055 and on the bottom AT138) to see easily the time delay between the stations.

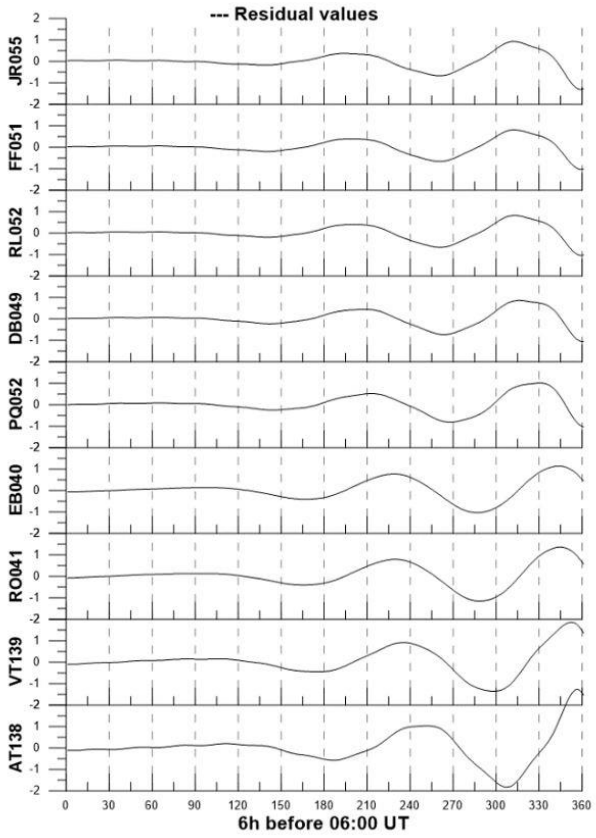

Figure 43. Residual values for each station calculated on basis a synthetic data simulating a TID with a velocity of 500m/s propagating southward, with period of 120 minutes, amplitude of 0.2 MHz centred at 6 h.

We have defined a data set of 24-hour with a sampling interval of 15 minutes for each station to be used as input to verify the HF interferometry method. Figure 44 shows the results for a simulated TID with a period of 120 minutes, velocity of 500 m/s and azimuth of 180º. As we can see, the results for period, velocity and azimuth fits very well to the expected values. Larger discrepancies are observed at the beginning and ending of the detection. Theses discrepancies are due to the fact that the window of analysis does not matches enough data to clearly detect a “periodic” variation which is optimally one cycle.

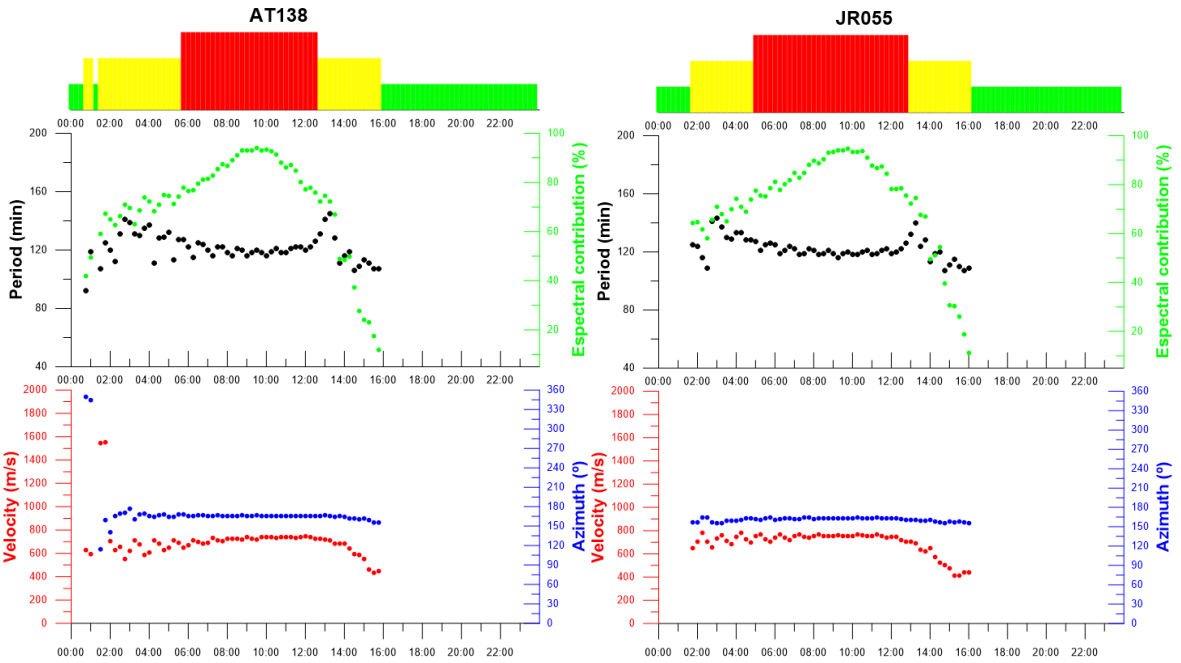

Figure 44. Results of the HF interferometry method for a synthetic TID with velocity 500 m/s and azimuth 180º for 2 different stations AT138, and JR055. From the bottom to the top, velocity and azimuth, period and espectral contribution and the warning "traffic lights".

Another example of the verification of the method is presented in figure 45. In this case we simulate two synthetic TID, the first centred at 06 UT with period of 120 minutes, velocity of 500 m/s and azimuth of 270º (simulating a TID linked to sunrise effect), the second TID centred at 21 UT with period of 80 minutes, velocity of 1000 m/s and azimuth of 180º (simulating a TID of auroral origin).

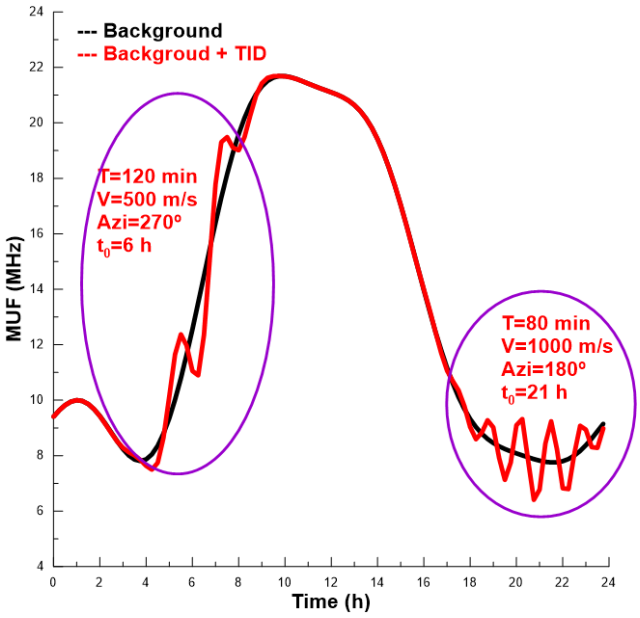

Figure 45. Example of 2 TIDs generated analytically on the same day for VT139 in winter. Black lines correspond to the IRI predictions for the MUF above VT139 for 15 January 2017. Red lines correspond to the plane wave analytical functions added to the IRI predictions for the same day. Different values of period (T), amplitude (A), duration of the disturbance (b) and centered time (t_0) are depicted in the plot.

Figure 46 shows the results after run the HF interferometry method to this synthetic data set. For all cases the method is able to reproduce the expected results.

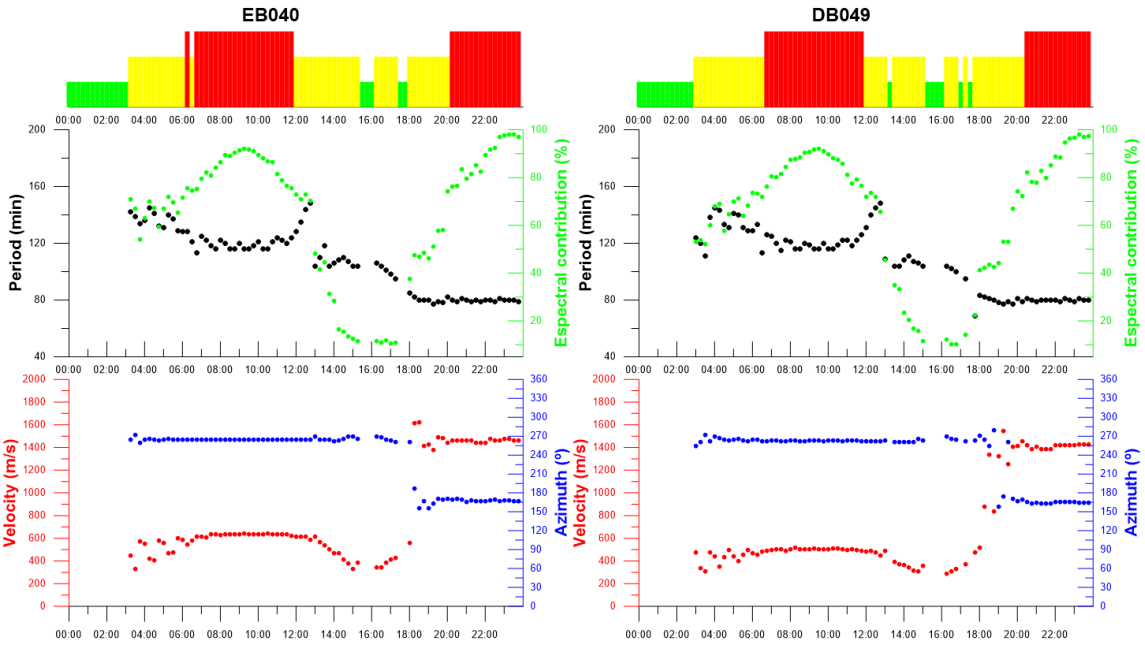

Figure 46. Results of the HF-method for two successive synthetic TID presented, for the indicated stations. The first TID is centred at 06 h with period of 120 minutes, velocity of 500 m/s and azimuth of 270º, and the second synthetic TID is centred at 21 h with period of 80 minutes, velocity of 1000 m/s and azimuth of 180º.

4.3 Verification of spatial and temporal GNSS analysis tools

4.3.1 Verification with actual data

4.3.1.1 MSTID detection

The verification of the MSTIDs detector it is planned to be done using the CATNET network during a whole Solar Cycle.

For the verification we will compare the NRTK solutions of single frequency users with the outputs of the MSTIDs detector.

4.3.1.2 MSTID propagation parameters

For verification purposes, the clearest MSTIDs are plotted in order to check the correctness of the propagation parameters. For instance, the next example corresponds to a MSTIDs detected with the MADR network during day 001 in 2018.

MSTID: 39300 9 madr

time: 39300

sat: 9

sta_ref: madr

amplitude: 0.028 (0.27 TECUs)

elevation: 74.6

name ipp_lon ipp_lat d_x d_y corr d_t T_mx-T_mn

ADD_STA: cebr -3.79 40.97 -9.75 2.70 1.00 -39.00 -393.00

ADD_STA: vill -3.40 40.96 24.61 1.36 .98 48.00 -405.00

STA_REF_ipp: madr -3.683 40.947

SCAN_velocity(km/s,deg): .051 46.490

SLOWNESS: 2.640321 -7.105491 .48E+00 .41E+01

RMS_residuals: .00E+00

PROP_velocity(km/s,deg): .132 159.615

SOL: 39300 9 madr 132. 160.

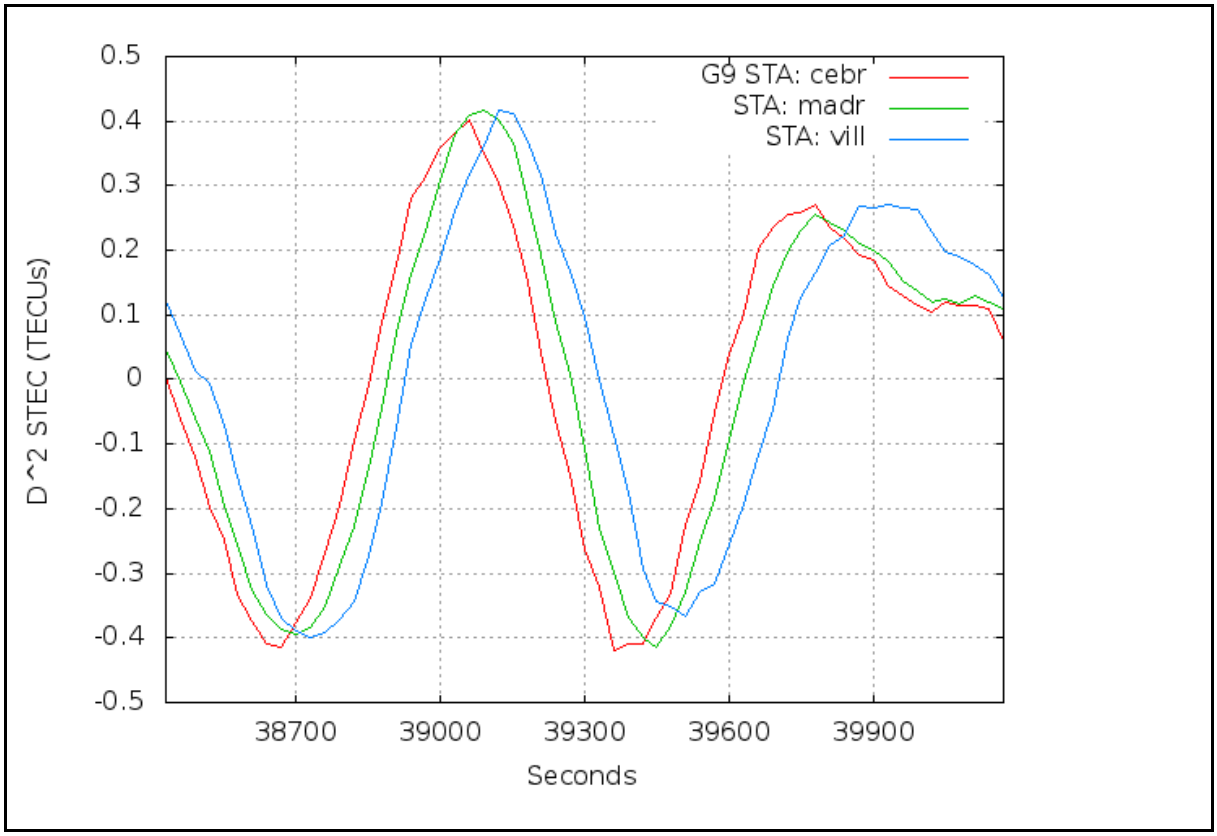

Figure 47. **Example of an actual MSTID affecting differently 3 receivers from the MADR network**

4.3.2 Verification with semi-synthetic data

The tool for estimating propagation parameters has been verified using semi-synthetic data. These data have been generated using actual data from the MADR network during the day 197 in 2018. The STEC measurements of these actual data have been substituted by the prediction from the IGS GIMS for this day (because the low resolutions of IGS GIMs. it is expected that MSTID signatures will be not present in the predictions). Finally a sinusoidal perturbation with an amplitude of 0.1 TECU and a period of 1000 and with variable velocities and azimuths has been generated and added to the GIMs predictions.

The MSTID velocities range from 50 to 350 m/s with a step of 50 m/s.

The MSTID azimuths range from 0 to 330 degrees with a step of 30 degrees.

Figure 47 depicts an example corresponding to a MSTID simulated with an azimuth of 210 degrees and a velocity of 50 m/s. One can see that, in spite of the simulated period is of 1000s and due to the IPP movement, the apparent period is clearly smaller

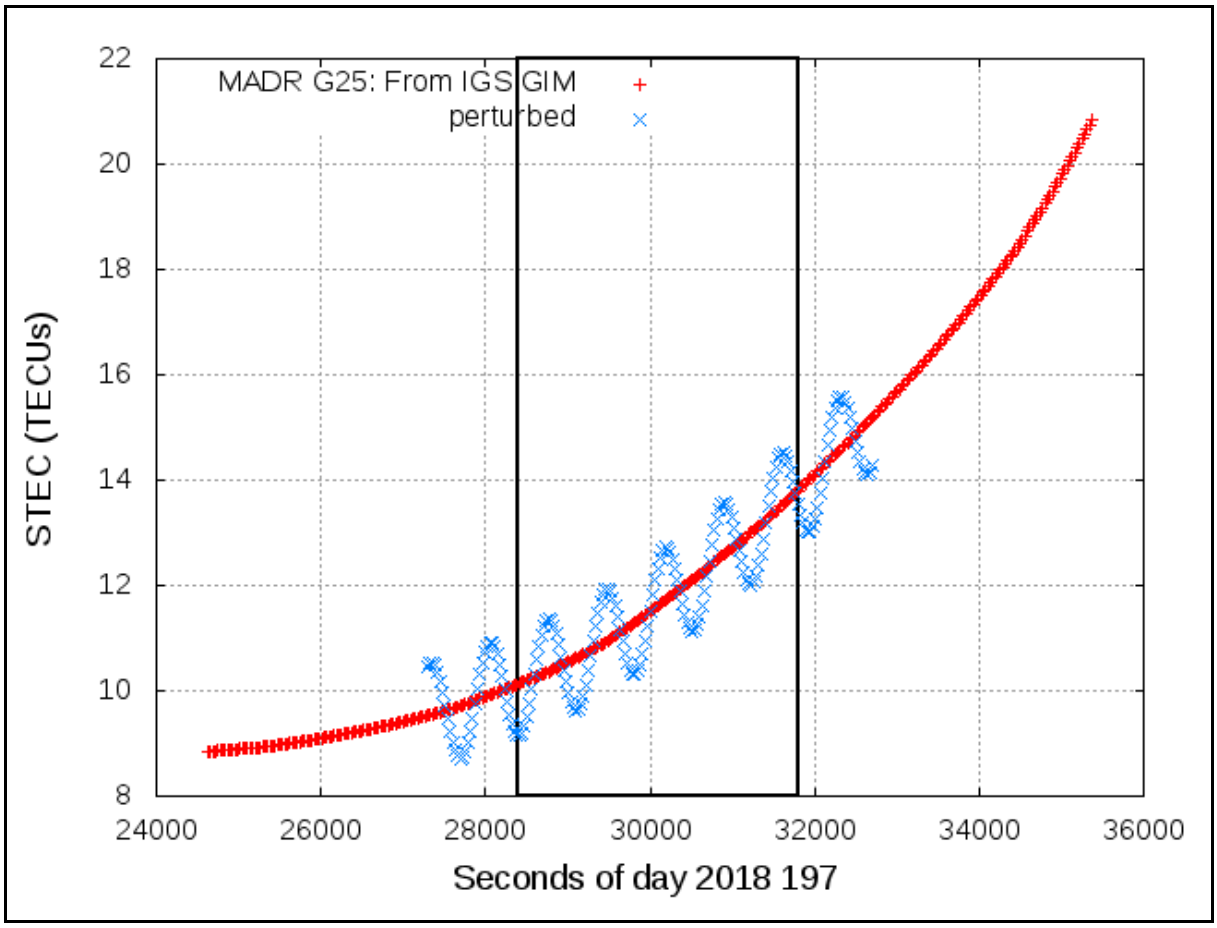

Figure 48. Example of a simulation corresponding to the receiver MADR and the G25 satellite. Red color represents the STEC values from the IGS GIMs. The blue points are the perturbed STECs after the MSTID simulation.The box indicates the analysed period

4.3.2.1 Estimation of the propagation parameters.

In what follows we present the results for the satellite G25 at UT 30000s, the elevation of this satellite at this time is 61 degrees. In the plots we depict the difference between the simulated and estimated parameters.

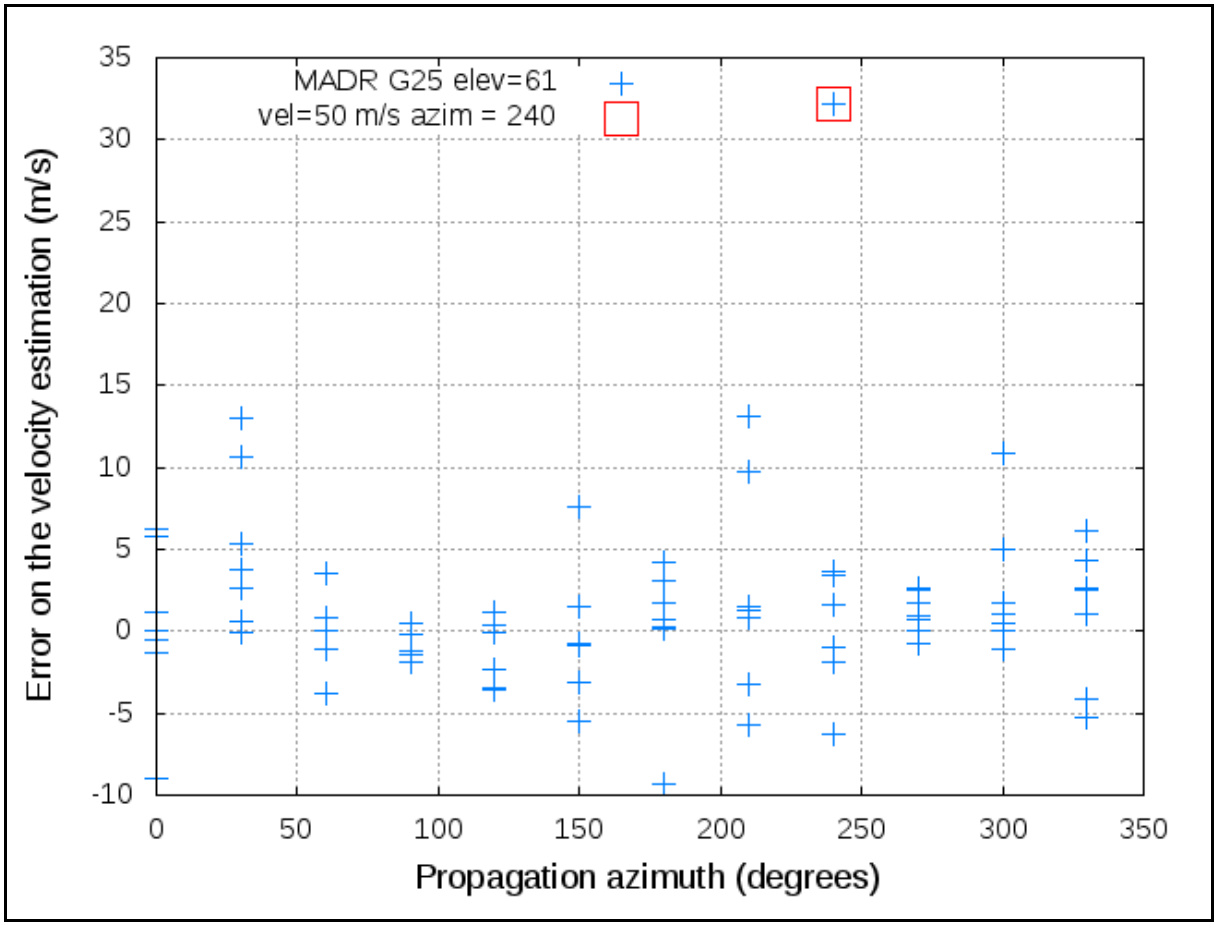

Figure 49. Error of the velocity estimation as a function of the MSTID direction

As can be seen from Figure 49, the error on the velocity estimation is typically below 10 m/s. There is only one anomalous case that correspond to a MSTID with 50 m/s and an azimuth of 240 degrees. These small velocities can be even smaller than the scan velocities (the apparent movement of the IPP) and can produce very small apparent periods due to the combination of the IPP movement and the MSTID. In these cases, with such small periods and in spite of the small baselines, it can appear ambiguities in the estimation of the delays that can be wrong by a period.

One can prevent against these cases because they present small apparent periods (pseudo periods) as can be seen in Figure 50. Indeed, the apparent periods are clearly smaller than the simulated ones (1000s) and some of them are below the expected period for a TID.

Finally, from Figure 51 one can see that, except for the anomalous case above mentioned, the error on the estimation of the azimuth is of only few degrees.

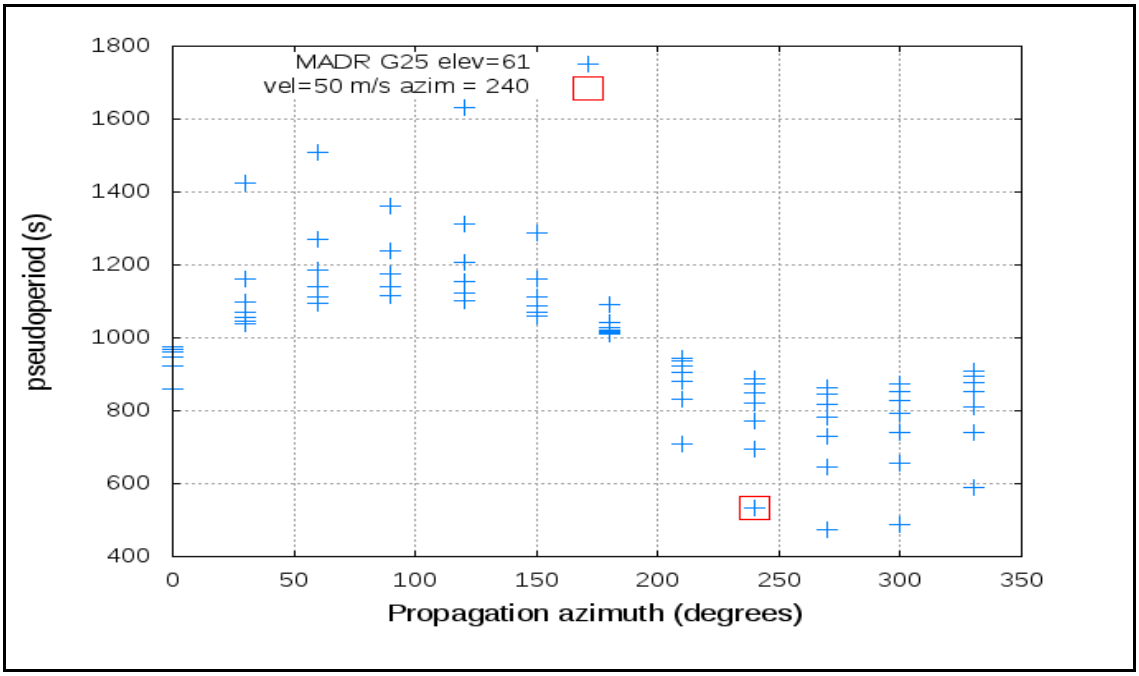

Figure 50. **Estimated apparent period as a function of the MSTID direction**

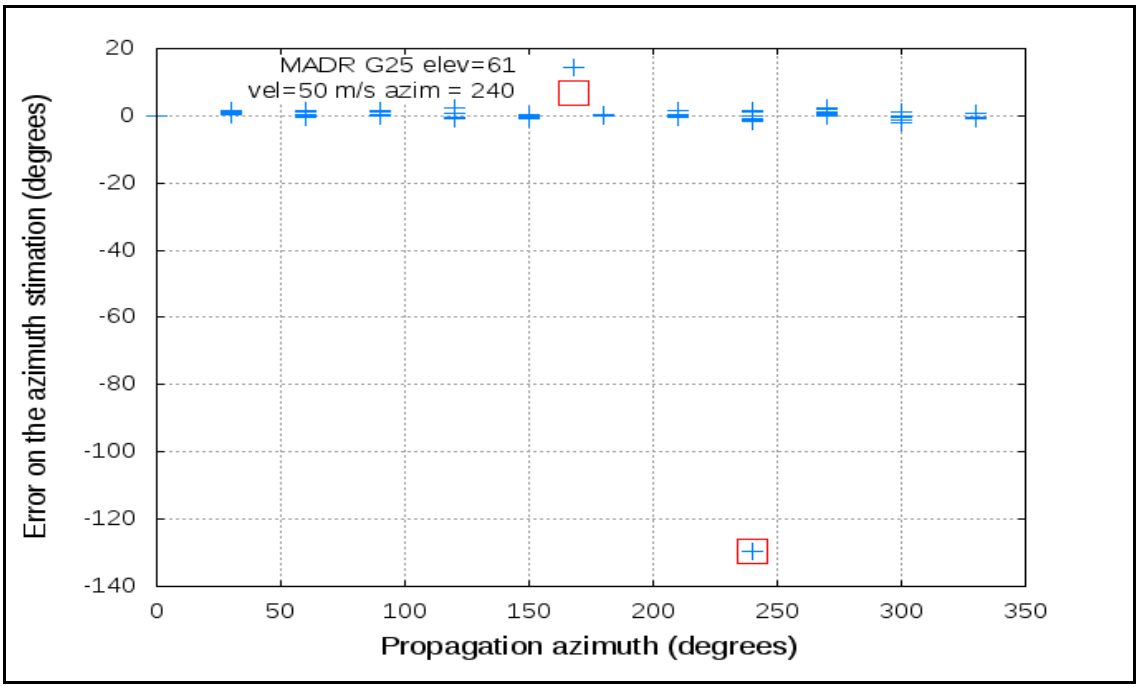

Figure 51. Error on the azimuth estimation as a function of the MSTID direction

4.4 Verification of TEC Gradient algorithms

The validation of TEC maps have been implemented in case studies which were performed against published event description.

In [RD-18] Mayer et al. (2008) detected extreme ionospheric gradients during the 20 November 2003 storm near Iceland. They estimated the speed with 117 m/s in North-South direction. The maximum gradients are observed short before 11 UT at latitude 63° North. These gradients are well reproduced in the TechTIDE product. Figure 52 clearly shows strong spatial TEC gradients and significant TEC decrease at 11 UT at 63 °N.

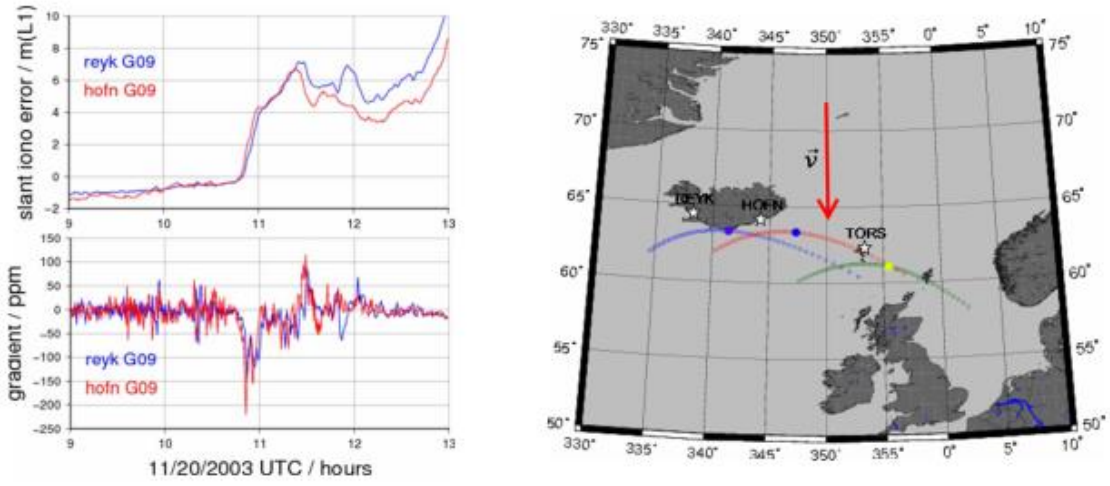

Figure 52. Ionospheric gradients during the 20 November 2003 storm near Iceland. Strong spatial TEC gradients and significant TEC decrease are detected at 11 UT at 63 °N

The Figure 53 demonstrates how these gradients are well reproduced by the TEC gradient method. It shows strong TEC gradients in the region between 60 and 70° N at 11 UT. Furthermore, it has been reported in Borries et al. (2017) that this gradient is located in the source region of LSTIDs. This shows well the validity of the TEC gradients method. However, it has to be noticed, that the TEC gradient method suffers from mapping and smoothing during the generation of the TEC maps. Therefore, the gradients are not as sharp and as steep as indicated in [RD-18].

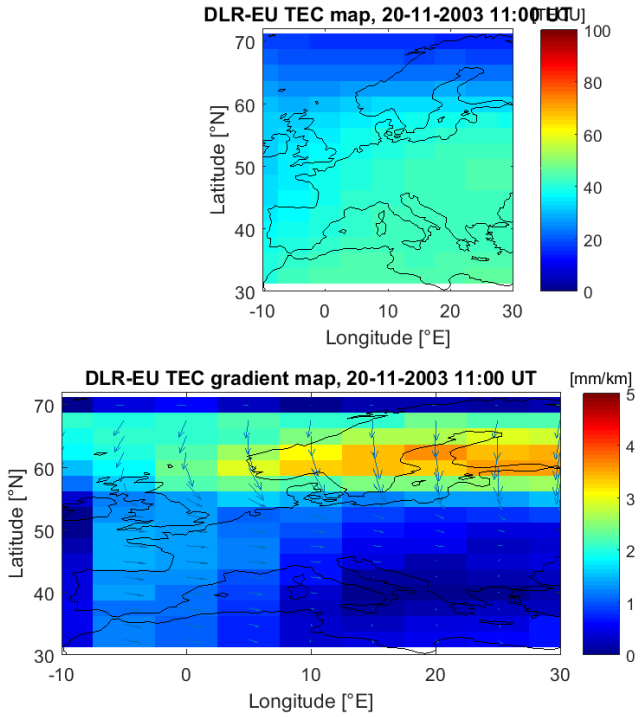

Figure 53. TEC gradients during the 20 November 2003 storm reproduced by the TEC gradient TechTIDE method.

The source region and excitation of LSTIDs has also been analysed in [RD-9]. The capability of the TEC gradient method to indicate is demonstrated in Figure 54. It shows that spatial and temporal TEC gradient occur in the source region of LSTIDs. This indicate the capability of TEC gradients to indicate the excitation of LSTIDs.

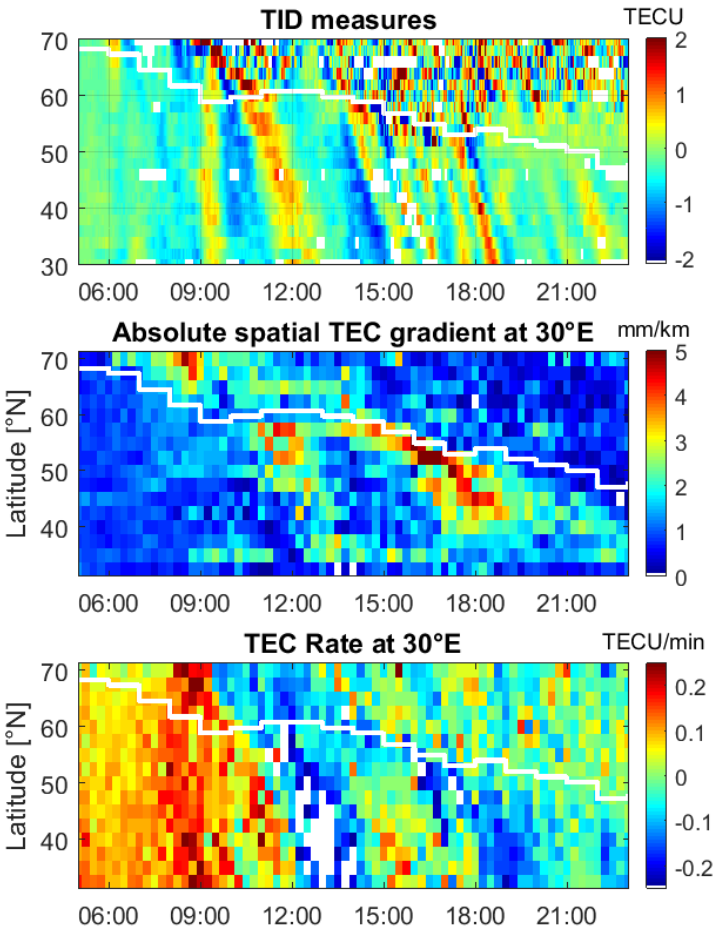

Figure 54. The capability of the TEC gradient TechTIDE method to indicate the source region of TIDs is shown for the 20 November 2003 storm

4.5 Verification of the TaD based EDD algorithms

4.5.1 The 1D version

As a first test of the performance of the new profiler, we compared TaD electron density profiles with actual measurements obtained from ISIS-1 satellite. This is not an independent evaluation test as ISIS-1 profiles were used for the development of the new method, but provides with evidence of how well the new profiler reproduces the input measurements. The comparisons are made through the estimation of the RMSE over whole profile, according to the following formula:

$$RMSE = \frac{1}{np}\left\{\sum_{h_{max}}^{h_{min}} [n_{TaD}(h) - n_{ISIS1}(h)]^{2}\right\}^{1/2}$$

where *np* indicates the number of points in each ISIS1 EDP, h_{min} and h_{max} are the lowest and highest altitudes for which ISIS1 electron density measurements are provided for a given profile, n_{TAD} and n_{ISIS1} are the electron density values at a given height *h*, provided by the TAD model and ISIS1 satellite respectively.

A very successful fit between measurements and model predictions indicating a very good agreement can be seen between the TEC parameters estimated by the ISIS1 profiles and those provided by the TaD model (Figure 55).

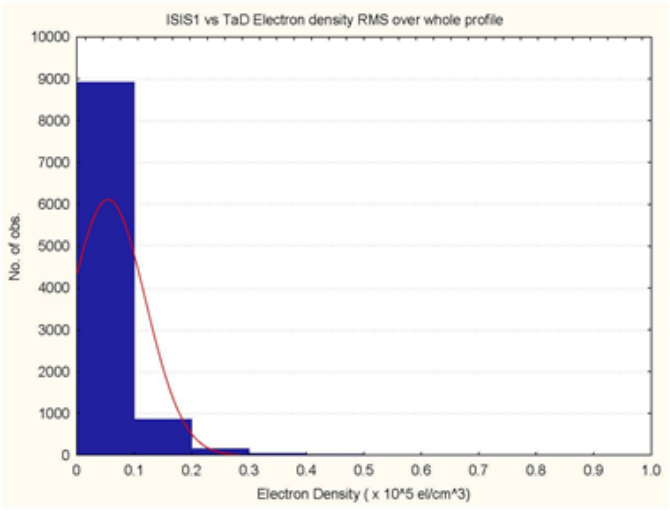

Figure 55. The histogram of distribution of RMSE between ISIS1 measured electron density and TaD output values.

The level of agreement between modelled and measured partial TEC parameters is estimated from the results of cross correlation analysis. First, we compare the plasmaspheric TEC, which is calculated integrating the electron density from the transition height up to the maximum height of the ISIS1 satellite. A very high correlation coefficient of 98.2% is estimated between the measured and the modelled parameters. Similarly, we calculated the topside TEC parameter, calculated integrating the electron density from the lower height of the ISIS1 satellite (slightly above hmF2) up to the transition height. Here the correlation coefficient, between observed and modelled quantities, is also impressively high reaching the 99%.

The second test is the comparison of the model profiles with measured profiles obtained from Malvern ISR. This test provides information for the model's performance in the altitude zone 200-600 km (approximately). The importance of this test is threefold: i) ISR profiles are the only source of full electron density observation from the ground, ii) they consist a totally independent source of information and iii) this comparison is strongly suggested by US National Space Weather Program and recent studies for the establishment of the top high priority metric for the ionosphere-thermosphere domain. For this purpose, a data set of some of 4000 electron density profiles obtained at Malvern ISR site (52.1 ˚N, 2.3 ˚E) during the time interval 1968-1971 were analyzed. After quality check almost the 30% of profiles have been eliminated from our sample. The F layer peak density NmF2 and height hmF2 were extracted from each individual profile. However, for the scaling of the ISR EDPs we have applied the method used in the topside sounder profiles scaling, i.e. the NmF2 and hmF2 parameters have been located in each measured profile; then its topside scale height H_{TM} has been obtained as a regression line from a number of data points above the peak, with the transition height h_{TM} being approximated as the height where O^+ is one half of the measured density. The four quantities taken from the measured profile have been ingested to the formula (2) and the model profile was calculated for altitude range of the topside part of measured profile.

Malvern-ISR profiles cover the altitude range up to approx. 700 km which is about the altitude of the actual transition height, so it is expected that O^+ will dominates and the observed Ne profile will follow closely the TaD profile of the O^+ density. Based on this, we compared the model predictions for O^+ distribution in respect to the measured profiles. The results are expressed in terms of the normalized RMSE estimates that where obtained over the topside profiles (from hmF2 up to the maximum height of the observed profiles). Their distribution is presented in Figure 56.

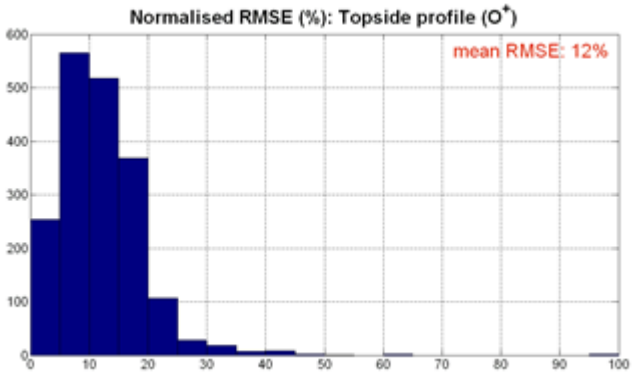

Figure 56. The normalized RMSE distribution of model predictions for O^+ in respect to the measured profiles.

As TEC is the most critical parameter for the reliable performance of several applications, we also performed comparison tests between TEC estimates obtained from modeled and observed EDP from the ISR at Malvern site concentrating in the topside part of the profile.

First, we present in Figure 57 the scatter plot of TEC modeled versus TEC observed estimates. The results indicate that the two parameters correlate reasonably well. A larger scatter is seen in the daytime hours (the area with larger TEC values), which is probably due to the high altitude of the transition height, something that makes its accurate determination problematic due to the lack of observations above 700 km. The O^+ /H^+ transition height varies but seldom drops below 500 km at night or 800 km in the daytime, although it may lie as high as 1100 km, depending on the geophysical conditions, and particularly on solar activity [RD-20].

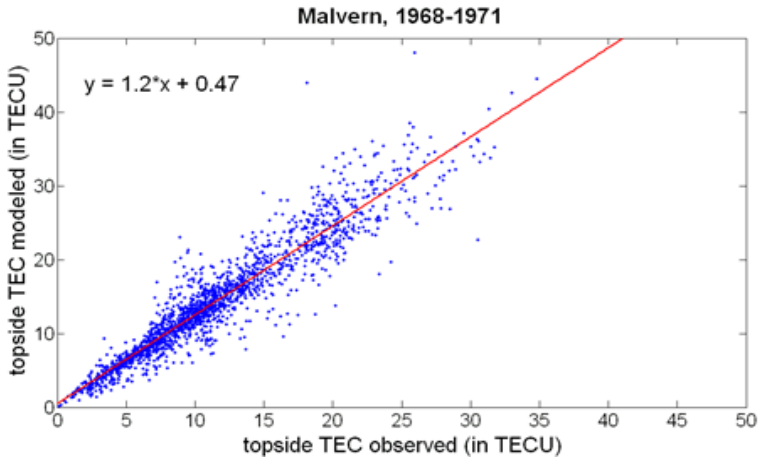

Figure 57. The scatter plot of TEC modeled versus TEC observed estimates

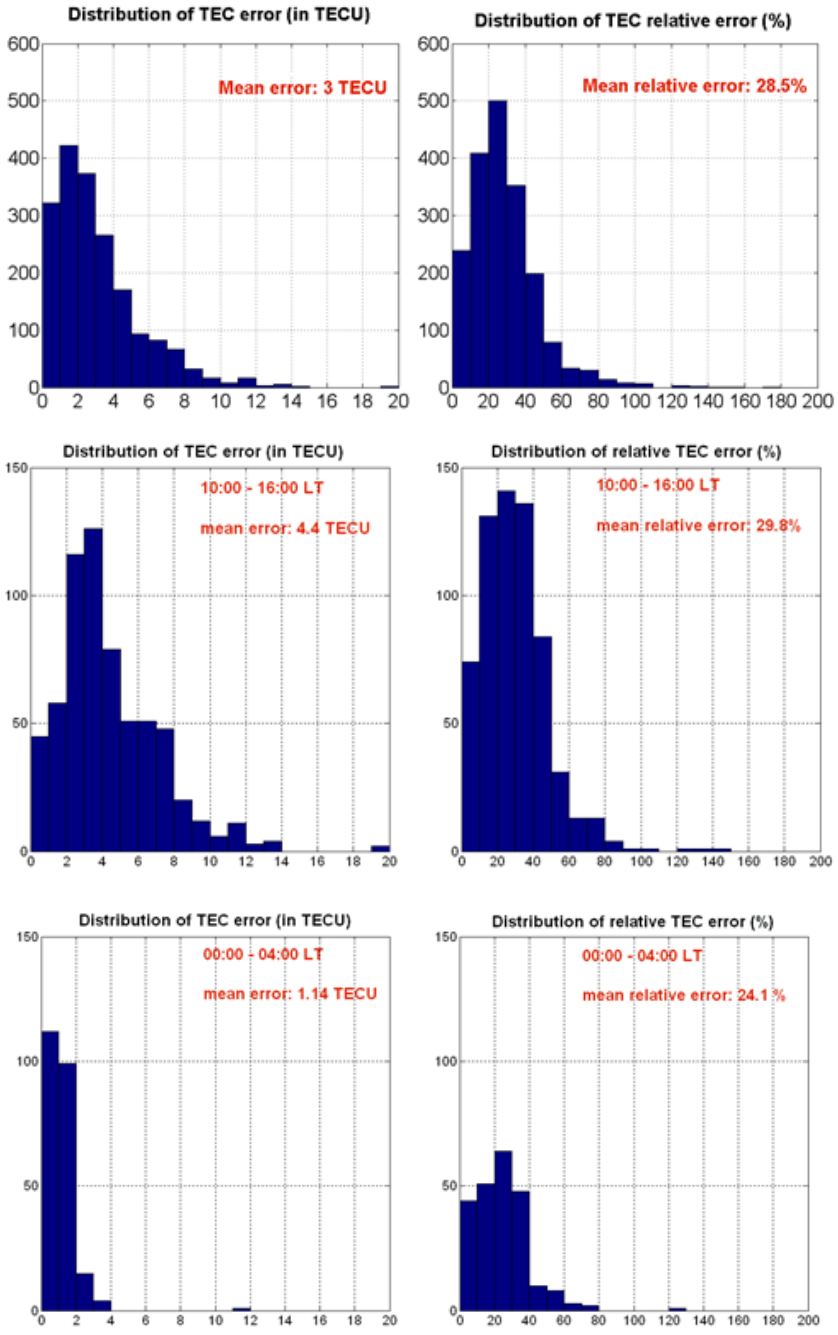

Figure 58. Distribution of the TEC error (abs(TECobs-TECmod)) and of the relative TEC error. From the top to bottom: (a) results based on all EDP; (b) results for to daytime EDP; (c) results for nighttime EDP.

In Figure 58 we present the TEC error (abs(TECobs-TECmod)) distribution and the relative TEC error distribution. From the top to the bottom we present the results based on all available measurement, in the middle we present the corresponding distribution diagrams for a subset of measurements that correspond to daytime EDP and in the bottom we give the distribution diagrams for nighttime cases. The analysis on the whole sample of measurements gives a mean error of 3TECU and mean relative error of 28.5%. However, this error reduces considerably when we include only the nighttime cases. This is an additional evidence showing that during daytime, when the transition height is in its upper limits, or even higher of 700 km, there are not enough data for the TaD to estimate correctly the transition height and this yields to artificial results.

4.5.2 The 3D version

To assess the accuracy of the 3D EDD distribution reconstructed with the TaD profiler, we have compared them with the slant TEC (sTEC) and vertical TEC (vTEC) values calculated from Receiver Independent Exchange Format (RINEX) files collected from the GPS stations listed in Table 10, on 8 March 2012 between 13:00 UT and 14:00 UT. To estimate the slant and vertical total electron content from GPS data we have followed the single station solution. Dual-frequency carrier-phase and code-delay GPS observations are combined to obtain ionospheric observables related to the slant total electron content (sTEC) along the satellite-receiver line-of-sight (LoS). Only datafiles received from GPS satellites with elevation larger than 70 degrees are considered in this analysis.

The EDD distribution along a particular raypath is obtained by calculating ED values at successive points along the trajectory. At each such point, the 5 TaD parameters are obtained by linear interpolation of their respective values at the nearest grid nodes and then ED is calculated for respective altitude by TaD formula (see Table 10). The integral of calculated ED along the given raypath is then compared with the measured sTEC. The difference between the calculated integral of ED along the raypath and the measured sTEC depends mainly on the shape of TaD profile (its values at different altitudes).

Table 10. **GNSS receiving stations which data is selected for error assessment**

Code	GNSS receiving station	Latitude, deg.	Longitude, deg.
NOA1	Athens, Greece	38.0	23.8
AQUI	L'Aquila, Italy	42.3	13.5
EBRE	Ebre, Spain	40.8	0.5

HERS	Hailsham, UK	50.8	0.3
HERT	Hailsham, UK	50.8	0.3
WARN	Rostock-Warnemuende, Germany	54.2	12.1
SASS	Sassnitz Island-Ruegen, Germany	54.5	13.6

To assess the TaD model performance, the error relative to the data deviation between the model and measured values is used, obtained separately for vTEC and for sTEC. The database consists of 6780 values of vTEC and sTEC pairs measured by the receiving stations listed in Table 10. TaD profiles are calculated for each data pair respectively. Figure 59 shows the relative deviations rel vTEC (red dots) and rel sTEC (blue dots) versus latitude (top panel), azimuth (middle panel) and elevation (bottom panel). The red and blue portion of the vertical bars in the top panel represents the relative deviations for each receiving station in the database. It is seen that middle and bottom plots consist of pieces of dotted curves representing the individual passes of GPS satellites over the selected stations. The red and blue portion of the vertical bars in the top panel represents the relative deviation for each receiving station in the database. The limited statistics reveal that the model error does not depend on azimuth and elevation of the signal raypaths. As expected, the model error of sTEC is larger than that of vTEC, due to fact that the slant raypath passes over larger territory, where the maps of TaD parameters may contain larger errors.

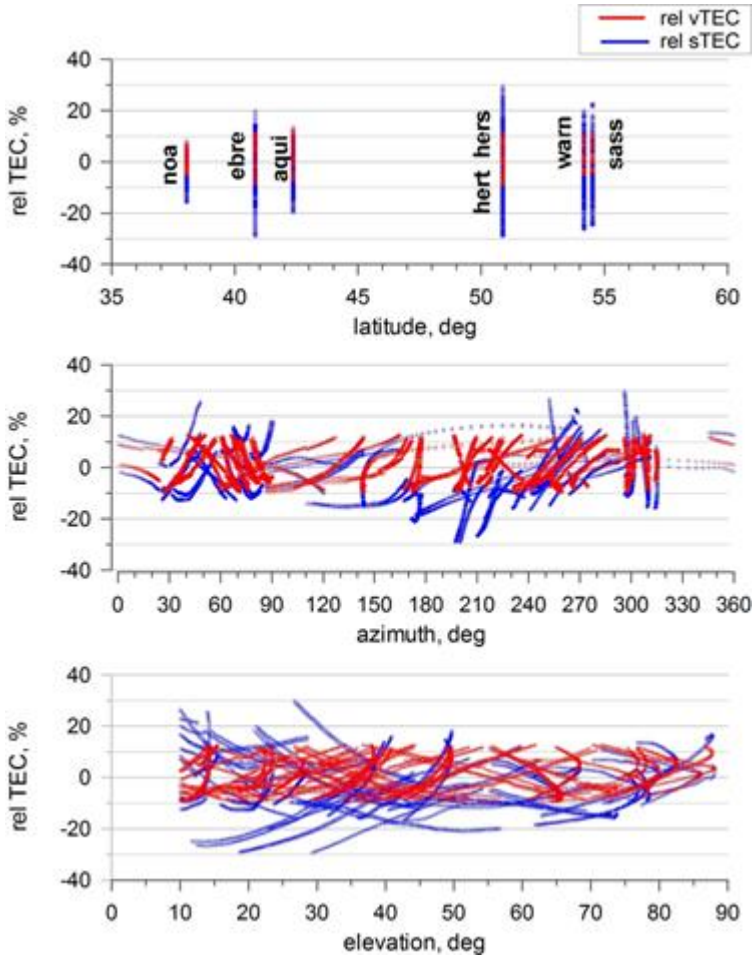

Figure 59. Relative deviation of model from measured sTEC (blue dots) and vTEC (red dots) versus latitude (top panel), azimuth (middle panel) and elevation (bottom panel).

Figure 60 shows histograms of rel vTEC and rel sTEC for all selected data points. The relative deviations are given in percent from the measured values. The sTEC distribution (filled cyan bars) are close to the normal distribution (the purple curve) which shows a standard deviation of 10 % and offset toward negative deviations of about 3%. The distribution of rel vTEC exhibits a double peak shape, probably an effect of the limited number of data, but the equivalent normal distribution shows an offset of only 0.77% and a standard deviation of 6.0%. The error assessment shows an excellent agreement between model and data which demonstrates the high accuracy of the 3D EDD model distribution.

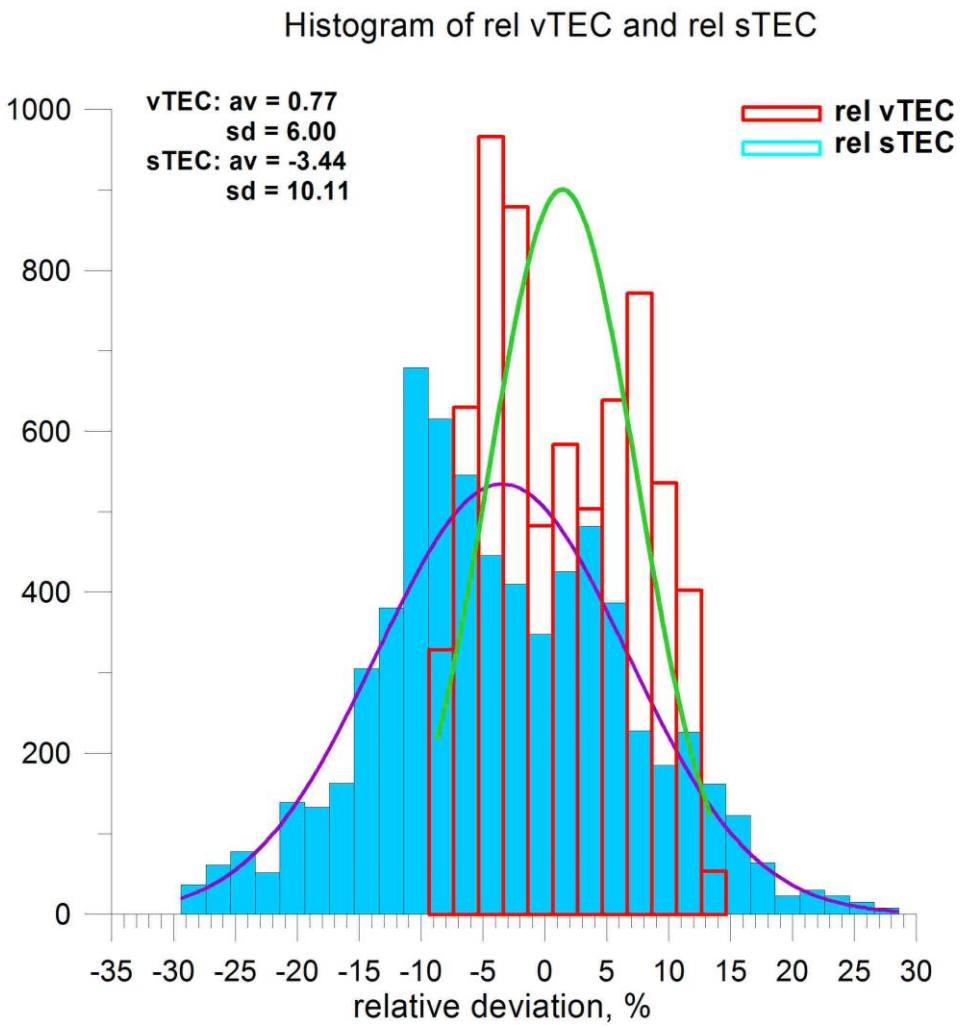

Figure 60. Histogram of relative deviations of model-from-measured sTEC (light blue) and vTEC (unfilled red).
The purple curve represents the normal distribution of rel sTEC data, and the dark green curve shows the corresponding normal distribution of rel vTEC.

The model errors of this multi-parameter fitting to the different source of data, as those of Digisonde sounding and GNSS-TEC maps, look surprisingly small. The explanation is that TaD profiles are calibrated in advance to the TEC values from the ROB maps and those profiles are then compared with vTEC values from EUREF database. The use, by necessity, of two TEC database, one for adjusting (ROB database) and another for comparing (EUREF database) is not a requirement of the 3D reconstruction procedure The use of one and the same database

would even decrease the total model error which is now evaluated. Two error sources contribute mainly to the total error: the mapping of TaD (H_T, h_T, and Hp, foF2 and hmF2) parameters in the mapping area and the theoretical shape of TaD profiles. The mapping procedure could introduce large errors in the areas of the map with no data, while the statistically defined analytical expressions of the vertical TaD profile could differ significantly from that in any particular condition. While these error sources cannot be separately evaluated, their total effect on the model error is well assessed. Fortunately, the total error is quite small, which is a clear evidence of the reasonable accuracy of the 3D EDD reconstruction.

It has to be noted that the chosen time of 8 March 2012 is in the initial phase of an intense substorm, after a sudden storm commencement (SSC) at 11:00 UT accompanied by an abrupt increase of the solar wind pressure [RD-28]. The geomagnetic conditions are favorable for LSTID occurrence. The increase in the electron density calculated by the model for the specific vertical direction in the 3D space for altitude above 800 km can be potentially considered as an evidence for the sensitivity of the model in TID generated perturbations. It should be noted that during this epoch, a marked increase of foF2 and hmF2 is seen between 40° and 55° latitude and 5° to 20° longitude, although TEC does not show a proportional increase.

4.5.3 Tracking the altitude of LSTIDs with the EDD methodology

The 3D EDD code has been used to calculate the electron density distribution for the period 16 April to 26 April 2017, using the following settings:

Location: Athens (Longitude 23.5 E, Latitude 38.0 N)

Digisonde data: Athens Digisonde in 5 min operation mode for the vertical ionograms

GNSS data: Athens GNSS station (Longitude 23.8 E, Latitude 38.0 N)

TEC solution: Provided by UPC

The input parameter to the EDD code are

(Year, Month, Day, Hour, Minutes) -- Date and UTime

Lat -- Latitude

Long -- Longitude

foF2 – cut off frequency in [MHz]

hmF2 – height of maximum electron density in [km]

TEC – GNSS Vertical TEC in [TECU]

bTEC – Digisonde Bottomside TEC in [TECU]

HsD – Digisonde Bottom Scale Height in [km]

The EDD code retrieves the input parameters and delivers the electron density at any altitude from 90 km to 20,000 km. In Figure 61, we present on the left-hand side the input parameters for the day 21 April 2017 and the calculated electron densities for preselected altitudes starting from 150 km to 500 km at 50 km step. On the right-hand side, we present the de-trended electron densities using as a background the 1 hr running average. At the bottom panel we present the height of the occurrence of the maximum perturbation h(Ne_{max}).

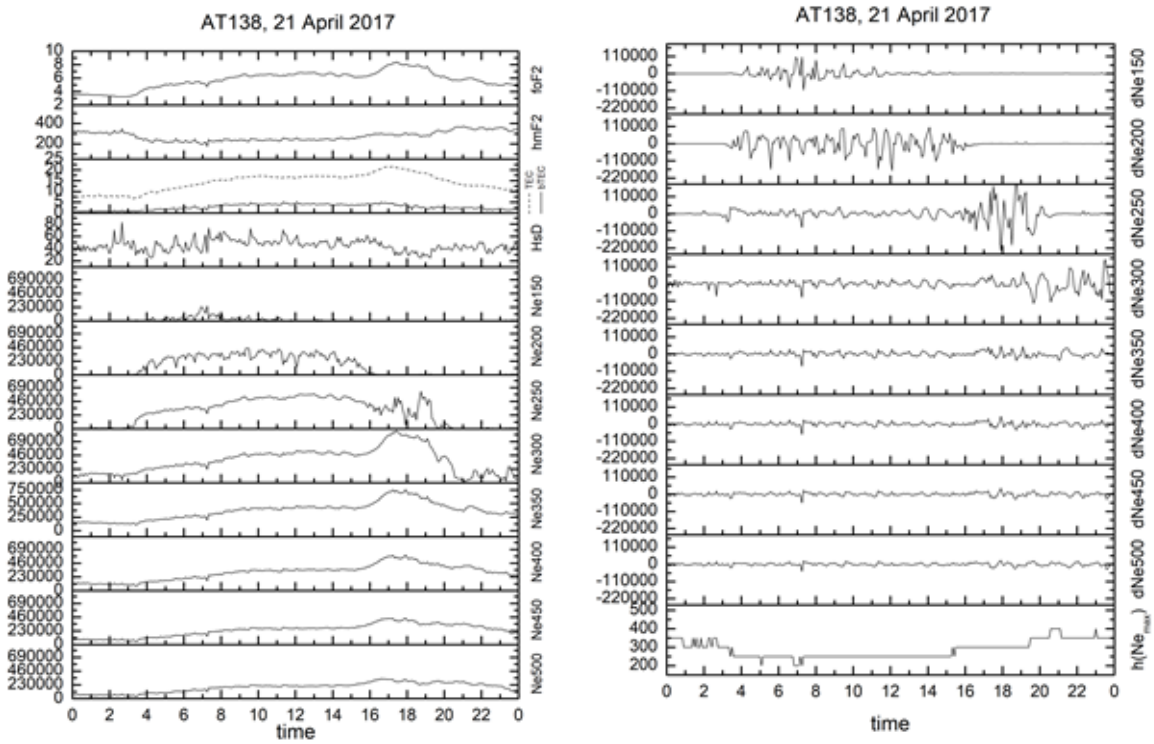

Figure 61. To the left: The input and output parameters for the day 21 April 2017 (see the text for more details. To the right : The de-trended electron densities using as a background the 1 hr running average. The height of the occurrence of the maximum perturbation h(Ne_{max}) is given at the bottom panel.

During this day we observe significant variations in all the layers of the ionosphere. The detrended values on the right-hand side show a perturbation probably due to travelling ionospheric disturbances which starts at the lower altitudes (around 150 km) and shifts progressively to a height of 300 km during the evening sector. This shift coincides with an

abrupt increase in TEC (see the corresponding plot in the left-hand panel). The height of the TID occurrence h(Ne_{max}) varies significantly from approx. 300 – 400 km in the nightside ionosphere down to 250 km in the dayside ionosphere, following the variation of the F-layer altitude, showing that the LSTIDs occur most frequently in the F-layer.

4.6 Verification of HTI method

To verify the capability of the HTI method to detect TID events, we have to use raw data since there is no capability to produce synthetic ionograms. We concentrate on two days one of which (10 April 2017) does not exhibit any TID activity and one day (April 21 2017) where TID activity was registered. The corresponding HTI intervals of interest around the time of the TID event are indicated in the HTI plots provided in Figure 62:

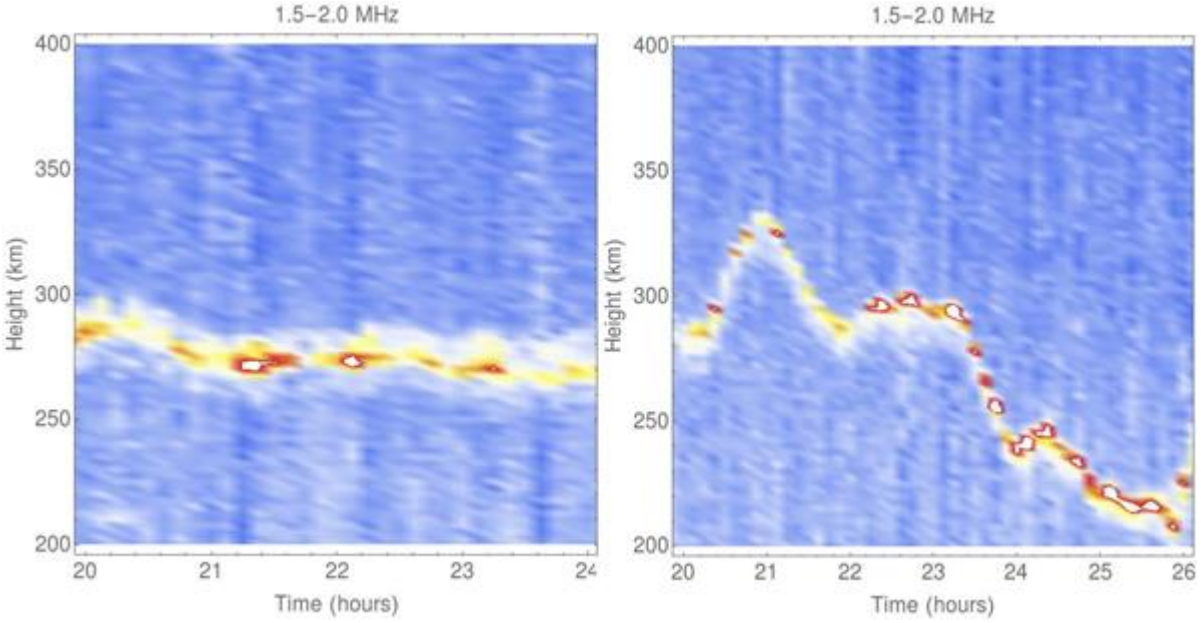

Figure 62. HTI density plots for 10/04/2017 (left) and 21/04/2017 (right).

We subsequently carry out the analysis of detecting relevant TID periodicity as described in section 3.6.1.1.

An example of our analysis is given in Figure 63 for the points of maximum intensity extracted from the data of Figure 62. In the range between 1 and 3 hours a well-defined and narrow distribution is obtained for the 21st of April, in contrast to the 10th of April. This signifies that with high probability our signal on the 21st can be described by an LSTID on top of which some

arbitrary background activity exists. In Figure 64 we plot the fit function after the parameters were determined and compare this with the points of maximum intensity.

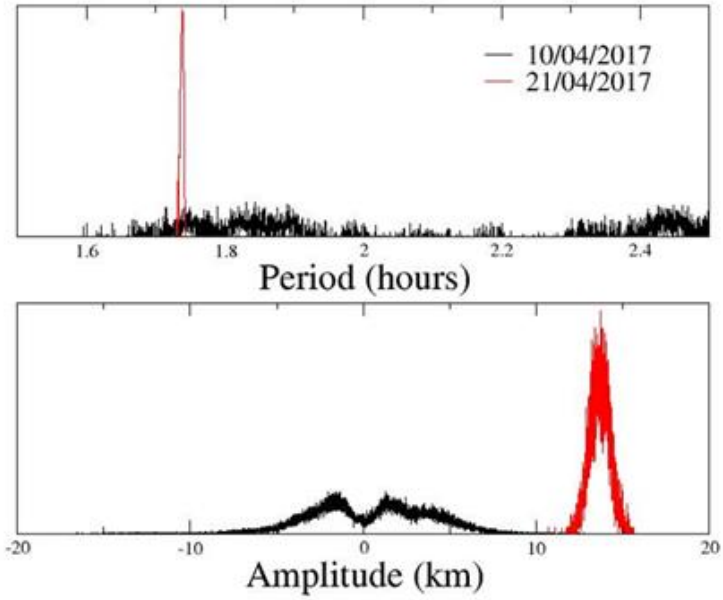

Figure 63. The probability distribution function for the lowest periodicity (top) and the equivalent amplitude (bottom) as sampled using AMIAS.

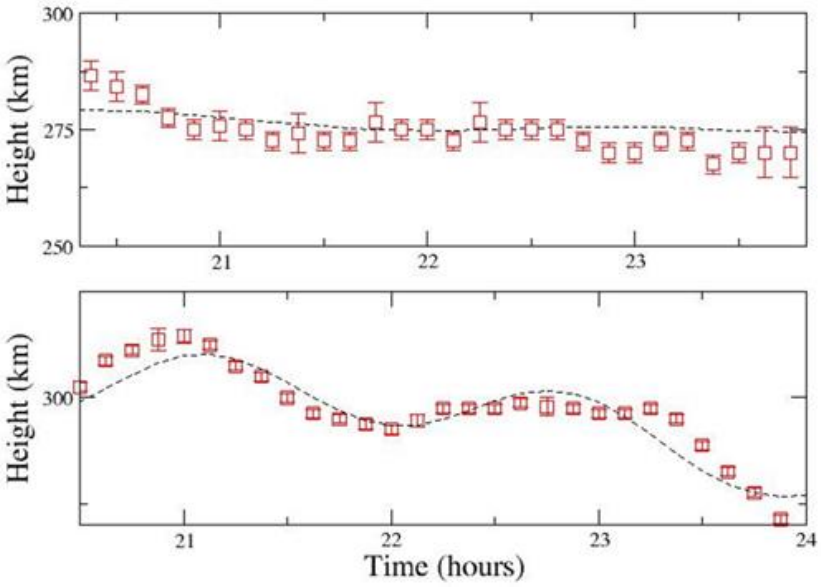

Figure 64. The model function (broken line) resulting from AMIAS analysis. The points of maximum intensity with their statistical error are also shown.

The HTI method has been implemented and is currently operated in an off-line mode under specific time intervals of interest over Europe and South Africa.it is expected to transition into a near real-time mode soon. The geographical scope for the European region is limited to the Digisonde stations in the region (37 - 55 N, −2 - 25 E); the geographical scope for the South Africa region is for ionospheric stations in the region (−22 - −35 N, 19 - 31 E). All products may be issued not later than 5 minutes after transfer of the latest ionogram observation.

The validation of the HTI method has been implemented in case studies in which the algorithm was validated against LSTIDs detected by other methods implemented in the TechTIDE project.

We show here two examples of the detection of LSTIDs with the HTI method for 20 January 2016 and 21 - 22 April 2017. In Figure 65 we can see the dominant LSTID periods for the two cases and in Figures 66 and 67 the HTI plots and the extracted periods over each station. The dominant periods extracted by HTI are consistent with the results of HF-TID and HF interferometry techniques provided in sections 3.1.2.4 and 3.2.2.5 respectively.

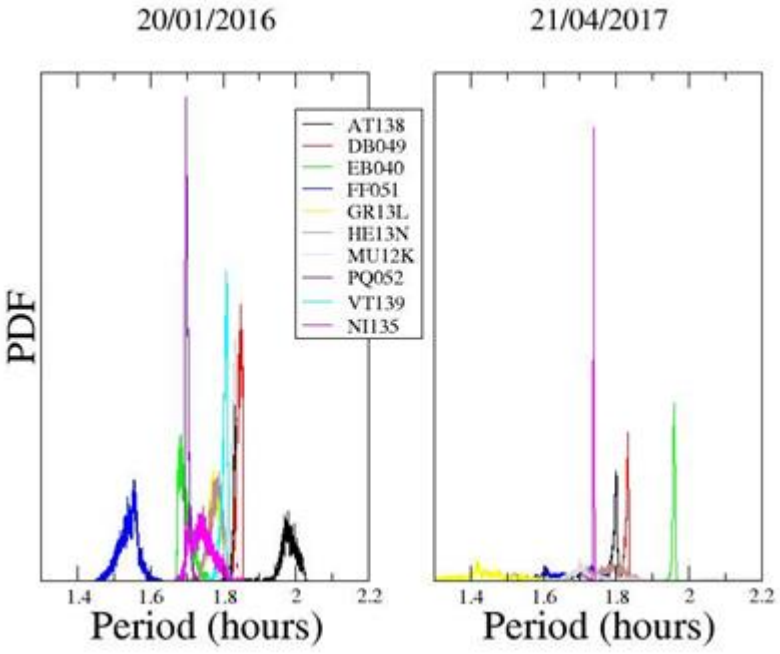

Figure 65. Dominant LSTID periods as extracted by HTI method and AMIAS over each station.

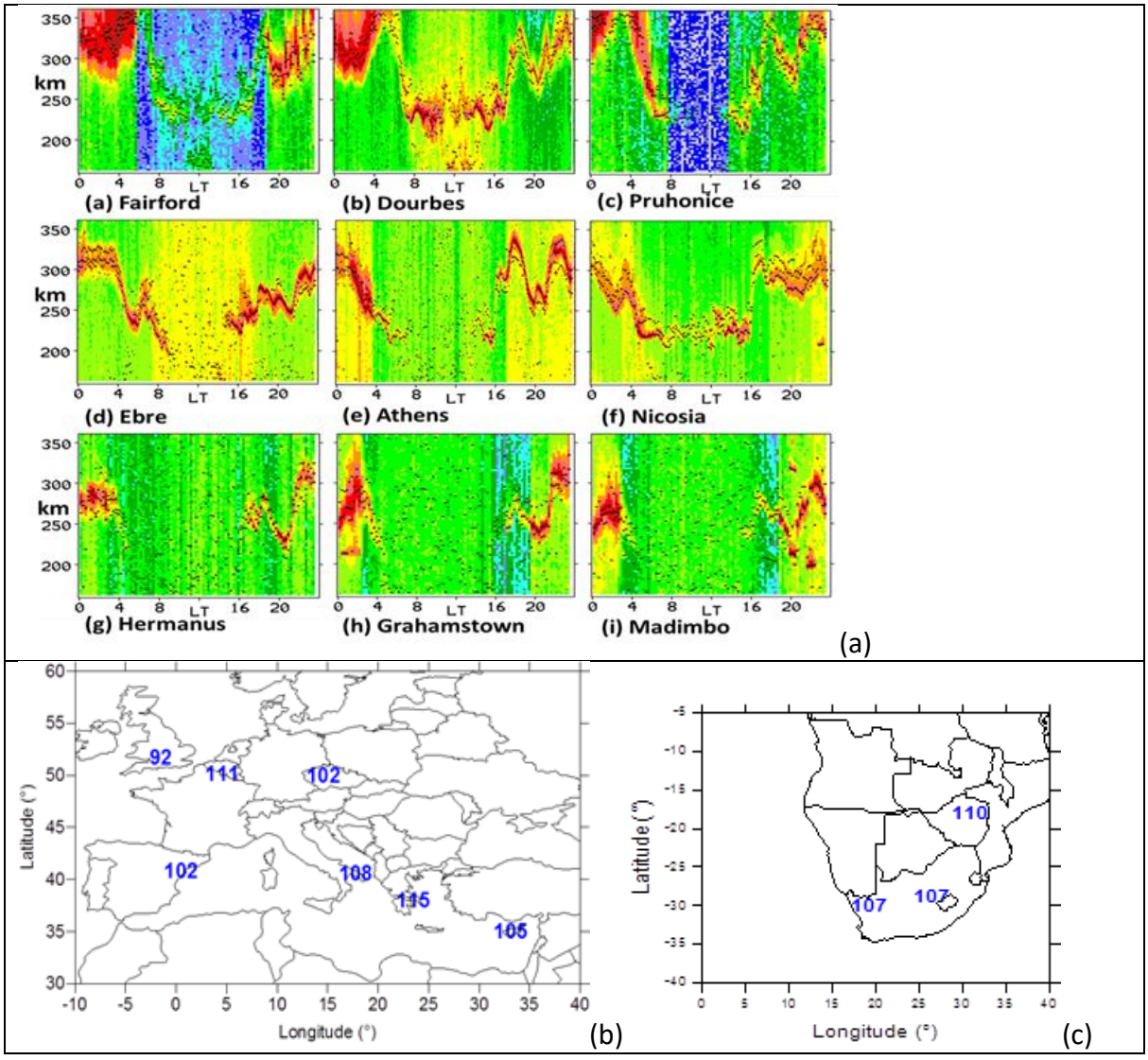

Figure 66. Detection of LSTID over Europe and South Africa for 20 January 2016 at 18:00 UT.

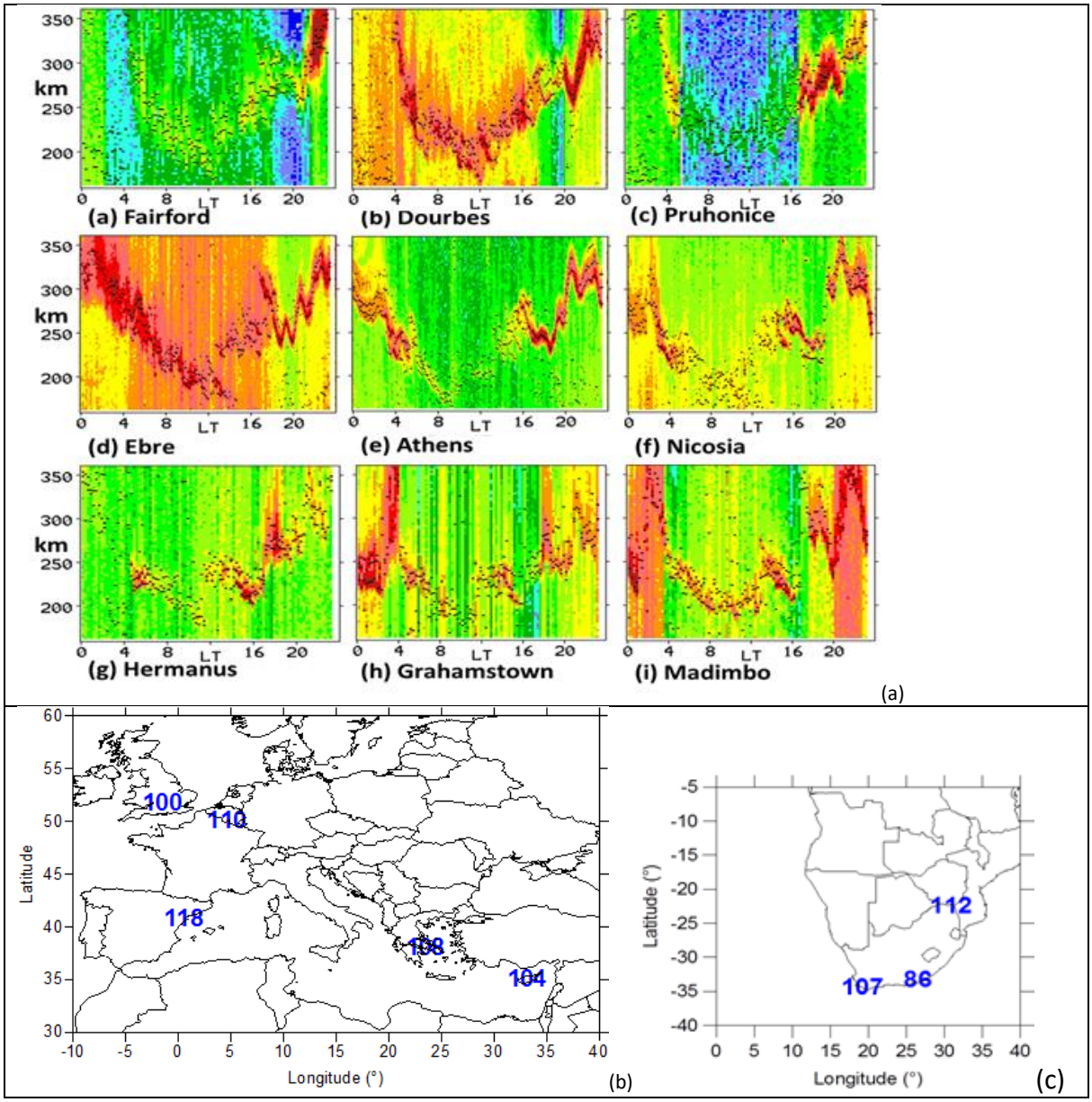

Figure 67. Detection of LSTID over Europe and South Africa for 21 April 2017 at 18:00 UT.

4.7 Verification of CDSS Method

There is possible to verify the CDSS method by comparing phase paths computed from digisonde-derived N(h) profiles and CDSS outputs during simultaneous common volume campaigns. In particular, ionospheric disturbances well appear on Doppler records. The uncertainty within the Doppler shift measurement is mainly determined by the instability of the frequency of reference generators and errors arising due to interference of radio waves. Both errors can be reduced with the help of CDSS design and corresponding computer programs. The Doppler shift of a radio wave can be calculated using the equation [RD-22]:

$$fd = \frac{f}{c_L}\frac{dP}{dt} \quad , \tag{4.7.1}$$

where *f* is the carrier frequency of the radio sounder, and c_L is the speed of light,

$$P = \int_s \quad n\,cos\alpha ds \tag{4.7.2}$$

is the phase path of a radio wave, α is the angle between trajectory of radio ray and z axis (z is vertical coordinate), *s* is the path of radio ray from transmitter to receiver and *n* is the refractive index : $n = \sqrt{1-A}$, where

$$A = \frac{2w(1-w)}{2(1-w) - u\,sin^2 \quad \lambda \pm\sqrt{u^2\,sin^4\,\lambda + 4u\,(1-w)^2\,cos^2\,\lambda}} \tag{4.7.3}$$

$w = N/Nm$, $Nm = 1.24f^2 10^{10} electron/m^3$ is the electron density at the height of radio wave reflection, *N* is the electron density at a given height $u = f_H^2/f^2$, λ is the angle between direction of the geomagnetic field and radio wave trajectory, f_h is the gyro frequency for geomagnetic latitude of ionospheric sounding, the sign "+" is for ordinary waves and "-" is for extraordinary waves. The absorption of radio waves and the variation of geomagnetic field with time have been neglected.

Equation (4.7.2) takes into account the electron density profile (N(h) profile) from the initial height to the height of radio wave reflection. To compare the Digisonde and Doppler data we use N(h) profiles obtained from ionograms by the inversion algorithm NHPC (a program for inversion of scaled ionogram traces into electron density profiles) incorporated in the ARTIST scaling program (Automatic Real Time Ionogram Scaler with True height algorithm). The inversion technique is based on the least squares fitting of modified Chebyshev polynomials to the profiles of each of the ionospheric layers. Then we calculate the phase path P (Eq. (4.7.2)) of the sounding radio wave, P_i. To calculate the phase path Pd on the basis of Doppler record, we use an equation derived from equation (4.7.1):

$$P_d = -\frac{c}{f}\int_0^t \quad f_d\,(t)dt + h_0\,, \tag{4.7.4}$$

where h_0 is a constant.

The relative accuracy of P_d is determined only by the accuracy of measurement of the Doppler shift fd, while the absolute accuracy is influenced also by the accuracy of h_0 determination. Parameter h_0 in eq. (4.7.4) cannot be directly calculated from Doppler records. However, we can calculate the entire phase path using N(h) profiles inverted from the recorded ionograms and eq. (4.7.2) – the inversion method considers the ordinary trace (O-trace). For the given day there is possible select the intervals, when there is only an O-trace on the ionograms in the surrounding of the working frequency of the Doppler measurements. Then it is assumed for these intervals that the phase paths obtained from the ionogram (P_i) and from the Doppler measurement (P_d) are equal. For the given day there are several data points, which can provide slightly different h_0 . Then we fit the set of individual P_i and P_d, using the least squares method to obtain the value of. We assume that the phase path from the ground surface to the radio wave reflection point equals to the backward phase path from the radio wave reflection point to the ground surface. Therefore, for comparison of the phase paths we use P_c(t)=P_i(t)/2 and P_e(t) = P_d(t)/2; time variations of P_c and P_e are similar to time variations of the reflection height.

4.7.1. Optimization of CDSS Method

The proper values of thresholds Th1, Th2, Th3 were found experimentally by visual checking of spectrograms. Their optimum values might change if the background noise changes or if the character of signal changes, e.g., frequent splitting to ordinary and extraordinary mode or a partial spread F conditions might cause problems. Current values of Th1, Th2, Th3 are based on initial testing on limited number of examples, and may be changed in future after getting larger experience with automatic detection.

Also, current software package uses an external value of ground wave from transmitter Tx2 that has to be removed to reliably find spectral maximum of the Tx2-Rx sky wave. This external value has to be updated if necessary (e.g. owing to long-term drift).

The information is updated each 15 minutes. So, there is an overlap as the analyzed intervals are longer.

Testing site is at http://datacenter.ufa.cas.cz/TID/

4.7.2. *Verification against known events*

The CDSS method is mostly effective for detection of acoustic gravity waves and MSTIDs with periods up to 45-50 minutes.

Below we analyse the May 27-28 event:

Beginning at 27/14:47 UTC, a small shock was observed indicating the arrival of the 23rd May CME. Total field increased from 3 nT to 10 nT while the solar wind increased from 303 km/s to 353 km/s. Although solar wind speed remained fairly steady between 350 km/s and 380 km/s, another increase in total field was observed with the transition into the magnetic cloud at 27/20:00 UTC. Total field reached a maximum of 23 nT at 27/22:30 UTC before it slowly declined to near 13 nT by the end of the period. The Bz component deflected southward to -20 nT beginning at 27/20:36 UTC and remained negative until 28/14:42 UTC. Geomagnetic field activity was at quiet to active levels on 29 May due to waning CME effects. (Event from the HELCATS catalogue).

We analysed activity of atmospheric waves of different periods during the May 2017 event using CDSS, GNSS and DPS-4D drift measurements. Observations for day or two before and after the event are also included in the figures below.

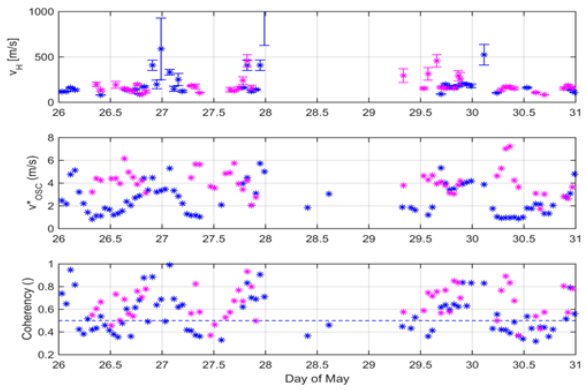

Figure 68a. Analysis of the horizontal plasma drift velocity v_H ,oscillation velocity v^*_{OSC} and coherency based on the Czech CDSS network measurements. All the results are for the period range of 5-45 min. Color coding: blue for 3.59 MHz, magenta for 4.65 MHz

Here v_H is the observed horizontal velocity of a GW (TID) propagation and v^*_{OSC} is the oscillation velocity of plasma induced by a GW (TID) estimated from the observed Doppler shift by equation

$$v^*_{OSC} = -f_{DRMS} \cdot \frac{c}{2f_0},$$

where f DRMS is the square root of the average Doppler shift power in the interval of analysis (90 min), c is the speed of light and f_0 is the sounding frequency. Coherency is a

pseudocoherence of three Doppler shift sounding paths estimated as maximum in the normalized slowness map [RD-23].

The CDSS data indicate increased atmospheric wave activity and significant enhancement in the horizontal plasma drift velocity around the midnight of 27th and 28th of May in consequence of the 23rd May CME forcing.

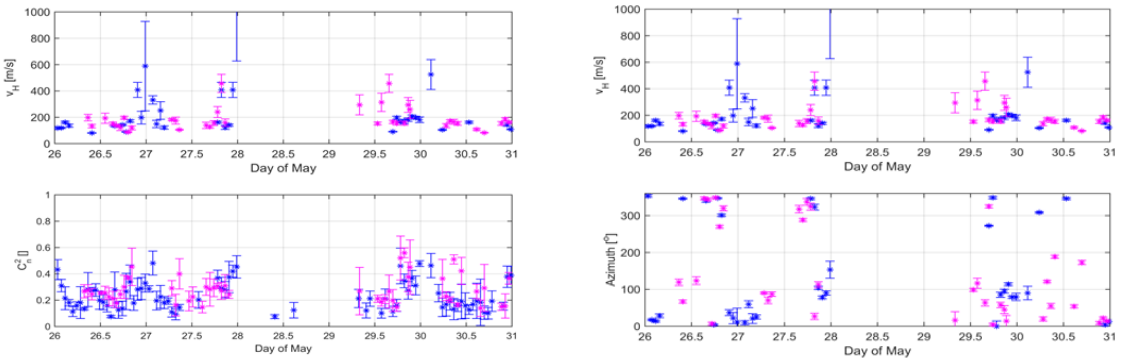

Figure 68b. Comparison of the horizontal plasma drift velocity v_H calculated from the Czech CDSS network measurements and the square of cross-correlation coefficient C^2 between North-South component of geomagnetic field measured at the Budkov geomagnetic observatory, Czech Republic, and Doppler shift (average for all 3 sounding paths). Values of vH and azimuth for Coherency >=0.5 are only presented. All the results are for the period range of 5-45 min. Color coding: blue for 3.59 MHz, magenta for 4.65 MHz.

From the DPS-4D drift measurements there is very well seen significant oscillation of the vertical component at the beginning of the storm main phase during the night of 27th May and the following night of 28th May (± 50 m/s), and regular drift course recorded day before the event (e.g. a presence of the typical morning and evening peaks, gradual velocity increase from small negative values through zero around noon to small positive values in the late afternoon). Similar storm-time course was observed also for both horizontal components.

Wave activity with periods ~2-3 h and ~4 h are seen at 27th May. Enhanced TEC oscillation was observed also during whole day of 28th May with periods of ~4 hours.

LSTIDs and MSTIDs on 27th-28th May were confirmed also by the HF-TID method (e.g. LSTID with WAm 21.6%, WP 110 min, WAz 271 deg from 23:30 of 27th May till 02:00 of 28th May on Ebro-Dourbes path of 4725 kHZ; LSTID with WAm 27.9%; WP 120 min; WAz 66 deg from 18:30 till 21:00 on Juliusruth-Pruhonice path of 5760 kHZ; MSTID with WAm 37.4%; WP 45 min; WAz 204 deg from 00:30 till 02:00 on Juliusruth-Pruhonice path of 2450 kHZ on 28th May).

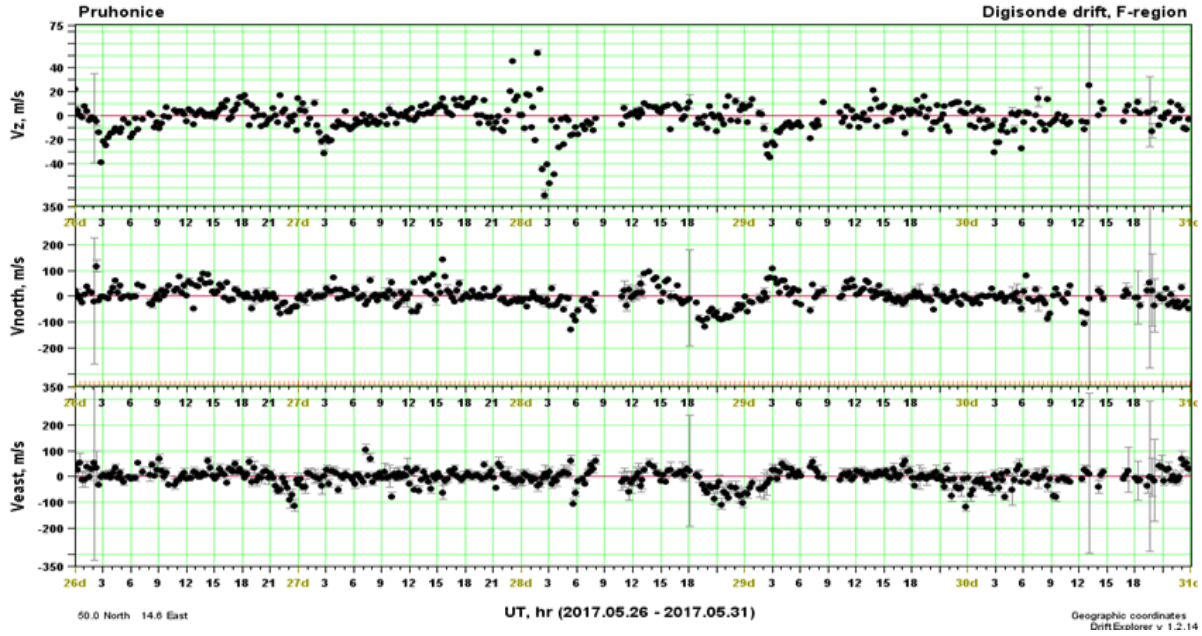

Figure 69. Course of the vertical and horizontal components of the drift velocity, as it was observed at Pruhonice ionospheric station.

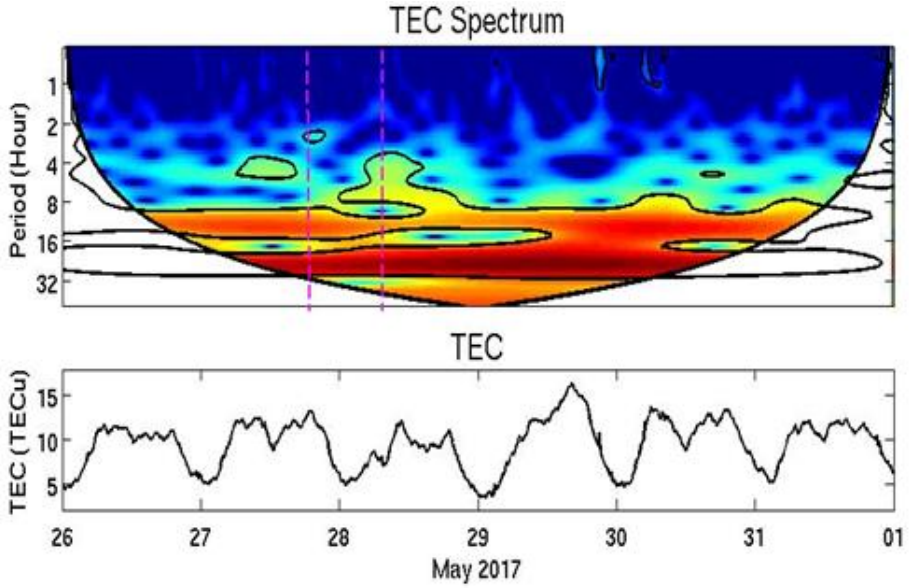

Figure 70. Wavelet spectrum analysis of the Pruhonice GPS TEC for 26-30 of May 2017. The black lines denote statistically significant areas of increased activity. The vertical dashed purple lines denote maximum *Dst* at the beginning of the main phase, and minimum *Dst* – the end of the main phase of the storm.

4.8 Verification of AATR

AATR has been used for detecting ionospheric activity for hundreds of receivers during more than a Solar Cycle. As can be seen in the next example, AATR is sensitive to most of the effects that disturb the ionosphere (geomagnetic activity, Solar flares, scintillation, ...).

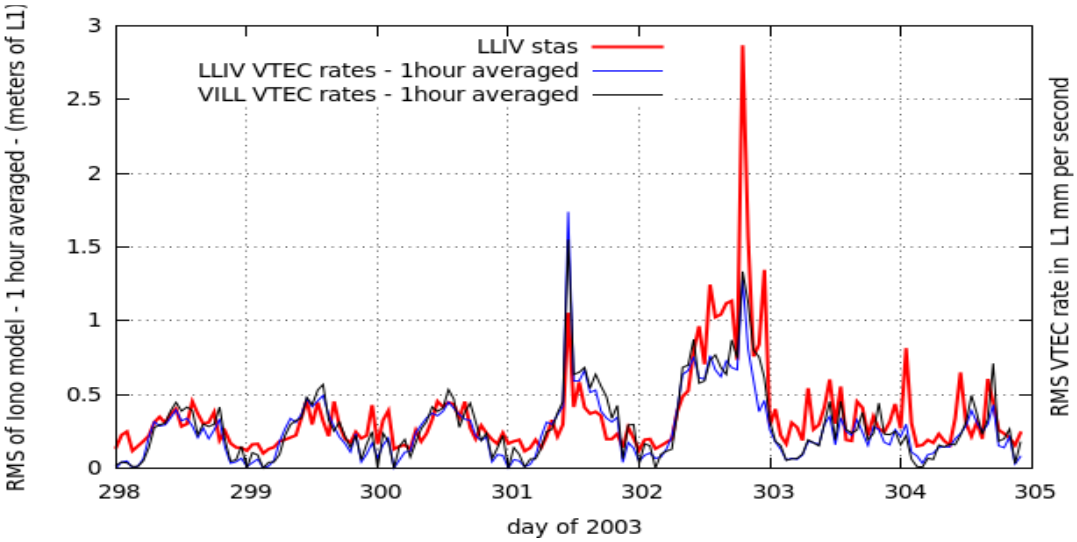

Figure 71. Example showing the AATR values during the Halloween storm in 2003 for 2 receiver in the Iberian peninsula. The AATR reflects the Solar Flare occurred during day 301 and the consequent ionospheric storm during days 302 and 303

It has been shown that, for receivers placed in the auroral region, AATR is quite correlated with the DST (Figure 72):

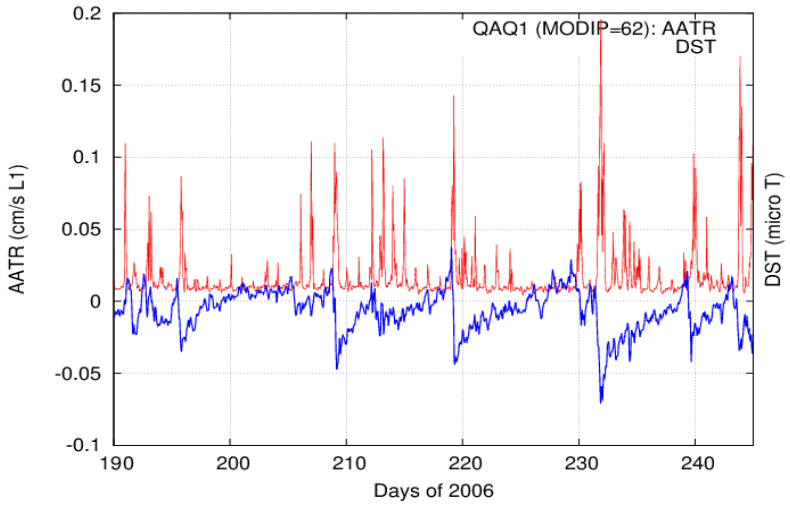

Figure 72. Example showing the correlation between the DST and the AATR values for a receiver (QAQ1) in Greenland

In this sense, unlike a planetary index, AATR can reflect the different impact that a specific space weather event can have in different regions. For instance, Figure 73 depicts the AATR values for 4 receivers during the event on April 21-22 2017 reported in WP3.

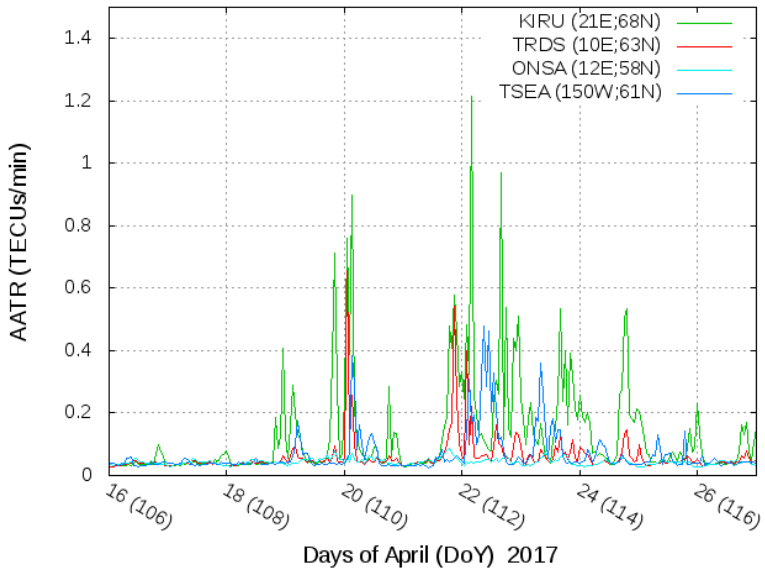

Figure 73. AATR values for 4 different European receivers at different latitudes during the event starting in April 21th 2017 which is reported in WP3

Therefore, AATR can reflect ionospheric activity in a regional context. This is shown in the next figure, where large AATR values for a receiver in the Canary Islands are related with degradation in the EGNOS availability in this region.

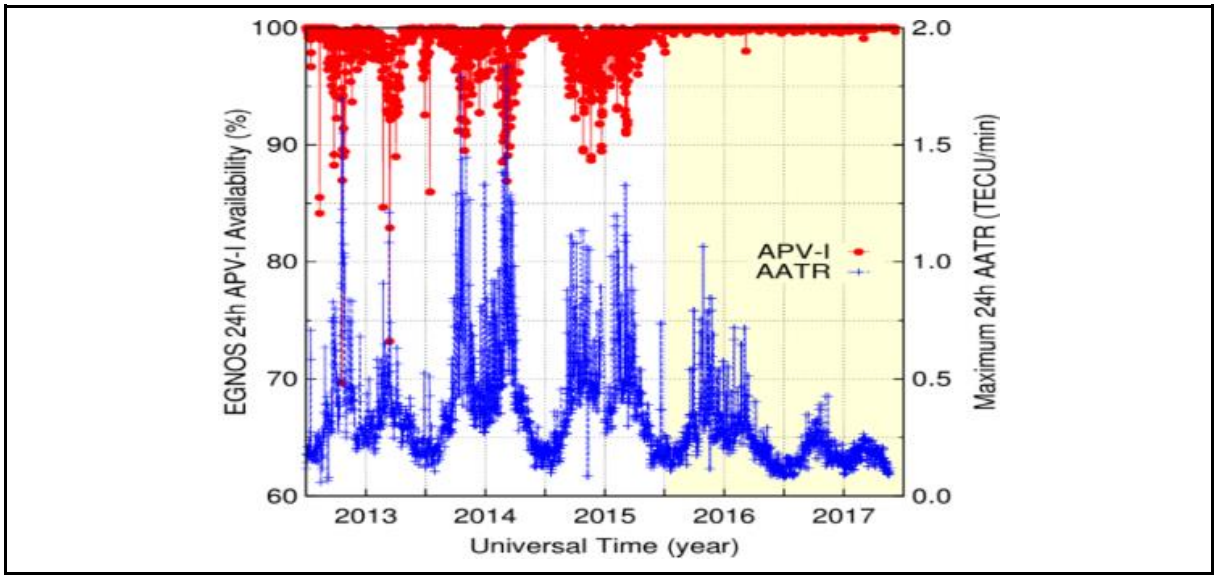

Figure 74. Relationship between the AATR values for a receiver in the Canary islands and the EGNOS availability

Thanks to this relationship, AATR index has been adopted as a standard tool by the International Civil Aviation Organization (ICAO) for joint ionospheric studies in SBAS.

5. Benchmark metrics of TechTIDE algorithms

Primary purpose of this benchmarking study is to evaluate capabilities and requirements for transitioning TechTIDE algorithms to the real-time operations. All TechTIDE partners have access to low-latency data feeds from the member observatories, with the typical latency of data arrival to analysis centers well below 10 minutes since the measurement start time. It is important to stress that, however, the oscillating nature of the TID phenomenon requires algorithms to reliably identify presence of the quasi-periodic variations in the input data (whether in space or in time). In turn, this requires a good portion of one wave period to be acquired and available for such detection. In other words, in order to sense a 30-minute period TID in progress at particular observatory location, a "real-time" processor has to accumulate 30 minutes data since the event start.

This does not mean that one-period latency is always system-inherent for any TID wave event in progress at an observatory site. Observations *up-stream* in the direction of TID arrival are instrumental in prompt local detection of ongoing events by means of the spatial gradient analysis. Feasibility of the TID warning systems is further strengthened by the capability of TID detectors to sense direction and velocity of the wave propagation. Correspondingly, *probability* of the detected TID event to affect users in the upcoming areas of TID propagation can be evaluated and reported to the users.

In the following sections, the benchmark metrics of TechTIDE algorithms do not address the question of data accumulation prior to detection. The following aspects of algorithm performance are considered:

- Measurement data latency that delays start of processing until all needed data are acquired, including
  - Measurement duration
  - Data delivery time
  - Measurement processing prior to evaluation for TID signatures
- TID computation time
- Selection of computing hardware for the task
- Cadence of measurements and TID computations

5.1 HF-TID benchmarking

The HF-TID real-time processor is a continuously running application that triggers it processing sequence every minute of the hour. It takes a few seconds to review availability of the newly arrived D2D measurements in Lowell GIRO Data Center. Should such new records exist, the

processor runs its complete analysis suite against new data, including computation of the arrival angles, clustering of sources into signals, signal tracking within analysis time window, and TID detection and evaluation using the multi-window iterative algorithm. Detected TID events are stored in TIDBase of LGDC. Overall, the computing time does not normally exceed 15 seconds.

HF TID Benchmark	Value
D2D measurement duration	20 sec (long pulse) or 40 sec (short pulse)
D2D measurement cadence	2.5 min (long pulse) or 5 min (short pulse)
Data delivery latency to processing center	< 3 minutes
Central processing of measurements	< 20 sec of data dispatch and databasing
TID detection update rate	Every minute
CPU time	minor (<15 seconds)
CPU type	Xeon E5-2620 2.1 GHz

5.2 HF interferometry products

The method takes less than 30 seconds to get the result and starts at minute 5. However, we have to wait for 4.5 minutes to download the data to be sure that all stations provided data to the data server at http://giro.uml.edu/didbase/scaled.php. In addition, as we work with Fourier analysis, to efficiently detect a TID we need that at least three stations observe one complete cycle of the wave (see figs. 40, 42), which is typically 80-120 minutes. In addition, it is needed the propagation time of the wave between 3 stations, which for typical velocities of LSTIDs of 500 m/s use to be at around 20-25 minutes. Although the physical characteristics of the CPU are indicated in the next table, all programs are running in a Virtual Machine into a server which shares other tasks of the institute. The VM has 8 vCPUs.

HF Interferometry Benchmark	Value
Ionogram duration	~1 min
Ionogram cadence	5 min (optimal), 15 min (nominal)

Ionogram analysis (autoscaling)	< 10 sec
Data delivery to center	< 3 min
TID detection update rate	5 minutes
Total TID processing Latency	4.5 minutes (since the ionogram start)
CPU time	minor (< 30 seconds)
CPU type	8 CPUs x Intel(R) Xeon(R) CPU E5-2620 v4 @ 2.10GHz

5.3 Spatial and temporal GNSS analysis

5.3.1 MSTID detection

Benchmark	Value
update rate	5 minutes
latency	Almost real time if data are available
CPU time	minor

5.3.2 Propagation parameters.

Benchmark	Value
update rate	5 minutes
latency	A time comparable to the MSTID period
CPU time	minor

5.4 TEC Gradient products

Benchmark	Value
update rate	15 minutes

latency	5 minutes (1 minute after provision of TEC maps)
CPU time	minor

5.5 Electron Density Distribution products

In the off-line mode, the method takes 1.5 sec to calculate the ED in 1D version.

The on-line implementation is based on the real-time analysis of Digisonde data from the contributing ionospheric stations in Europe and in South Africa and on the acquisition of TEC parameters from the European and global TEC maps released by DLR. Therefore, a latency of 15-20 min should be considered.

5.6 HTI method products

The method takes less than 10 seconds to generate the HTI plot and less than a minute to estimate the TID period following spectral analysis for each station. It will start operating every five minutes and generate the HTI plot and estimate the TID period for any station that provided a new ionogram within that interval. To allow for ionograms from all stations to be received it will probably take some considerable time within this 5 minute interval. Therefore for every new ionogram that arrives the process for that station will start immediately provided that the autoscaled data (http://giro.uml.edu/didbase/scaled.php) that that are also needed to determine the optimum frequency bin for that station have also arrived. In addition, as we utilize spectral techniques, to efficiently estimate the TID period we need that at least that each station observes one complete cycle of the wave, which is typically 80-120 minutes.

HF Interferometry Benchmark	Value
Ionogram duration	~1 min
Ionogram cadence	5 min (optimal), 15 min (nominal)
Ionogram analysis (autoscaling)	< 10 sec
Data delivery to center	< 4.5 min
TID detection update rate	5 minutes
Total TID processing Latency	4.5 minutes (since ionogram reception)

CPU time	minor (< 1 minute for each station but will execute in parallel)
CPU type	Unspecified yet. Presently offline procedure runs on a PC.

5.7 CDSS product

Benchmark	Value
update rate	15 minutes
latency	15 minutes after all data are processed
CPU time	minor

5.8 AATR product

Benchmark	Value
update rate	5 minutes or 1 hour
latency	Almost real time if data are available
CPU time	minor

6. Validation of TechTIDE Algorithms

Validation is a process of evaluating how developed TechTIDE algorithmic solutions match users' expectation. Such evaluation is done by reviewing algorithm capabilities against the user requirements.

in the following analysis, three degrees of compliance to the requirements are used:

- **Complete**: subsystem as implemented fully satisfies the requirement
- **Partial**: subsystem satisfies the requirement, but not on all occasions or in all regions
- **In progress**: subsystem R&D team works to satisfy the requirement

When evaluating the subsystem compliance, the nominal operation of the data providers is assumed; potential data gaps and latencies due to the sensor or communications outages are not considered degrading.

The TID methods in the validation review are identified by the following ID number:

1. HF-TID method
2. HF Interferometry
3. Spatial and temporal GNSS analysis
4. GNSS TEC gradient
5. 3D-EDD maps
6. HTI
7. CDSS
8. AATR indicator

6.1. Service Requirements

SERVICE REQUIREMENTS		
ID	**Name**	**Compliant Subsystems**
TeT-SRV-0020.1	Scope: TID detection (**Mandatory**) Users shall be informed in near real-time on TIDs occurrence: both LSTIDs and MSTIDs	**LSTID**: 1, 2, 3, 4, 5, 6, 8 **MSTID**: 1, 3, 4, 7, 8

TeT-SRV-0060.1	Ionospheric conditions: background (**Mandatory**) The system shall assess the ionospheric background conditions	**Complete**: 1, 2, 3, 4, 5, 7, 8
TeT-SRV-0070.1	Ionospheric conditions: forecast (**Mandatory**) The system shall forecast ionospheric conditions for the next 24h	[no forecast capability]
TeT-SRV-0080.1	Interhemispheric circulation (**Mandatory**) The system shall identify TIDs travelling equatorward and being observed in the other hemisphere	**Complete:** 3, 4 **In Progress**: 1, 2, 5, 6
TeT-SRV-0090.1	Geographical scope: Europe (**Mandatory**) Users shall be informed on TIDs in the area: 20 to 72 deg lat and -40 to 40 deg lon	**Complete**: 3, 4, 8 **Partial**: 1, 2, 5, 6, 7
TeT-SRV-0100.1	Geographical scope: extended Europe (**Desirable**) Users shall be informed on TIDs in the area: 0 to 72 deg lat and -40 to 80 deg lon.	**Complete**: 3, 4, 8
TeT-SRV-0110.1	Geographical scope: South Africa (**Mandatory**) Users shall be informed on TIDs in the area: -20 to -35 deg lat and 15 to 35 deg lon	**Complete**: 3, 4, 8 **Partial**: 1, 2, 5, 7 **In Progress**: 6
TeT-SRV-0120.1	Geographical scope: global real time (**Desirable**) The spatial coverage of near real-time data shall be: -90 to 90 deg lat and 0 to 360 deg long	**Complete**: 3, 4, 8

TeT-SRV-0130.1	Geographical scope: global archive (**Desirable**) The spatial coverage of near real-time data shall be: -90 to 90 deg lat and 0 to 360 deg long	**Complete**: 3, 4, 8 **Partial**: 1, 2, 5, 6, 7
TeT-SRV-0140.1	Geographical scope: global forecast (**Desirable**) The spatial coverage of forecast data shall be long: -90 to 90 deg lat and 0 to 360 deg long.	[no forecast capability]

6.2. Overall Performance Requirements

OVERALL PERFORMANCE REQUIREMENTS			
ID	**Name**	**Users**	**Compliant Subsystems**
TeT-PRF-2100.1	Timeliness: MSTID Warnings (**Mandatory**) Warnings on the localized occurrence of MSTIDs shall be issued not later than 5 minutes after observation (completion of measurements)	NRTK	**Complete**: 1, 3, 4 **In Progress**: 6, 7
Various per sub-system	Timeliness: Data product release (**Mandatory**) Subsystems shall release intermediate and final data products not more than 5 minutes after observation (completion of measurements)	EGNOS, HF, NRTK	**Complete**: 1, 2, 3, 4, 6,8 **In Progress**: 7

TeT-PRF-2090.1	Timeliness: forecast (**Desirable**) Time between forecast and product provision shall be at least 15 minutes up to 3 days ahead	ESA	[no forecast capability]
TeT-PRF-2220.1	Spatial resolution: near real-time data (**Desirable**) The spatial resolution of near real-time data shall be 100 km	ESA	**Partial**: 3, 4
TeT-PRF-2230.1	Spatial resolution: archive data (**Desirable**) The spatial resolution of archive data shall be 100 km	ESA	**Partial**: 3, 4
TeT-PRF-2240.1	Spatial resolution: forecasts (**Desirable**) The spatial resolution of forecast data shall be 100 km	ESA	[no forecast capability]
TeT-PRF-2310.1	Temporal resolution: near real-time data (**Desirable**) The time interval between two near real-time product/data points shall be less than 5 minutes	ESA	**Complete**: 1, 3, 4, 7, 8 **Partial**: 2, 5,6

TeT-PRF-2320.1	Temporal resolution: archived data (**Desirable**) The time interval between two near real-time product/data points shall be less than 5 minutes	ESA	**Complete**: 1, 3, 4, 7, 8 **Partial**: 5,6
TeT-PRF-2330.1	Temporal resolution: forecasts (**Desirable**) The time interval between two near real-time product/data points shall be less than 15 minutes	ESA	[no forecast capability]

6.1.3. Per-system Product Requirements

1. HF-TID Product requirements		
ID	**Name**	**Fulfilment**
TeT-PRD-1010.1	HF-TID final (**Mandatory**) The system shall estimate for LSTIDs and MSTIDs the values of: TID period, phase velocity, direction of propagation, wavelength and amplitude.	Y
TeT-PRD-1020.1	HF-TID intermediate (**Desirable**) The system shall estimate for HF communication: the Doppler frequency, angle of arrival, and time-of-flight from transmitter to receiver, both OI and VI sounding	Y

TeT-PRD-1220.1	Signal-to-Noise ratio on links (**Mandatory**) The system shall calculate the signal-to-noise ratio on link sections between the DPS4D sounders	Y
TeT-PRD-1230.1	Path probability ratio on links (**Mandatory**) The system shall calculate path probability ratio on link sections between the DPS4D sounders	N (uses frequency-agile algorithms based on real-time data to ensure uninterrupted operations)

2. HF Interferometry Product requirements		
ID	**Name**	**Fulfilment**
TeT-PRD-1030.1	HF interferometry final (**Mandatory**) The system shall estimate for LSTID: dominant period, amplitude and 2D vector velocity	Y
TeT-PRD-1040.1	HF interferometry intermediate (**Desirable**) The system shall estimate: de-trended ionospheric characteristics and spectral energy contribution for specific measuring stations.	Y

3. Spatial and temporal GNSS Product requirements		
ID	**Name**	**Fulfilment**

TeT-PRD-1050.1	Spatial and temporal GNSS analysis final (**Mandatory**) The system shall estimate TID velocity, direction of propagation and amplitude	N (This can be done in regions where baselines of some tens of km can be found.)
TeT-PRD-1060.1	Spatial and temporal GNSS analysis intermediate (**Desirable**) The system shall estimate de-trended GNSS products that remove the nominal ionospheric variations	Y

4. GNSS TEC Gradients Product requirements		
ID	**Name**	**Fulfilment**
TeT-PRD-1070.1	GNSS TEC gradients final (**Mandatory**) The system shall deliver TEC gradients	Y
TeT-PRD-1080.1	GNSS TEC gradients intermediate (**Desirable**) The system shall deliver maps of TEC and TEC rate	N (The system will deliver TEC gradients, but no TEC maps and TEC-rate)

5. 3D-EDD Maps Product requirements		
ID	**Name**	**Fulfilment**

TeT-PRD-1090.1	3D-EDD maps final (**Mandatory**) The system shall deliver TEC gradients	Y (the system will deliver gradient maps of the integral of the electron content over specific ionospheric layers, to give a better specification of the altitude of maximum disturbance)
TeT-PRD-1100.1	3D-EDD maps intermediate (**Desirable**) The system shall estimate 3D electron density distribution (EDD) for the bottomside ionosphere	Y
TeT-PRD-1110.1	3D-EDD maps topside intermediate **(Desirable)** The system shall estimate 3D electron density distribution (EDD) for the topside ionosphere	Y

6. HTI Product requirements		
ID	**Name**	**Fulfilment**
TeT-PRD-1120.1	HTI intermediate (**Desirable**) The system shall estimate the dominant period of wave activity	Y

TeT-PRD-1130.1	HTI final (**Mandatory**) The system shall estimate the signal-to-noise ratio variation of vertically reflected radio signals above a given measuring station	N (The system shall estimate F region virtual height variation not signal to noise variation)

7. CDSS Product requirements		
ID	**Name**	**Fulfilment**
TeT-PRD-1140.1	CDSS intermediate (**Mandatory**) The system shall estimate the period, amplitude and phase of Doppler shift measurements	Y
TeT-PRD-1150.1	CDSS final (**Mandatory**) The system shall estimate continuous Doppler shifts of fixed sounding radio frequencies	Y

8. AATR Product requirements		
ID	**Name**	**Fulfilment**
TeT-PRD-1160.1	AATR intermediate (**Mandatory**) The system shall estimate TEC rate	Y
TeT-PRD-1170.1	AATR final (**Mandatory**)	Y

	The system shall use AATR and TEC rate to identify regions where the ionosphere is disturbed with respect to nominal conditions	

6.1.3. System-wide Product Requirements

SYSTEM-WIDE PRODUCT REQUIREMENTS		
ID	**Name**	**Compliance**
TeT-PRD-1180.1	foF2 maps (**Desirable**) The system shall deliver a real-time foF2 map showing the effects of the TID incorporated	Y
TeT-PRD-1190.1	Maximum Usable Frequency (**Desirable**) The system shall deliver MUF	Y
TeT-PRD-1200.1	Sunspot Number (**Desirable**) The system shall deliver sunspot number	Y
TeT-PRD-1240.1	Ionosphere perturbation index (**Mandatory**) The system shall calculate an ionosphere perturbation index indicating any current ionosphere small scale perturbations (scale below 80 km) in Europe	Y

7. Summary and conclusions

The current status and capabilities of the TID detection methodologies have been presented jointly with the design of adjustments and upgrades. Different methods tried to adopt the initial requirements gathered among users affected by TIDs according to the current monitoring capabilities. A degradation with what one actually plans to achieve in TechTIDE is provided by given methodologies for those requirements that cannot be fully achieved. Such a “no fulfillment” is mainly due to the limitation of available network sensors for probing the ionosphere and due to the limitation of available measurements and data of the existing sensors for probing the ionosphere. A major constraint, especially for the methods that are based on HF measurements, is the time resolution; The operational soundings are currently obtained with a cadence of five minutes. Tests have been done demonstrating the feasibility of decreasing the sounding interval to 2.5 minutes, depending on the future roll-out of both hardware and software upgrades. This will allow for the detection of smaller scale TIDs (related user-requirement TeT-SRV-0020.1). This is still under experimentation.

Another major “non-fulfillment” results from the requirement for early forecast of TID activity. This requires the development of models whose drivers, in the solar radiation environment and in the solar wind, can be forecasted few days in advance. This to be done requires the combined exploitation of measurements from L1 and L5 vantage points as well as from Earth orbiting satellites and from ground-based solar radio monitoring systems. This is far beyond the objectives of the current project, but we consider carefully these requirements to design a follow up research programme.

In the frame of the TechTIDE effort, a set of value-added products are presented targeted to nowcasting methodologies providing also the probability for TID detection over certain areas for the next hours. These products are planned to be released in order to satisfy the majority of requirements of the user. The WP2 activities will be planned in relation to the WP3 work plan where the results of all TID detection methodologies will be cross-validated and evaluated based on the assessment of current geospatial and lower atmosphere conditions. The algorithms for the intermediate products will be released in January 2019 and their capabilities will be demonstrated in the first release of the TechTIDE warning system. The final and value-added products will be released towards the end of 2019 and will be implemented in the final version of the TechTIDE warning system.